Università degli Studi di Padova

Department of Information Engineering

Ph.D. Course: Information Engineering
Curriculum: Information Science and Technology
Series: XXXI

Analysis and Design of Innovative Antenna Systems for Telecommunications and Health Applications

Ph.D. Student:
Giulia Mansutti

Supervisor:
Professor Antonio–Daniele Capobianco

Coordinator:
Professor Andrea Neviani

Academic Year: 2017–2018

The two important things that I did learn
were that you are as powerful and strong
as you allow yourself to be,
and that the most difficult part of any endeavor
is taking the first step, making the first decision.

– Robyn Davidson –

Acknowledgements

At the age of 22, Robyn Davidson crossed the Australian Desert, from Alice Spring to the Indian Ocean, completely alone. I've chosen to report a quote from her in the previous page, because I feel that these three years have been a journey also for me (even if a far less wild one): I have moved back and forth between Padova, Trento and Brisbane, ending up feeling at home in two countries that are more than 14000 kilometers apart. Unlike Robyn though, I was not alone: I have been constantly surrounded by wonderful people, and for this, I feel extremely lucky.

I would like to express my appreciation to all of them, and I will start from my two lifelong number-one supporters. Thank you mum and dad for your infinite love and patience, and for always being on my side all the way through the last three years (actually all the way through the last twenty-six years). Thank you for all the support and advice: from those related to important decisions, to those that involved getting rid of spiders and cockroaches.

I would like to express my gratitude also to Professor Antonio Capobianco, who has been an amazing supervisor during these three years, and to Professor Andrea Galtarossa, without whom this Australian adventure would not have been possible. For the same reason, I would like to thank Professor Andrea Massa, that made me feel part of the Eledia family and that connected me to Professor Amin Abbosh and his wonderful research group in Australia. To Professor Amin and all the Microwave Team goes my gratitude for all the guidance they gave me, and for making me feel at home on the other side of the world.

Then I would like to thank my fellow Ph.D. Francesco for all the breakfasts at Soranzo's, and for the conference-adventures we've had together. Thanks also to Chiara, Maria, Marco and Mattia for all the Italy-USA-Australia Skype calls. Thank you Ziwei, Mohammed, Akbar and Effa, for our coffee times at Merlo's and for all the delicious food we had together down under (that made me really happy but also 5 kg heavier). Thanks to the 'Amici' group for an amazing Eastern weekend in the Gold Coast, and in particular a big hug to Veerle and Lydia for all our girls trips, lunches and brunches, and to Guen, for being such a patient surf instructor. Thanks also to my amazing flatmate Atena, with whom I've had a wonderful time and that I miss very much. Finally, I would like to thank my life-long friends, and in particular Giulia, Paola and Martina, for all the laughs, fights, trips, dinners, calls and voice messages.

To conclude, thanks to everyone I came across during this Ph.D.: you contributed to make these three years the most exciting chapter of my life so far.

Abstract

In this thesis the study of different innovative antenna systems is presented. The antenna designs that have been analyzed and that are described in this thesis can be divided in three main groups based on their application: phased-array antennas working on surfaces that change shape in time, millimeter-wave antennas for skin cancer diagnosis, and gaseous plasma antennas for satellite communications.

As far as the first topic is concerned, the research activity presented in this thesis focuses on the study of the strengths and limitations of a specific pattern recovery technique: the projection method. This technique has been adopted to retrieve the radiation properties of linear and planar arrays placed on surfaces whose shape changes in time according to different geometrical deformation; moreover its effectiveness was assessed for both broadside and beam steering arrays, leading to a novel and simpler formulation of this pattern recovery technique for arrays whose beam is tilted towards different directions. The results have been obtained both through full-wave numerical simulations in CST Microwave Studio and through measurements performed in collaboration with the North Dakota State University (NDSU), Fargo, North Dakota, USA.

Regarding skin cancer diagnosis, a novel substrate integrated waveguide probe for early-stage skin cancer detection has been designed as well: this probe is cheap and easy to fabricate and can achieve high accuracy in detecting small early-stage skin cancer, thus providing a tool with the potential of being adopted as a real aid for skin cancer diagnosis. The probe has been tested both through full-wave numerical simulations and through measurements on a skin phantom realized at The University of Queensland with the support of the Microwave Team.

The study about gaseous plasma antennas for satellite communications has been mainly numerical. Different designs have been conceived with the aim of exploiting the advantages of using plasma elements while at the same time avoiding the limitations related to this novel technology. A practical implementation of these designs is now the subject of a collaboration with CISAS B. Colombo, an aerospace research center of the University of Padova.

Contents

List of Figures

Chapter 1

Introduction

This thesis comprises three main chapters, one for each topic studied during this Ph.D.: self-adapting phased array antennas, gaseous plasma antennas and antennas for skin cancer detection. The purpose of this introduction is to give a brief description of what has been studied and achieved in these three fields. Every topic will be then thoroughly addressed in a dedicated chapter with a specific introduction.

Self-adapting phased array antennas are antennas capable of adapting to surfaces that change shape in time. This feature makes them appealing for different applications in which the antennas are subject to deformations, shifts and vibrations (e.g., wearable devices, vehicle-to-vehicle communications), provided that they can maintain their radiation properties even when they are deformed. In order to fulfill this requirement, different pattern recovery techniques can be adopted: some of these are very accurate but also very expensive, while others are simpler, less expensive but also less accurate. During my Ph.D. I have focused on the second class of these pattern recovery techniques (particularly suitable for simple antenna systems like wearable devices) and in particular the projection method (PM), continuing the collaboration between our department and the Electrical Engineering Department of the North Dakota State University (NDSU), Fargo, ND, US. I have started by studying the effectiveness of the PM in retrieving the radiation properties of different broadside antenna arrays. I have begun by considering linear broadside patch arrays placed on different deformed surfaces: a 1x4 wedge-shaped array, a 1x4 arc-shaped array, a 1x4 S-shaped array a 1x6 Z-shaped array. In all these cases the PM proved to be a good tool to retrieve the main radiation properties of the array. However, the effectiveness of the PM is limited to a region centered on the direction of maximum: the correcting capabilities of this method reduce for angles that are far from the broadside direction. Moreover, the higher the entity of deformation of the surface, the least the correcting capabilities of the PM far from the broadside direction. Then I have analyzed the performance of the PM when applied to a 4x4 array placed on a strongly deformed surface: the PM is capable of retrieving also the radiation properties of a planar antenna, but again, its effectiveness substantially decreases further from the direction of maximum. As a final step the capabilities of the PM to correct the radiation properties of an antenna array that steers its beam towards different directions have been studied: a new simplified version of this pattern recovery technique for beam tilting arrays was introduced and it was proved how it is effective in retrieving the radiation properties of a

4x4 and an 8x8 doubly wedge-deformed arrays.

Gaseous plasma antennas (GPAs) are antennas that exploit partially or fully ionized gas to transmit and/or receive EM waves. They present some interesting advantages with respect to their metallic counterparts: they can be electrically (rather than mechanically) reconfigured with respect to some antenna parameters such as input impedance, bandwidth and gain. Moreover, GPAs are also transparent to EM waves in two cases: when the plasma is off (since it reverts to its neutral state), and when the frequency of the impinging EM signal is above the plasma frequency. However, this interesting technology presents some important limitations: for example, it is difficult to match plasma loads and to realize plasma antennas that operate in the GHz regime, because they require very thin glass vessels to confine the plasma, proper electrodes to generate it and tailor-made signal couplers that allows to obtain satisfactory radiation properties. During my Ph.D. I have worked on the design of two types of plasma antennas: an active plasma dipole working between 600 MHz and 1 GHz, and a reconfigurable metal-plasma Yagi-Uda antenna. Both works have been conducted in collaboration with CISAS B. Colombo, an aerospace engineering research center of the University of Padova. The active plasma dipole provided good results in CST simulations, but proved to be cumbersome to feed and realize in practice: in CST the dipole is simply fed through a discrete face port, while in practice the design of a proper signal coupler represents a challenge. Moreover, the electrodes and the other equipment used to generate the plasma have a non-negligible influence on the operation frequency of the dipole. As far as the hybrid Yagi-Uda antenna is concerned, this proved to be a good solution to exploit plasma reconfigurability features and at the same time to avoid some of the issues related to this technology: the use of a classic metal dipole as the active element of the antenna simplifies the feeding of the structure, and the use of plasma discharges as directors allows to realize an antenna that can be reconfigured with respect to its gain.

During the time I have spent as a visiting Ph.D. Student at The University of Queensland, Brisbane, AU I have focused on the design of novel microwave devices for skin cancer detection. In particular, I have worked on the design of two new millimeter-wave devices for skin cancer detection: a substrate integrated waveguide probe for early-stage skin cancer detection and a conformal array-based directional antenna system for microwave applications. The first device can efficiently detect early-stage melanomas and has the potential of being used in practice as a real aid for skin cancer diagnosis because it is cheap, simple, fast to use and easy to feed. Its effectiveness has been proved both through full-wave numerical simulations and measurements on a skin phantom. The second device that I have designed, i.e., the conformal array-based antenna system, has also the potential of being used as an aid for skin cancer detection and more in general, biomedical applications: in fact, it can achieve a uniform E-field over a wide angle, that is a desirable feature for many biomedical applications; moreover, it is based on four patch antennas and it is therefore cheap and easy to fabricate. However, the device has been tested only through full-wave numerical simulations since the design of a proper feed network for the antennas is quite challenging and some more studies are needed.

The rest of this thesis is structured as follows: first self-adapting phased array antennas are presented, then the two microwave devices for skin cancer detection are described,

and finally the work on gaseous plasma antennas is presented. A final section is dedicated to some general conclusions.

Chapter 2

Self-Adapting Phased-Array Antennas for Changing Surfaces

2.1 Summary

Self-adapting phased array antennas are antennas capable of adapting to surfaces that change shape in time. This feature makes them appealing for different applications in which the antennas are subject to deformations, shifts and vibrations (e.g., wearable devices, vehicle-to-vehicle communications), provided that they can maintain their radiation properties even when they are deformed.

In order to fulfill this requirement, different pattern recovery techniques can be adopted: some are very accurate but also very expensive, while others are simpler and less expensive but also more imprecise. During my Ph.D. I have focused on the projection method (PM) that belongs to the second class of these pattern recovery techniques: this tool is very simple and cost-effective and therefore it can be adopted as a suitable solution for simple antenna systems like those commonly used in small and light-weight wearable devices. In this framework, I have continued the collaboration between our department and the Electrical Engineering Department of the North Dakota State University (NDSU), Fargo, ND, USA: the fabrication and measurement of the antenna architectures presented in the followings took place in NDSU facilities.

The effectiveness of the projection method has been assessed for different scenarios. First, linear and planar broadside arrays placed on surfaces that change shape in time were considered, then planar arrays with beam steering capabilities have been examined, and finally, the phase sensitivity of the projection method was analyzed. For each antenna architecture the strengths and weaknesses of this pattern recovery technique have been stressed and are reported in the followings.

This chapter is organized as follows. First, self-adapting phased array antennas are introduced together with some literature review about the most common pattern recovery techniques and in particular the projection method; then the effectiveness of the PM as applied to linear and planar arrays is discussed; afterwards, the pattern recovery capability of this technique for beam-tilting arrays is debated, and finally its sensitivity to phase variations is described.

2.2 Introduction and Previous Work

Wireless systems have undergone huge developments in the last two decades, finding widespread applications: cellular and sensor networks, aviation communications, wearable devices, and telemedicine are only some examples of technologies that rely on wireless systems. And a lot of other applications are and will be based on wireless communications as well, as for example most of the systems related to smart cities and more in general to the internet-of-things (IoT): vehicle-to-vehicle communications that improve safety and enable traffic control, intelligent and communicating household appliances that allow the end-users to monitor and control their consumes, sensor networks which can monitor a wide range of parameters (e.g., temperature, humidity, light), wearable technologies and telemedicine that have the goal of improving people lifestyle [6].

These novel applications are accompanied by stricter requirements like for example those that are depicted in the design of the 5G new standard for wireless communication: diminished end-to-end latency (from 30-50 ms to 1 ms), higher throughput (from 100 Mbps to 10 Gbps), more connections per km^2 (from 10 K to 1000 K) and technological capability of functioning in high-mobility environments (e.g. high-speed railways where trains travel at a speed higher than 500 km/h) [6] [7].

These new standards demand improvements of consolidated technologies like antennas: they are one of the building blocks of wireless communications, and recent scientific research aims at providing them with more powerful features in order to face present and future challenges.

For example, antenna systems should provide higher directivity and gain, and capability of functioning on changing surfaces: this last feature in particular would allow the placement of antennas on wearable devices that are capable of adapting to body movement [8] [9] [10], or to vibrating surfaces [11] [12] (for example on cars for vehicle-to-vehicle communication purposes).

In this context, self-adapting phased-array antennas have been gaining increasing attention by the scientific community as a feasible solution to this type of problems. In fact,these antennas are capable of adapting to surfaces that change shape in time: the main challenge to face with this kind of phased-arrays consists in maintaining their original radiation pattern when the surfaces on which they are placed changes shape. In fact, when an array changes its original shape, its radiation properties degrade: this usually implicates a reduction in the overall gain of the array, and a diminished directivity of the system. In order to avoid this issue, various compensating techniques can be adopted: from very simple, cheap and easy-to-implement solutions to more performing and complex ones. The choice of the particular technique depends on the requirements of the system and on the inevitable trade-off between performance and ease of implementation.

This work focuses on the projection method, that is a very simple and easy-to-implement pattern recovery technique with a good but limited effectiveness: this can be a valuable solution for applications that prioritize an overall low cost over a very high accuracy, as it is the case of wearable devices. The projection method has been adopted as a pattern recovery technique in several works that can be found in literature, some of

which are briefly described in the followings.

In [13] the PM was used to retrieve the radiation properties of a linear 1×4 conformal array whose shape changes according to two geometries, i.e., a wedge- and an arc-shaped deformations: in particular, a flexible array was fabricated and used to demonstrate the simplicity and low-cost of the projection method. In fact, a flexible resistive sensor was used to measure the deformation of the substrate of the conformal antenna array, while a sensor circuit was used to measure the changing resistance: the circuit uses this information to control the individual voltage of the phase shifters of each radiating element in the array. It is shown that with appropriate phase compensation, the radiation properties of the array can be autonomously recovered as the surface of the flexible array changes shape during normal operation, thus demonstrating the effectiveness and low-cost of the projection method in retrieving the radiation properties of simple broadside linear arrays.

A similar work has been presented in [14]: a 1×4 linear array is placed on a wedge- and on an arc-shaped surface and the PM is used to retrieve the radiation properties of this array. However in this case, the array is not flexible but it is reconfigurable with respect to its operation frequency: each patch antenna composing the array can vary its dimensions thanks to pin diodes connecting the main patch to an additional metallic rectangle. Also in this case the PM proved to be effective in retrieving the radiation pattern of the antenna.

In [15] the PM was used to retrieve the radiation properties of a linear 1×6 patch array placed on an arc-shaped surface and to assess the limits of the pattern recovery technique in compensating the gain loss of the array.

The effect of amplitude tapering as a way to improve the broadside radiation pattern of a 1×6 linear array was investigated in [16]: the amplitude coefficient of each element were computed using the array factor of a conformal antenna and a search algorithm.

Planar conformal arrays were studied as well: a 4×4 array placed on a changing spherical surface was considered in [17], while a 4×4 array placed on a cylindrical surface was analysed in [18]. In both works a sensor circuit is used to measure the radius of the surface deformations (spherical and cylindrical): this information is then used to pilot voltage-controlled phase-shifters in order to retrieve the radiation pattern according to the PM. It must be noted that these works assume to know *a priori* the shape of the surface deformation: the fact that the array bend according to a spherical or a cylindrical shape is given, and the only unknown is the radius of the sphere/cylinder.

Finally the PM was applied to beam-steering arrays in [19] [20]: a 1×4 and a 1×5 patch array were used to assess the effectiveness of the PM in retrieving the pattern of arrays whose beam is tilted towards different directions.

2.3 The Projection Method

As it was mentioned in the introduction, the projection method is a simple, cheap and easy-to-implement pattern recovery technique. The purpose of this section is to provide a general description on the functioning of this method. A more detailed explanation will be given later on for each antenna architecture that has been studied and that will be

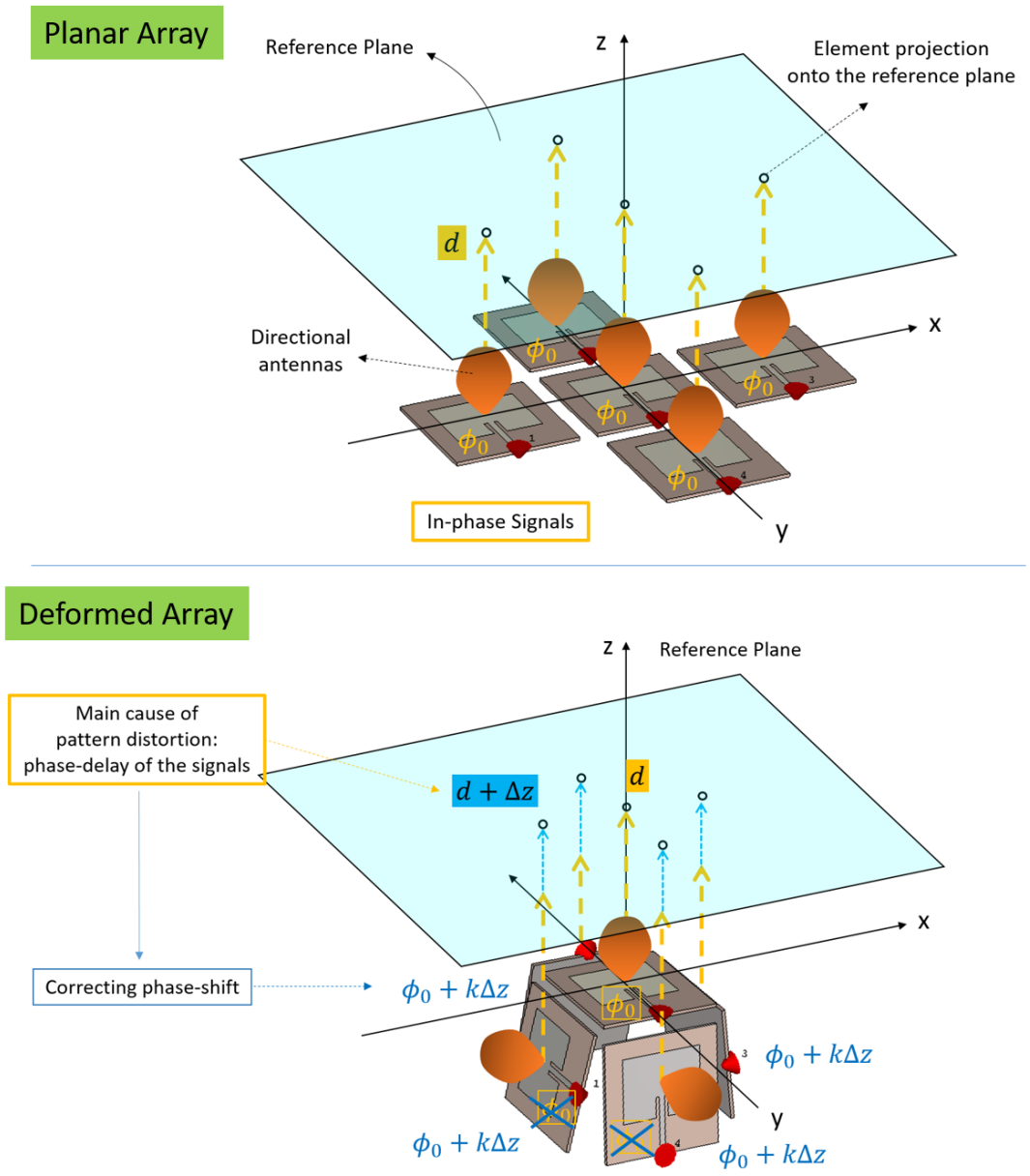

Figure 2.1: Illustration of the general idea behind the projection method: the signals coming from the antennas of the planar array (top figure) arrive in-phase to the reference plane, while those coming from the edge antennas of the deformed array (bottom figure) arrive out-of-phase to the reference plane with respect to the central one.

described in the remaining of this chapter.

Let us consider the planar star-shaped array depicted at the top of Figure 2.1. First of all, we define the *reference plane* (light blue plane in the picture) as one among the infinite planes that are perpendicular to the direction of maximum of the array: in this case we assume a broadside array and therefore the reference plane is parallel to the xy plane. Since the array is broadside, all the elements are fed with signals having the same phase ϕ_0, and we can notice two things:

1. since all the elements (i.e., their *phase-centers*) of the array are placed at the same distance from the reference plane, the signals coming from all the array antennas arrive in-phase to the reference plane;

2. since the array is made of patch antennas, i.e., directional antennas, that are placed on the same plane, the main lobes of these antennas are parallel among each other.

Now, let us assume that the surface onto which the array is placed get deformed according to a box-like shape as depicted at the bottom of Figure 2.1: this implies that the radiation properties of the array degrade as it will be shown in the followings. In this case, we can notice two main differences with respect to the planar configuration:

1. the distance from the reference plane of the elements (i.e., their phase-centers) that are placed at the edges of the array (i.e., all the elements except the central one) is not the same as the distance of the central element;

2. the patch antennas at the edges of the array are tilted with respect to the xy plane and therefore their main lobe is pointing towards different direction with respect to the one of the central element.

The first fact implies that the signals coming from the edges antennas arrive out-of-phase at the reference plane with respect to the signal coming from the central antenna. According to the projection method, this is the main cause of the pattern distortion affecting the deformed array.

In order to retrieve the radiation properties of the array around the direction of maximum, the PM requires that a *compensating phase-shift* is introduced in the array elements at the edge of the array. This phase-shift is proportional to the difference Δz in the distance from the reference plane between the edge elements and the central one and it is given by:

$$\Delta\phi = k\Delta z \tag{2.1}$$

where k is the wave vector in free space. As it will be shown in the next sections, this allows to retrieve the radiation properties of the array; however, its effectiveness is limited around the direction of maximum of the array. This can be easily explained by noticing that the evaluation of the compensation phase-shifts starts by defining a reference plane as a plane orthogonal to the direction of maximum of the array: this means that the PM compensation focuses on re-establishing in-phase signals along the direction of maximum, and it does not take into accounts the radiation pattern of the antennas towards other directions.

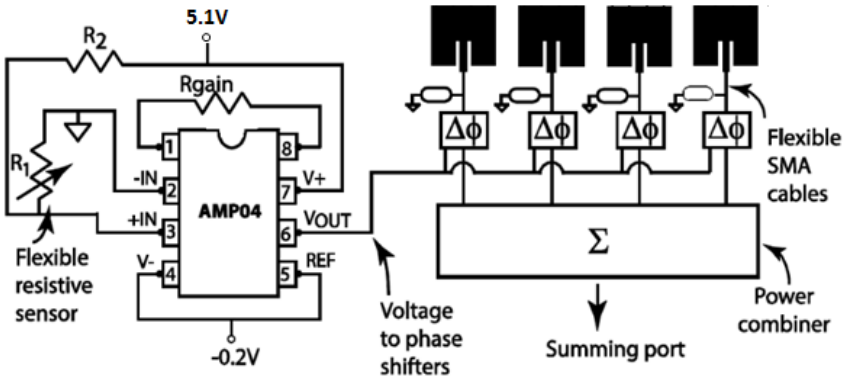

Figure 2.2: Topology of the frequency reconfigurable self-adapting conformal antenna ($R_1 = 1\ M\Omega$ and $R_{gain} = 4\ K\Omega$).

2.4 Pattern Recovery of Linear Phased Array Antennas

In [21] the effectiveness of the projection method was tested through full-wave numerical simulations in CST Microwave Studio and through measurements (conducted at the North Dakota State University (NDSU), Fargo, ND, USA) on some linear arrays placed on deformable surfaces: a 1x4 array placed on an S-shaped surface and a 1x6 array placed on a Z-shaped conformal surface and the prototype used for validation.

As depicted in Figure 2.2, the antenna array consists of microstrip patch antennas each individually connected to voltage controlled phase shifters with identical SMA cables (flexible cables were chosen for placement on various surfaces). The Z- and S-shaped surface deformations are measured by a reconfigurable sensing circuit (as the one presented in [13]) that does not require signal processing or complex algorithms. In fact, the derived compensation algorithm based on the projection method can be autonomously implemented in the reconfigurable array using the simple reconfigurable circuitry with passive components and an operational amplifier (which is much simpler and cost effective than a microprocessor) as it was done in [13]. The circuit then in turn provides an output voltage that drives the voltage controlled phase shifters to implement phase compensation [22].

By choosing the appropriate circuit design, the array in Figure 2.2 can autonomously preserve the radiation pattern using phase compensation, thus confirming the validity of the projection method, as obtained in [13], [15], [20] and proving that this technique is effective even for more complex surfaces than those presented in these works.

2.4.1 Theoretical Framework

Z-shaped 1x6 Array

Figure 2.3 represents the undeformed 1x6 linear array: each element is a patch antenna resonating at $f = 2.45$ GHz, oriented parallel to the xy plane and whose main lobe direction is indicated by the dashed arrows. The distance between adjacent elements is $L = \lambda/2$ and all the elements are in phase, so that the main lobe direction of the entire array coincide with the z-axis, i.e., $\theta = 90^\circ$ (assuming spherical coordinates as shown in

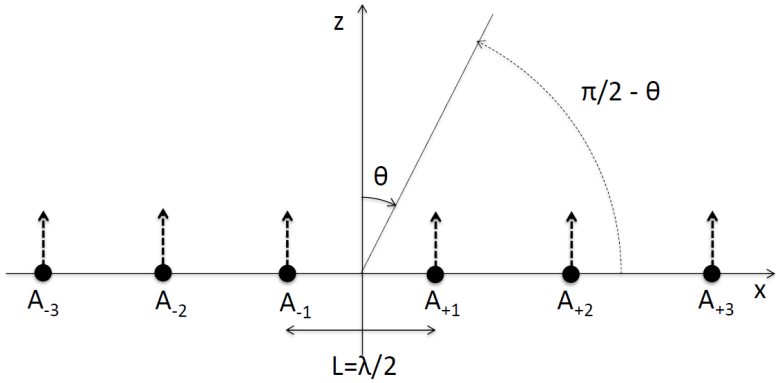

Figure 2.3: 1x6 linear array representation: each element is a patch antenna parallel to the xy plane, whose direction of maximum is indicated by the dashed arrow.

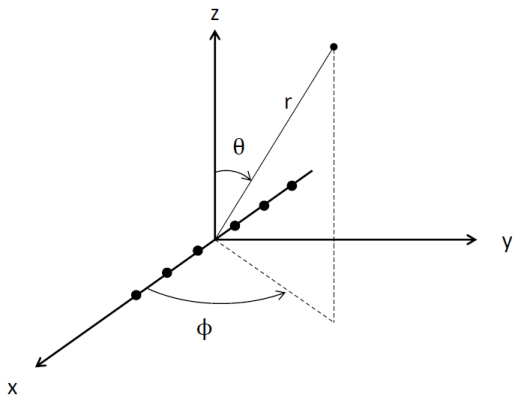

Figure 2.4: Spherical coordinates system.

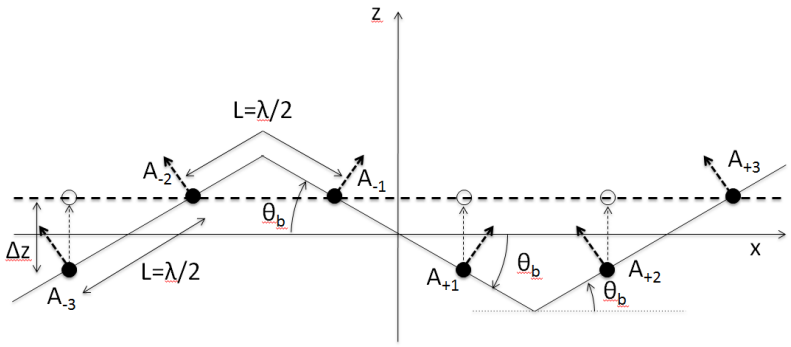

Figure 2.5: 1x6 conformal array placed on a Z-shaped surface: each element is represented by a black dot, whose direction of maximum is indicated by the dashed arrows. The dashed line indicates the new reference plane onto which the elements are projected (the empty dots represent the elements projections onto this plane.

Figure 2.4).

As it will be shown in the followings, when the conformal array is placed on the Z-shaped surface, as depicted in Figure 2.5, the radiation pattern is distorted. In order to recover the radiation properties of the antenna, the projection method is applied and therefore a correcting phase-shift must be introduced in some of the elements of the array.

When the signals radiated by elements A_{-3}, A_{+1}, A_{+2} (see Figure 2.5) arrive at the reference plane (the horizontal dashed line in Figure 2.5), i.e., the plane perpendicular to the main lobe direction of the array, they are out-of-phase with respect to the other elements of the array, and therefore a phase-shift is introduced in order to make these signals arrive in phase with the other elements again (as they were when the surface was linear as depicted in Figure 2.3).

The correcting phase-shift for the i-th antenna of the array is given by:

$$\Delta\phi_i = \Delta z_i \qquad i = -3,\, -2,\, -1,\, 1,\, 2,\, 3 \tag{2.2}$$

where $\Delta\phi_{-2} = \Delta\phi_{-1} = \Delta\phi_3 = 0$ and $\Delta\phi_{-3} = \Delta\phi_1 = \Delta\phi_2 = L\sin\theta_b$, k is the wave number and θ_b is the angle as depicted in Figure 2.5.

It is worth noticing that the main lobe directions of the single patch antennas (dashed arrows starting from the black dots in Figure 2.5) are not parallel to the desired direction of maximum of the array as they were in the linear array (Figure 2.3) and therefore, in order to compute the analytical overall radiation pattern of the array, this information must be considered when evaluating the three dimensional array factor (AF) expression:

$$AF = \sum_{n=-3}^{3} e(\theta-\theta_n) w_n e^{jkx_n \sin\theta\cos\phi + y_n \sin\theta\sin\phi + z_n\cos\theta} \tag{2.3}$$

where $w_n = a_n e^{j\delta}$ is the signal coming from element A_n, $e(\theta)$ is the radiation pattern of antenna A_n that with a peak at $\theta = \theta_n$, and $e(\theta-\theta_n)$ is the radiation pattern of the same element with a peak at $\theta = 0°$ instead, (x_n, y_n, z_n) are the coordinates of the n-th element of the array, and finally θ and ϕ are the height and azimuthal angles in the spherical coordinates system depicted in Figure 2.4. In this specific case we have that $\theta_{-1} = \theta_1 = \theta_b$ and $\theta_{-3} = \theta_{-2} = \theta_2 = \theta_3 = -\theta_b$.

After introducing the correcting phase-shifts into the elements of the array, the AF becomes:

$$AF = \sum_{n=-3}^{3} e(\theta-\theta_n) w_n e^{jkx_n \sin\theta\cos\phi + y_n \sin\theta\sin\phi + z_n\cos\theta} \cdot e^{j\Delta\phi_n} \tag{2.4}$$

S-shaped 1x4 Array

Figure 2.8 represents the 1x4 conformal array of Figure 2.6 after it was bent on an S-shaped surface. In order to apply the projection method and therefore to derive the compensating phase-shifts to be introduced in each array's element, it is useful to understand how this surface deformation has been obtained. As a first step, the linear array in Figure 2.6 was bent on a surface that is the union of two arcs of circumference that are symmetric with respect to the origin, as depicted in Figure 2.7. The elements coordinates are:

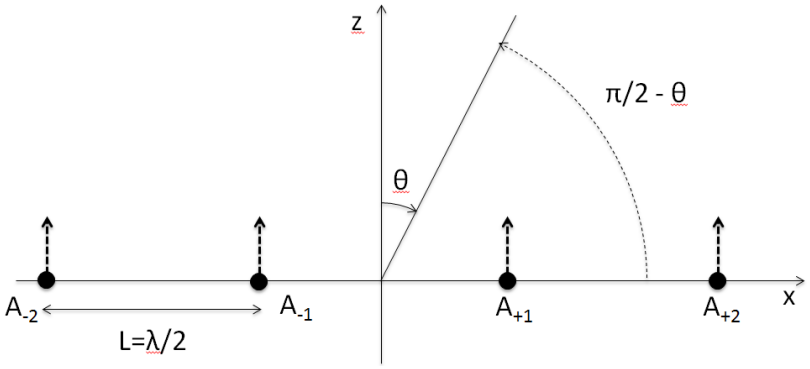

Figure 2.6: 1x4 linear array representation: each element is a patch antenna parallel to the xy plane, whose direction of maximum is indicated by the dashed arrows.

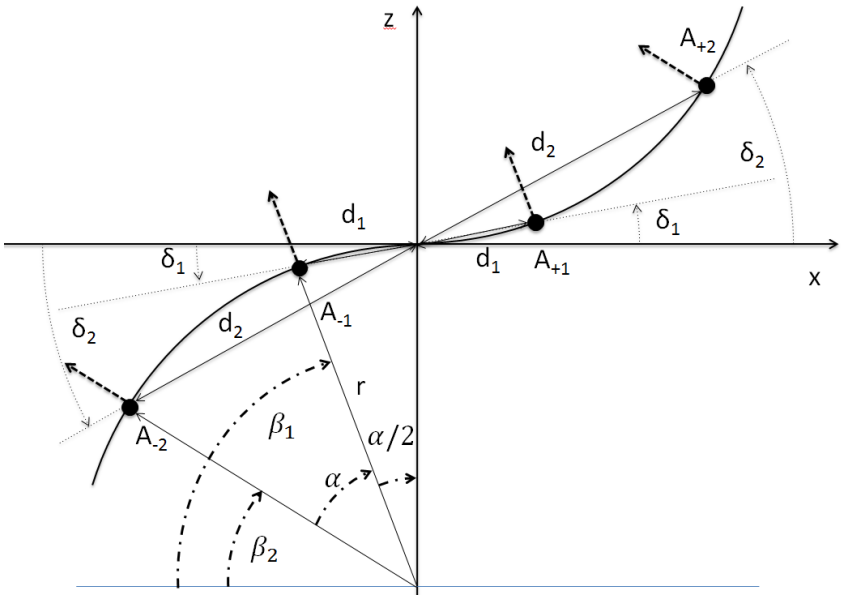

Figure 2.7: 1x4 conformal array placed on two arcs of circumference symmetric to each other with respect to the origin..

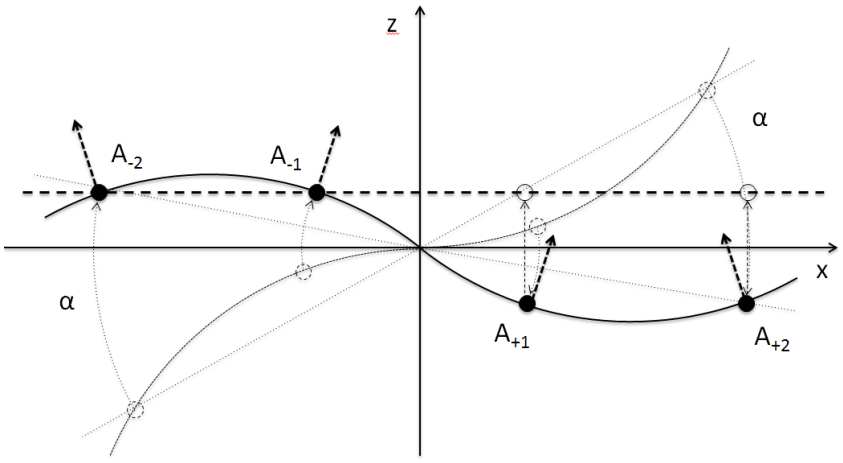

Figure 2.8: 1x4 conformal array placed on a S-shaped surface: each element is represented by a black dot, whose direction of maximum is indicated by the dashed arrows. The dashed line indicates the new reference plane onto which the elements are projected (the empty dots represent the elements projections onto this plane.

$$
\begin{aligned}
A_{-2}: &\ (x^0_{-2},\ 0,\ z^0_{-2}) = (-r\cos\beta_2,\ 0,\ -(r - r\sin\beta_2)) \\
A_{-1}: &\ (x^0_{-1},\ 0,\ z^0_{-1}) = (-r\cos\beta_1,\ 0,\ -(r - r\sin\beta_1)) \\
A_{+1}: &\ (x^0_{+1},\ 0,\ z^0_{+1}) = (+r\cos\beta_1,\ 0,\ +(r - r\sin\beta_1)) \\
A_{+2}: &\ (x^0_{+2},\ 0,\ z^0_{+2}) = (+r\cos\beta_2,\ 0,\ +(r - r\sin\beta_2))
\end{aligned}
$$

where r is the radius of the circumferences to which the arcs belong and $\beta_1,\ \beta_2$ are given by:

$$
\alpha = \frac{L}{r}\,, \qquad \beta_2 = \frac{\pi}{2} - \frac{3}{2}\alpha\,, \qquad \beta_1 = \beta_2 + \alpha
$$

The array was then clock-wise rotated of an angle α, thus obtaining the final configuration represented in Figure 2.8. In order to derive the final elements coordinates, we can define the angles formed by the x-axis and the segment connecting the elements to the axis origin (see Figure 2.7) as:

$$
\begin{aligned}
\delta_2 &= \tan^{-1}\left|\frac{z^0_{-2}}{x^0_{-2}}\right| = \tan^{-1}\left|\frac{z^0_2}{x^0_2}\right| \\
\delta_1 &= \tan^{-1}\left|\frac{z^0_{-1}}{x^0_{-1}}\right| = \tan^{-1}\left|\frac{z^0_1}{x^0_1}\right|
\end{aligned}
$$

and the length of the above-mentioned segments as:

$$
\begin{aligned}
d_2 &= \sqrt{(x^0_{-2})^2 + (z^0_{-2})^2} = \sqrt{(x^0_2)^2 + (z^0_2)^2} \\
d_1 &= \sqrt{(x^0_{-1})^2 + (z^0_{-1})^2} = \sqrt{(x^0_1)^2 + (z^0_1)^2}
\end{aligned}
$$

Therefore the elements coordinates become:

$$
\begin{aligned}
A_{-2}: &\ (x^0_{-2},\ 0,\ z^0_{-2}) = (-d_2\cos(\alpha - \delta_2),\ 0,\ d_2\sin|\alpha - \delta_2|) \\
A_{-1}: &\ (x^0_{-1},\ 0,\ z^0_{-1}) = (-d_1\cos(\alpha - \delta_1),\ 0,\ d_1\sin|\alpha - \delta_1|) \\
A_{+1}: &\ (x^0_{+1},\ 0,\ z^0_{+1}) = (d_1\cos(\alpha - \delta_1),\ 0,\ -d_1\sin|\alpha - \delta_1|) \\
A_{+2}: &\ (x^0_{+2},\ 0,\ z^0_{+2}) = (d_2\cos(\alpha - \delta_2),\ 0,\ -d_2\sin|\alpha - \delta_2|)
\end{aligned}
$$

Now the projection method can be applied: the new reference plane is the plane parallel to the xy plane on which elements A_{-2} and A_{-1} lie, and the correcting phase-shift that

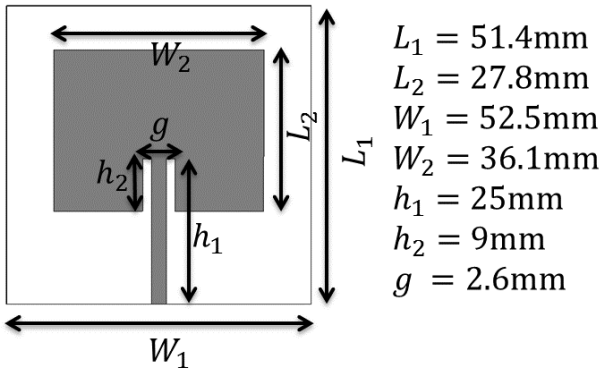

Figure 2.9: Patch antenna design: this is the basic element of all the linear arrays presented here.

must be introduced in elements A_{+2} and A_{+1} is again given by $\Delta\phi = k\Delta z$ where:

$$\Delta z = \Delta z_2 = \Delta z_1 = z_{-1} - z_1 = 2d_1 \sin|\alpha - \delta_1|$$

Finally, in order to compute analytically the radiation pattern of the conformal array, the main lobe directions of the single patch antennas is computed first so that it can be inserted into Equations 2.3, 2.4 to compute the AF expression. After the array is bent along the S-shaped surface but before it is rotated of α degrees (see Figure 2.7), these are given by: $\theta^0_{-2} = \theta^0_2 = -\beta_2$, $\theta^0_{-1} = \theta^0_1 = -\beta_1$. And after the array is rotated of α degrees, they become: $\theta_{-2} = \theta_2 = -\beta_2 + \alpha$ and $\theta_{-1} = \theta_1 = -\beta_1 + \alpha$.

2.4.2 Implementation and Results

The two novel conformal arrays described in the previous section were designed and studied in CST Microwave Studio, moreover two prototypes of the arrays (see Figures 2.10, 2.12) were developed and measured at the facilities of the North Dakota State University (NDSU) of Fargo, North Dakota, USA. In this section the analytical, simulated and measured results for the Z- and S-shaped conformal arrays are presented and it will be shown that they agree. For both the two conformal arrays the single patch antennas are designed to resonate at $f = 2.45$ GHz, with an input impedance of 50Ω. They were simulated in CST on a 1.52 mm thick TMM4 Rogers Substrate with $\epsilon_r = 2.94$ and $\tan\delta = 0.0025$. Referring to Figure 2.9, the values of the parameters in the picture are: $h = 1.52$ mm, $W = 43.70$ mm, $L = 35.33$ mm, $W_0 = 4.1$ mm, $y_0 = 4.1$ mm, $\Delta W = 1.94$ mm.

Z-shaped Conformal Array

Figure 2.11 shows the absolute value of the co-polar component of the electric field $|E_\phi|$ of the Z-shaped array without and with phase-compensation, normalized with respect to the peak value obtained through simulations for the corrected array: the co-polar component is shown, since the cross-polar one (i.e., $|E_\theta|$) is well below -20 dB.

As a first thing, it can be noticed that full-wave numerical simulations agree with the measurements of the prototype depicted in Figure 2.10. If no pattern recovery technique

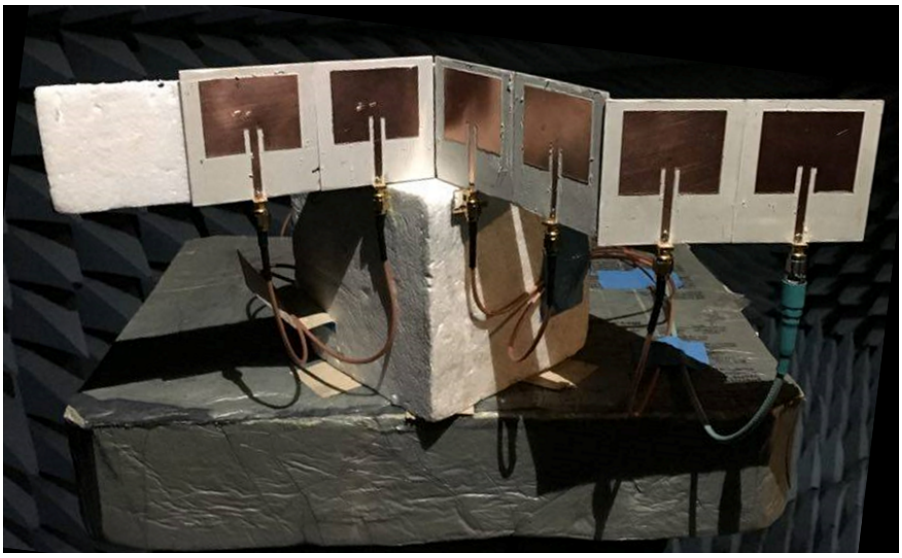

Figure 2.10: Prototype of the fabricated Z-shaped array.

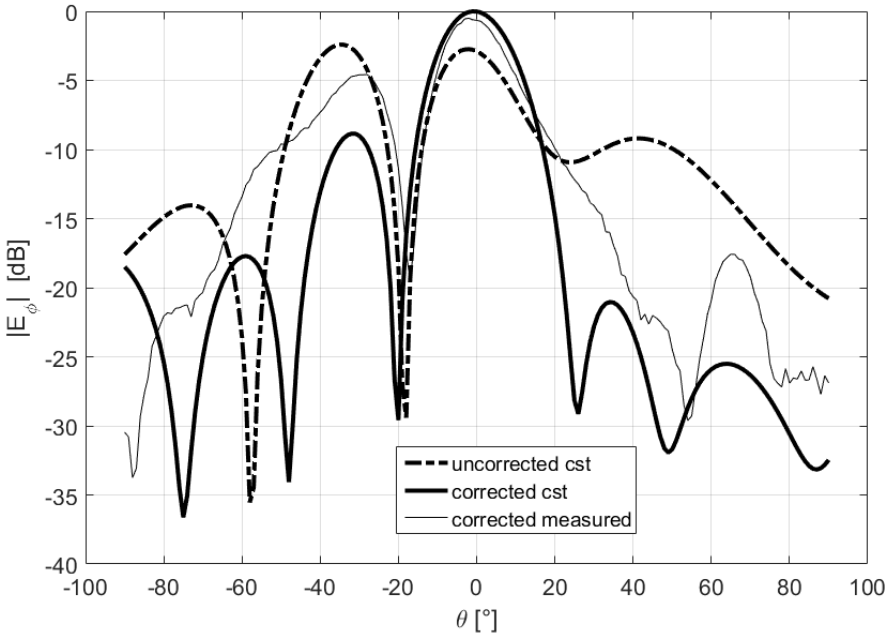

Figure 2.11: Radiation pattern of the Z-shaped conformal array for varying θ and fixed $\phi = 0$: simulated uncorrected (thick dashed line), simulated corrected (thick solid line) and measured corrected (thin solid line) patterns.

is applied, the characteristics of the array change: the main lobe magnitude decreases, the angular width increases, the side lobe level decreases to -7.4 dB and above all a grating lobe appears approximately in the direction $\theta = -35°$. The main benefit of the projection method is the removal of the grating lobe; furthermore with the introduction of the correcting phase-shift, the main lobe magnitude increases, the angular width and the side-lobe levels decrease. The gain of the original flat 1x6 linear array is 12.6 dB, when the array bends it becomes 9 dB while after compensation it increases to 11.8 dB. Therefore it can be said that the radiation pattern is recovered.

S-shaped Conformal Array

As far as the S-shaped conformal array is concerned, once again the projection method proves to be an effective mean for pattern recovery. Figure 2.13 shows the absolute value of the co-polar component of the electric field $|E_\phi|$ of the S-shaped array without and with phase-compensation, normalized with respect to the peak value obtained through simulations for the corrected array: the co-polar component is shown, since the cross-polar one (i.e., $|E_\theta|$) is well below -30 dB. First of all, as in the previous case it can be noticed that simulations and measurements from the realized prototype (represented in Figure 2.12) agree. It can be seen that the main lobe direction changes from 0 to $9°$ with respect to the linear case, and that the side lobe level has consistently increased from -13.8 dB to -6 dB. The gain of the 1x4 undistorted linear array was 11.1 dB, when the array is deformed it becomes 10.5 dB in the new direction of maximum at $\theta = 9°$ while it is only 8.2 dB for $\theta = 0$ (the original direction of maximum); after compensation the gain in the desired direction of maximum (i.e., $\theta = 0°$) increases to 10.8 dB. Applying the projection method the radiation pattern can be recovered: the main lobe direction moves back to zero and the side lobe level decreases to -11 dB.

2.4.3 Conclusions

Therefore in [21] two new conformal arrays were presented: a Z- and an S-shaped array. The projection method was used as a pattern recovery technique in order to compensate for surface deformation: it was shown that this technique is capable of efficiently recover the radiation pattern of the conformal array both through full-wave numerical simulations and through measurements of a realized prototype. These results show how the projection method is an efficient pattern recovery solution even when a conformal array is placed on a complex surface, thus providing a simple and cost-effective technique to preserve the radiation properties of an array. Therefore exploiting this method, the two novel conformal arrays here presented can autonomously recover their radiation pattern.

2.5 Main Lobe Control of a Beam Tilting Deformable Array

The projection method effectiveness was thoroughly studied for many types of antennas: for example, for 1×4 and 1×6 linear arrays placed on surfaces that change shape in time [13] [14] [21], planar arrays subject to cylindrical [18], spherical [17] and asymmetrical [23] surface deformations. All the aforementioned works adopt the PM in order to

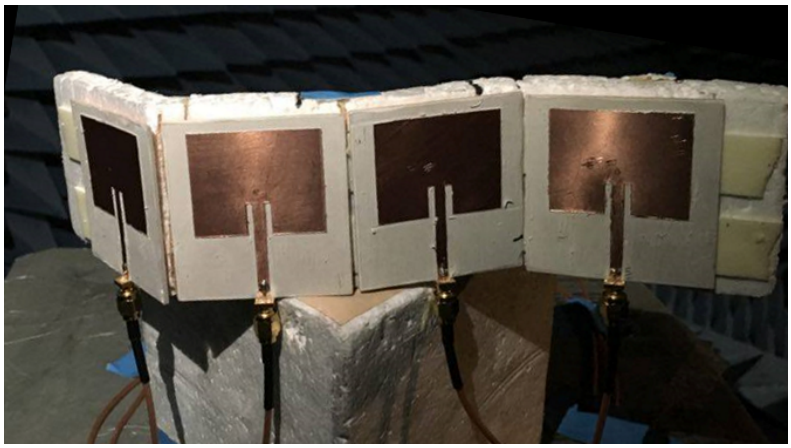

Figure 2.12: Prototype of the fabricated S-shaped array.

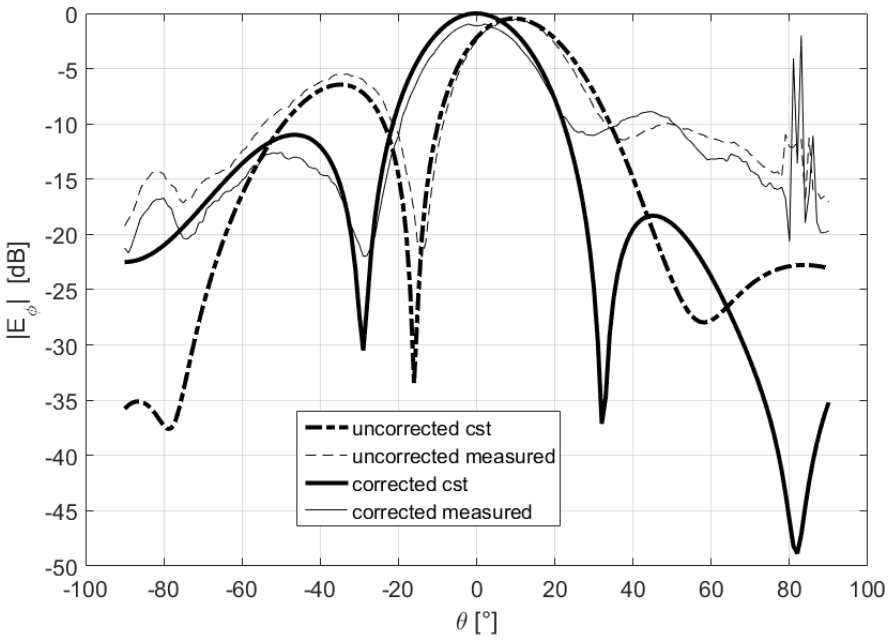

Figure 2.13: Radiation pattern of the S-shaped conformal array for varying θ and fixed $\phi = 0$: simulated uncorrected (thick dashed line), simulated corrected (thick solid line) and measured corrected (thin solid line) patterns.

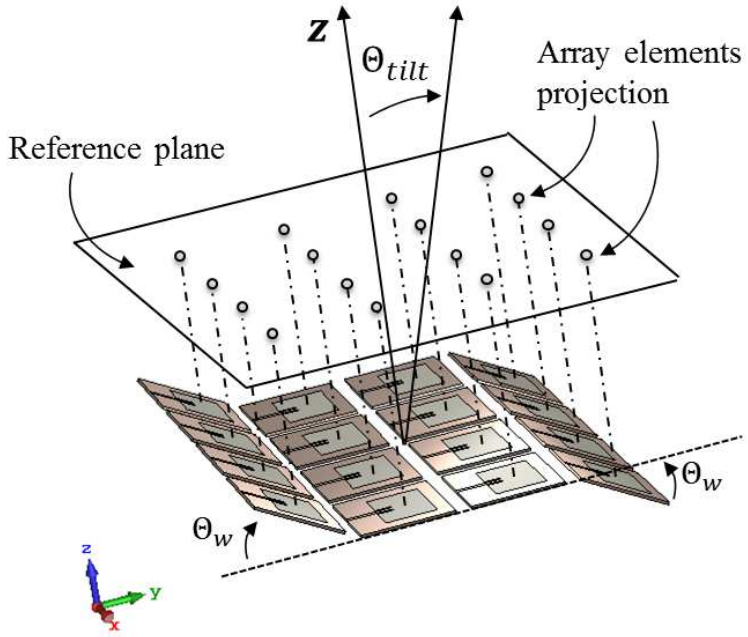

Figure 2.14: Investigated surface deformation.

recover the pattern of *broadside* arrays, but a common requirement when dealing with phased arrays, is to dynamically steer the main lobe towards different desired directions. Some works dealt also with this issue: for example in [19] the effectiveness of the PM is evaluated for a beam-tilting linear 1×5 array placed on a wedge-shaped deformable surface.

However, the vast majority of these works considered surface deformations that were geometrically simple, i.e., they could be described thanks to one or two parameters at maximum (like for example the radius in the case of a sphere or of a cylinder). Therefore in [23] the projection method was applied to a 4x4 planar array placed on a strongly deformed surface. The phase compensation technique is applied first on rows, and then, considering rows as single antenna elements, on array columns .This technique demonstrates to be effective in recovering direction and width at half maximum of the pattern main lobe and in suppressing side lobes. Analytically predicted recovered patterns are confirmed through full-wave numerical simulations.

The main issue of the PM when applied to beam-tilting arrays is related to the fact that it requires the correcting phase-shifts to be function of *both* the surface deformation *and* the main lobe direction. This is because the phase-shifts introduced in the elements have two purposes in this case: *compensating* the array deformation and *steering* the beam towards a desired direction. Therefore it can be seen how the PM is formulated in order to *tilt* the beam of an array taking into account (i.e., compensating) the array deformation; it is not used to retrieve the pattern of a deformed array whose main lobe has *already* been tilted towards a specific direction. This fact complicates the overall system since the phase compensation in this case cannot be simply extracted by the strain sensors data that measure the geometrical deformation (unless this is a-priori known): an additional signal processing step is required in order to *project* the array elements onto a new reference

plane *every time* that the beam is tilted towards a different direction.

In [19] this was not an issue since the deformation geometry was quite simple and a-priori known, and therefore also the analytical relation that linked the phase-shifts to the geometrical deformation and to the tilting angles was a-priori given; but as soon as the deformation becomes slightly more complex (as the one we present here) and/or a-priori *unknown*, the computation of the correcting phase-shifts becomes cumbersome. This is because the shifts cannot be directly computed from the strain sensors data anymore, because a new *analytical* relation between surface deformation, direction of maximum and compensating phase-shifts must be formulated for *each* main-lobe direction and for *each* possible geometrical deformation.

Since we are assuming that this type of arrays are used for simple and cheap devices, we are interested in keeping the overall system complexity and the cost as low as possible. Therefore we decided to express the correcting phase-shifts as the sum of two independent terms: one related to the geometrical deformation, and one related to the main lobe direction. Doing so, it is possible to simplify the system reducing the amount of signal processing required: in fact the first term can be directly extracted from strain sensors data that measure surface deformation, while the second component can be easily pre-computed through basic antenna theory.

As it is shown in the next sections, this approach allowed us to recover the main radiation properties of a doubly wedge-deformed planar array when its beam is tilted up to $40°$.

2.5.1 Theoretical Framework

In order to explain and test our approach, we consider a 4×4 planar array, whose elements are patch microstrip antennas resonating at 2.48 GHz. We will refer to array rows and columns as those sets of elements sharing, respectively, the same y or x coordinate (refer to Figure 2.14 for axes orientation). The array is placed on a surface which is subject to a doubly wedge-like geometrical deformation as depicted in Figure 2.14: the first and last rows of the array are tilted of θ_W degrees. As a consequence of the surface deformation, the array radiation pattern is distorted (as it will be shown in the followings), i.e., the main lobe decreases in gain, and shifts in direction. We will focus only on this particular geometrical deformation as we assume that the array beam is tilted faster than the speed at which the deformation changes shape: this scenario makes it easier to test the validity of our approach.

Let's assume now that we want to steer the beam of this array of θ_{tilt} degrees in the yz plane. In order to do this avoiding excessive pattern distortion, according to the PM (projection method) [19] we must apply phase-shifts that take into account *both* the geometrical deformation of the antenna *and* the desired main lobe direction. These phase-shifts are computed *projecting* the array elements onto the *reference plane*, i.e. the plane chosen among the infinite ones orthogonal to the desired direction of maximum (see Figures 2.15, 2.16): they are proportional to the distance of the elements from the reference plane so that the signals coming from different array elements will arrive with the same phase on this plane.

Referring to Figures 2.15, 2.16, and assuming $\theta_{tilt} = 0$, the deformed array is operating

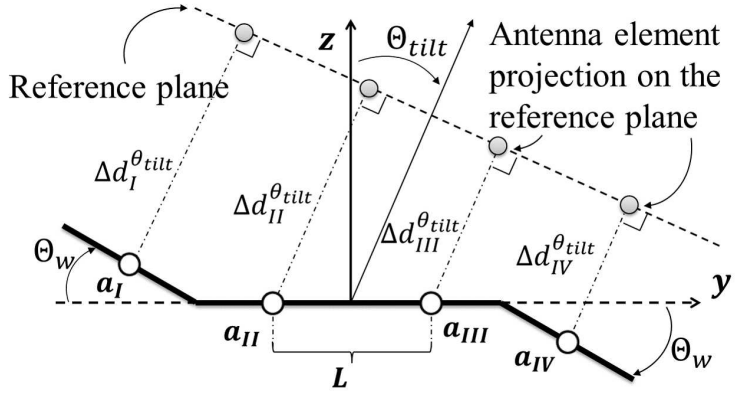

Figure 2.15: Representation of the pattern recovery with the PM for a deformed 4×4 array whose beam is tilted of θ_{tilt}: the reference plane is chosen among the infinite ones perpendicular to the direction of maximum θ_{tilt}, and phase-shifts related to the distances $\Delta d_n^{\theta_{tilt}}$ are introduced in the n-th element (see Section 2).

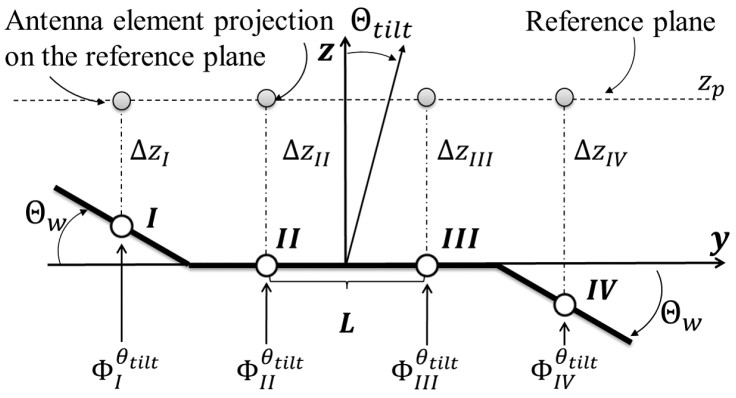

Figure 2.16: Representation of the pattern recovery with our technique for a deformed 4×4 array whose beam is tilted of θ_{tilt}: the reference plane is chosen as if the array were operating in *broadside*, and correcting phase-shifts $\Phi_n^{\theta_{tilt}}$ (different with respect to the one given from the PM) are introduced in the n-th element (see Section 2).

in *broadside* mode, and therefore the reference plane must be chosen among the planes that are parallel to the xy plane: for example in Figure 2.16, the reference plane is represented above this plane in order to stress the fact that *any* of these planes can be chosen as the reference one. For example, a straightforward choice, is to pick exactly the xy plane: in this way the distances of the array elements from it, are simply given by their z coordinates.

In particular, if strain sensors between adjacent antennas are used to measure the surface deformation, then the distance of the elements from the xy plane can be directly computed from the sensors data [13]: no analytical expression of this distance in function of the deformation geometry must be provided.

However, if the main lobe is tilted towards a different direction, then the reference plane will be tilted as well (see Figure 2.14), and this implies that the distances between the elements and the new reference plane cannot be simply evinced from the information provided by the strain sensors. Consequently, an analytical relation linking the correcting phase-shifts to the geometrical deformation and to the *tilted* reference plane must be introduced as it has been done in [19]. Now, this can be easily done if the geometrical deformation is simple or a-priori known (as it was in [19]), but if this is not the case, then it can be difficult to evaluate the compensating phase-shifts, since an analytical expression of these quantities must be available for *each* geometrical deformation and for *each* steering angle.

Our goal is to keep the system complexity as low as possible, and therefore we want to show that it's possible to retrieve the array radiation pattern even if we skip this last signal processing step that requires the computation of a new analytical relation *every time* that either the steering angle or the surface deformation change. In order to do this, we express the overall phase-shift to be introduced into the n-th element (see Figure 2.16) as the sum of two terms:

$$\phi_n^{\theta_{tilt}} = \alpha_n^{corr} + \alpha_n^{\theta_{tilt}} \tag{2.5}$$

where $\alpha_n^{corr} = k\Delta z_n^{broad}$ are the terms that have the function of *correcting* the surface deformation and coincide with the phase-shifts required by the PM to retrieve the pattern of the *broadside* array (they are given by the product between the wave vector k and Δd_n in Figure 2.16); while $\alpha_n^{\theta_{tilt}}$ is simply the phase-shift that must be introduced into the n-th element of the *undeformed* planar array in order to steer its main lobe into the desired direction. The first term can be directly computed from the strain sensors data that measure surface deformation, while the second term can be easily pre-computed for a set of angles of interest according to basic antenna theory and stored in a small memory or look-up table into the device. Therefore with this approach, no analytical expression of the phase-shifts in function of the geometrical deformation and of the steering angle is required and no further processing steps are necessary.

Let us make a comparison between the two approaches in terms of correcting phase-shifts. As far as the PM is concerned, we will refer to the geometrical deformation represented in Figure 2.15. Among the infinite planes orthogonal to the direction of maximum, we choose as the reference one, the plane that is touching element a_{IV} (in Figure 2.15) we actually chose to depict another reference plane, further from the array, for ease of read of the figure). The correcting phase-shifts $\psi_n\,,\ n = 1, \ldots, 4$ to be introduced into

elements $a_I, \ldots, a_{IV}$ respectively, are function both of the geometry of the deformation and of the steering angle and they are given by:

$$\psi_4 = 0 \tag{2.6}$$
$$\psi_3 = L/2[\sin(\theta_{tilt} - \theta_w) + \sin(\theta_{tilt})] \tag{2.7}$$
$$\psi_2 = \psi_3 + L\sin(\theta_{tilt}) \tag{2.8}$$
$$\psi_1 = \psi_2 + L/2[\sin(\theta_{tilt} - \theta_w) + \sin(\theta_{tilt})] \tag{2.9}$$

As it can be noticed, this expression can be cumbersome to evaluate, especially considering that the geometrical deformation may not be a-priori known and that it could further change in shape and become even more complex than the one presented here (e.g., it could change to a three-dimensional deformation as the one studied in [23]).

According to our approach instead, the overall phases to be applied to the elements are given by the sum of two terms that can be evinced from sensors data and pre-computed. The terms responsible for the deformation compensation are given by: $\alpha_4^{corr} = -\alpha_1^{corr} = 45°$, $\alpha_2^{corr} = \alpha_3^{corr} = 0°$, while those responsible of tilting the beam towards a set of sample directions are given in Table 1 and have been computed according to [24]. As it is shown in the next section, this approach proves to be effective in recovering the radiation pattern of the conformal array when the main lobe is tilted from $\theta_{tilt} = 0^{\circ}$ up to $\theta_{tilt} = 40^{\circ}$.

Table 1. Beam steering phases.

Beam Steering Phases	Array $i-$th row	θ_{tilt} $0°$	$15°$	$25°$	$40°$
$\alpha_n^{\theta_{tilt}}(°)$	I	0	70	155	200
	II	0	20	65	65
	III	0	-20	-65	-65
	IV	0	-70	-155	-200

2.5.2 Experimental Results

Four-by-Four Elements Array

Our experimental set-up consisted of a planar array capable of steering the beam along the y direction of θ_{tilt} degrees. The array is then placed on a surface that is deformed in a doubly-wedge shape with $\theta_w = 30°$ (see Figure 2.14). The radiation pattern of the *planar* array for different tilt angles ($\theta_{tilt} = 15°, 25°, 40°$) is taken as the reference pattern to be retrieved. Full-wave numerical simulations were performed in CST Microwave Studio and a prototype of the 4×4 array was fabricated and measured in an anechoic chamber (see Figure 2.17) reports a picture of the realized prototype). The phase of each patch antenna was controlled through a phase shifter (Hittite: HMC928LP5E).

Each of the Figures 2.18-2.20 contains four graphs: the radiation pattern of the planar array (i.e., our target to retrieve), the distorted pattern of the deformed array, the pattern

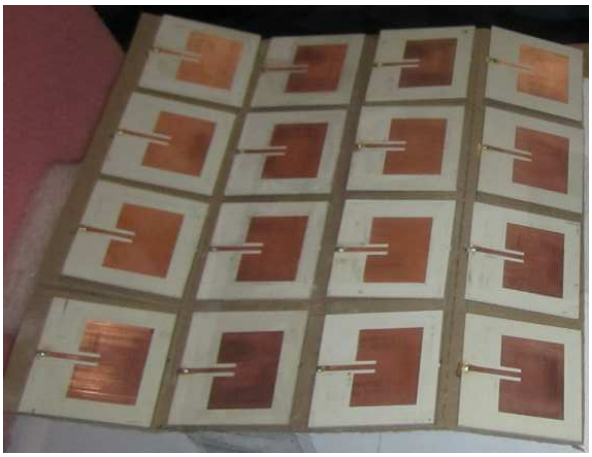

Figure 2.17: Fabricated 4×4 array prototype.

corrected according to our approach and the pattern corrected according to the current formulation of the PM (see previous section). For the last three graphs, both numerical and measurement results are shown. From all the three Figures it can be seen how the geometrical deformation results in pattern distortion with respect to the planar array: the main lobe is shifted of approximately 10° and its magnitude is reduced of about 1 dB; moreover at some frequencies where the planar array has a null, the deformed array has instead a considerably high gain value value (e.g., when $\theta_{tilt} = 15^\circ$ the planar array gain has a zero at $\theta = 45^\circ$, the one of the deformed array is still between 5 dB and 10 dB). We can compare our approach to the PM by noting that it is still effective in retrieving the main radiation feature of the deformed array, i.e., it is able to shift the main lobe back to the desired direction. It is also able to reduce the gain value in correspondence of the nulls of the planar array, even if in this case the PM performs better.

As far as mutual coupling is concerned, this depends on the reciprocal distance and orientation of adjacent elements in the array, and therefore we expect that it will depend also on the deformation geometry, e.g., if the deformation is such that the main lobes of two adjacent antennas are tilted towards each other (as in the case of elements I and II in Figure 2.16) we expect a higher coupling (i.e., a higher value of $S_{I,II}$) with respect to the planar array; in a similar way, if the deformation is such that the main lobes of two adjacent antennas are tilted away from each other (as in the case of elements III and IV in Figure 2.16) we expect a lower value of $S_{I,II}$ with respect to the planar array. Our guess is confirmed by the results reported in Figure 2.21. From this we can notice that in this particular case, the mutual coupling level in the deformed array are similar to those of the undeformed array: this is again what we expected since adjacent antennas are not strongly tilted towards/away from each other. Therefore we can say that mutual coupling is negligible in a *relative* way, i.e., with respect to the planar array, recalling that our goal was not to get *low* coupling levels, but to get coupling levels similar to the ones of the undeformed array.

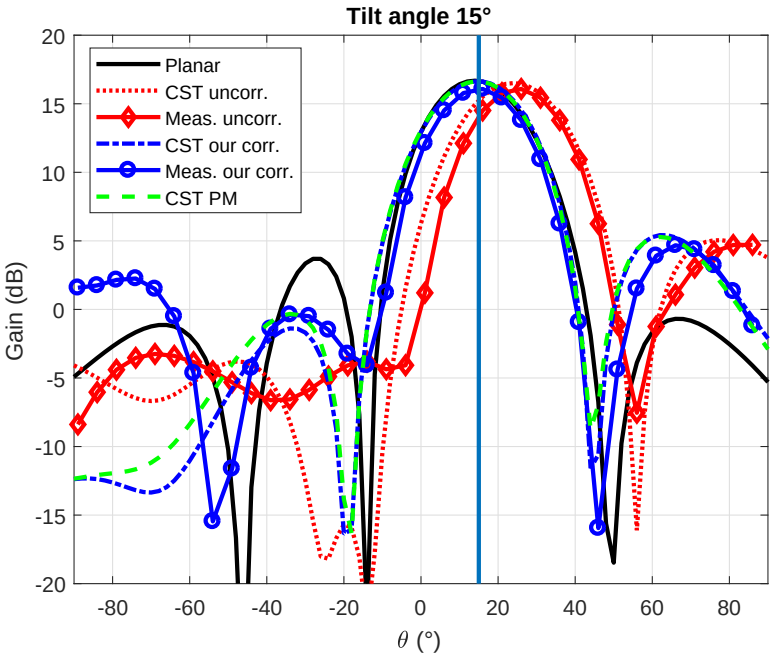

Figure 2.18: Simulated and measured 4×4 antenna gain: planar, uncorrected, corrected with our approach and with the projection method patterns on the $yz-$plane for $\theta_{tilt} = 15°$.

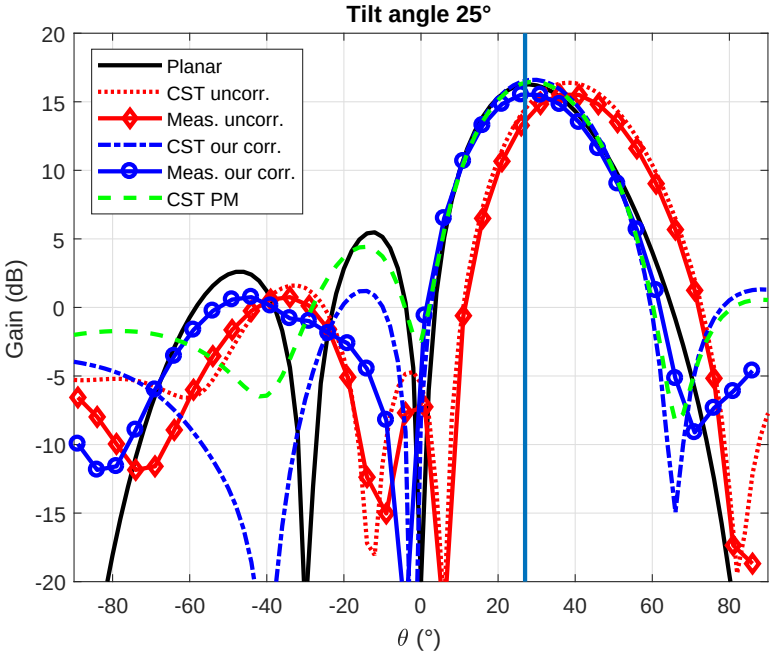

Figure 2.19: Simulated and measured 4×4 antenna gain: planar, uncorrected, corrected with our approach and with the projection method patterns on the $yz-$plane for $\theta_{tilt} = 25°$.

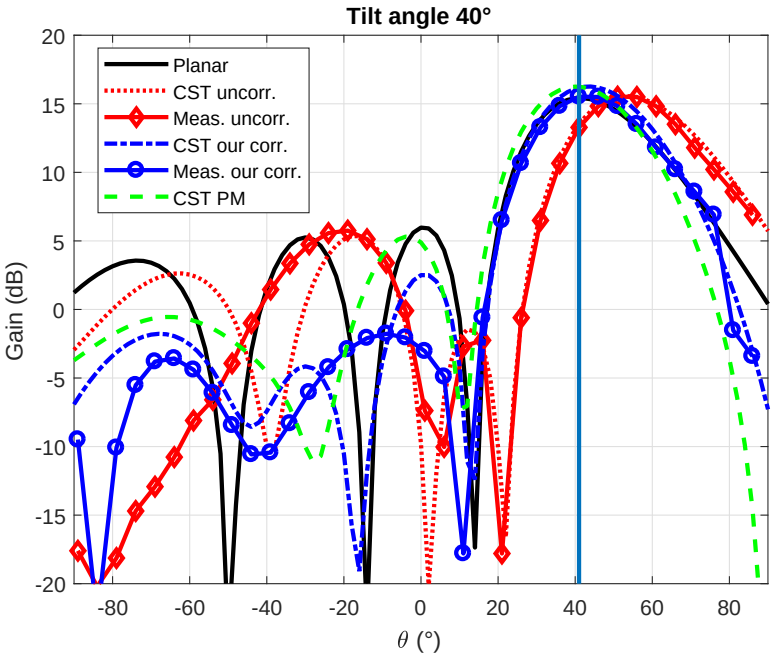

Figure 2.20: Simulated and measured 4×4 antenna gain: planar, uncorrected, corrected with our approach and with the projection method patterns on the $yz-$plane for $\theta_{tilt} = 40°$.

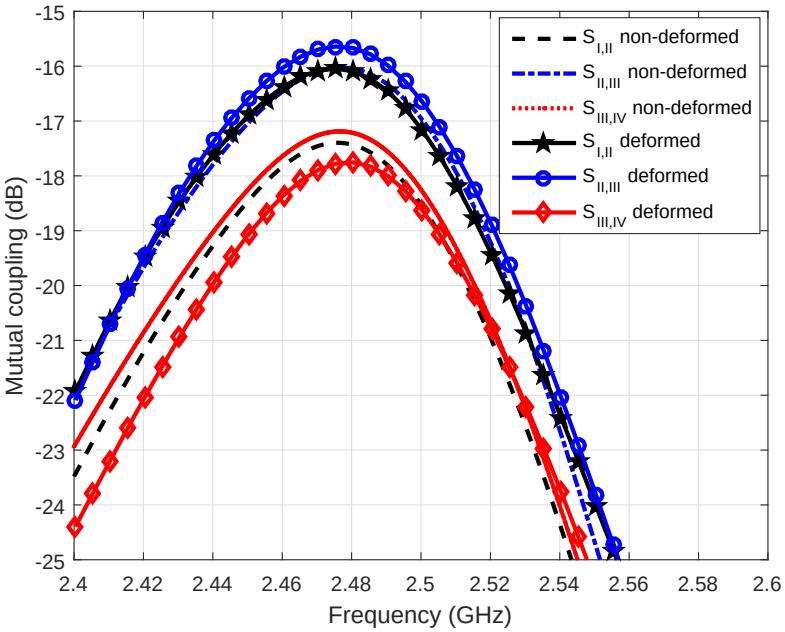

Figure 2.21: Relevant changes in mutual coupling effects after surface deformation of 4×4 array.

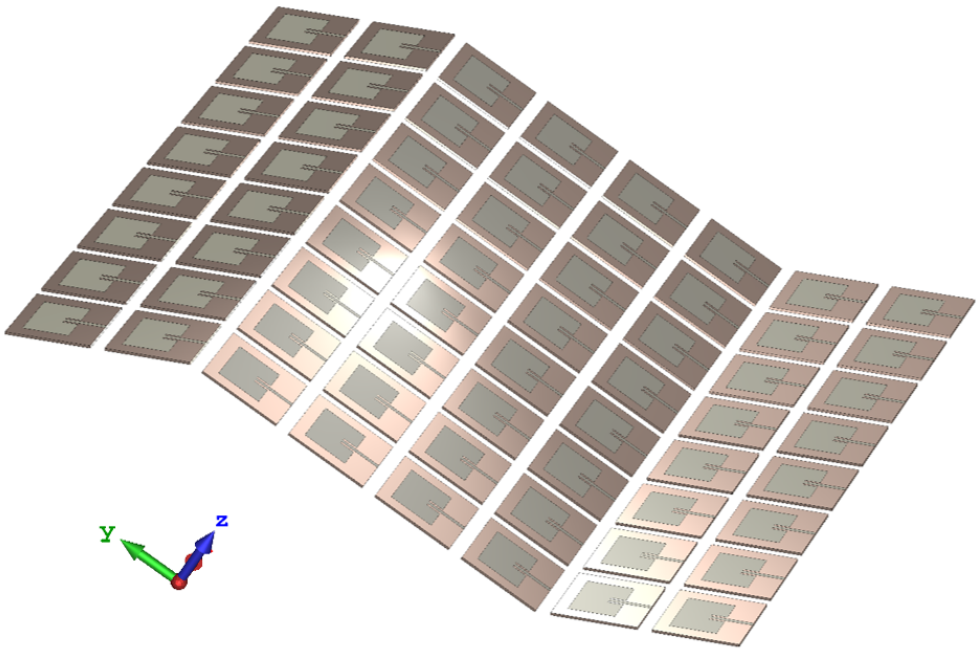

Figure 2.22: Investigated surface deformation for the 8x8 array.

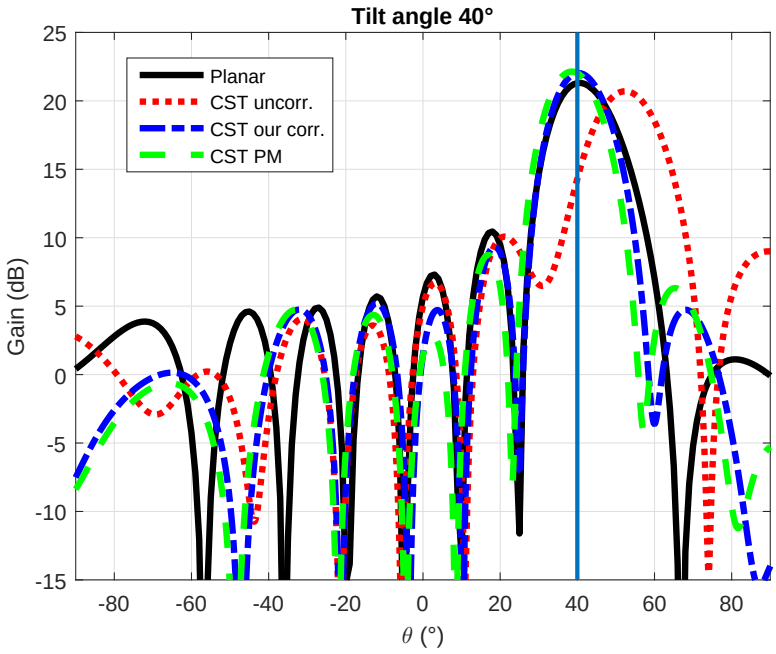

Figure 2.23: Simulated 8×8 antenna gain: planar, uncorrected, corrected with our approach and with the projection method patterns on the $yz-$plane for $\theta_{tilt} = 40°$.

2.5.3 Eight-by-Eight Elements Array

Our pattern recovery approach is valid also when dealing with larger beam-tilting arrays placed on a deformed surface. This has been proven through full-wave numerical simulations on an 8×8 array shaped according to a similar geometry (see Figure 2.22) with respect to the one presented in the previous section (see Figure 2.14). When beam-tilting weights are applied to the 64-elements array, the radiation pattern is distorted and the main beam is not tilted towards the desired direction. Therefore we applied our pattern recovery technique and compared it with the projection method in order to assess its effectiveness.

In Figure 2.23 the results are reported for the worst case scenario among the three discussed above: this is when the beam is tilted towards $40°$. The reference pattern is the one of a planar 8×8 array that steers the beam in the desired direction: it can be seen again how our approach can retrieve the radiation pattern and it is still valid when compared to the projection method.

2.6 Conclusion

In [25] a simplification of the projection method to retrieve the radiation pattern of beam-tilting antennas was proposed. The PM requires that the phase-shifts are analytical functions of *both* the deformation geometry S *and* the main lobe direction, i.e., $\psi_n = \psi_n(S, \theta_{tilt})$, thus requiring to provide an analytical formulation of these quantities for *every* geometrical deformation and for *every* steering angle. This introduces a further processing step and complicates the overall system.

The proposed approach instead, requires the computation of the phase-shifts as the sum of two components: $\phi_n^{\theta_{tilt}} = \phi_n(S) + \phi_n(\theta_{tilt}) = \alpha_n^{corr} + \alpha_n^{\theta_{tilt}}$, where the first one is responsible for deformation compensation, and the second one tilts the beam of the *planar* array towards the desired direction. The first term can be directly linked to the data acquired by simple sensors that measure surface deformation and the second one can be pre-computed according to basic antenna theory, so no analytical expression is required. It was shown through full-wave numerical simulations and measurements that our approach is still effective in retrieving the radiation properties of a deformed array, providing a straightforward and cheap pattern recovery technique suitable for simple low-cost systems.

2.7 Pattern Recovering of Planar Antenna Arrays Placed on Strongly Deformed Changing Surfaces

In [21] the projection method was applied to two *linear* arrays placed on complex surfaces, so the next logical step was to test the effectiveness of this pattern recovery techniques in retrieving the radiation properties of *planar* arrays placed on surfaces that change shape in time. In literature various works can be found on the subject: the PM has been applied to planar arrays placed on surfaces with different geometrical profiles, e.g., cylindrical and spherical, and it proved to be effective in retrieving their radiation pattern of these

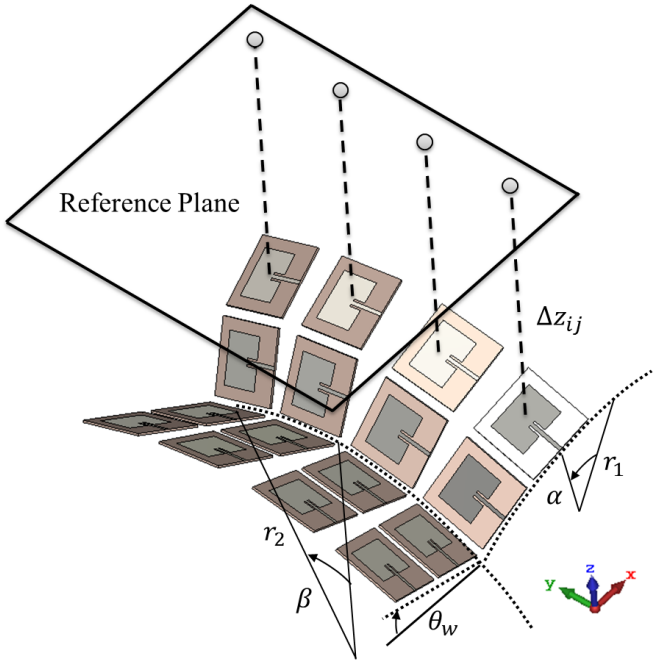

Figure 2.24: Investigated array surface deformation.

conformal arrays.

2.7.1 Implementation

We considered a planar 4x4 microstrip patch antenna array where each element is designed to resonate at 2.45 GHz (they are the same as the one depicted in Figure 2.9) and where the elements are spaced of $\lambda/2$ with respect to adjacent antennas. The array has been placed on a surface whose shape can be deformed. The array under investigation is depicted in Figure 2.24 this kind of deformation is particularly relevant with respect to those analyzed in the previous works, as it implies a pattern degradation along both the $\phi = 0°$ (yz-) and the $\phi = 90°$ (xz-) plane. As a consequence of the surface deformation, radiation properties of the array result to be strongly degraded. According to the projection method, pattern distortion is mainly caused by a relative phase change in the signals coming from different elements of the array: with the introduction of a proper phase-shift in some of the elements of the array, radiation pattern distortion can be mitigated.

In order to analytically determine the correcting phase-shifts to compensate the radiation pattern, it is worth observing that the parameters controlling the deformation are the wedge angle θ_W, and the radii of curvature of the two cylinders r_1 and r_2. Array rows indicate elements sharing the same y-coordinate and they are numbered with an increasing index $i = 1, \ldots, 4$. Analogously, array columns indicate elements sharing the same x-coordinate and are numbered with an increasing index $j = 1, \ldots, 4$.

Consider now a reference plane parallel to the initial flat undeformed array: the phase corrections to be introduced to each patch antenna input is proportional to the distance between each element and its projection on the plane:

$$\Delta\phi_{ij} = k\Delta z_{ij} \tag{2.10}$$

with:

$$\Delta z_{ij} = r_2(1 - \cos\beta_i + h_j \cos\beta_i) \tag{2.11}$$

where h_j for the i-th row is:

$$h_1 = \left(d + \frac{d}{2}\right) \sin\theta_W \tag{2.12}$$

$$h_2 = \frac{d}{2} \sin\theta_W \tag{2.13}$$

$$h_3 = r_1 \sin\alpha_1 \tag{2.14}$$

$$h_4 = r_1 \sin\alpha_2 \tag{2.15}$$

$$\tag{2.16}$$

As the deformation gets more accentuated, limitations of the recovery technique have been evaluated. Afterwards, the phase sensitivity of the projection method has been examined: with the main lobe tilted towards $40°$ along the xz-plane, the radiation pattern has been retrieved imposing phases values with different precision. Consequently, the accuracy of the equipment needed, i.e., the phase shifter typology required, can be established.

2.7.2 Robustness of the Projection Method

Main Lobe Gain: Parametrical Study

The projection method has been applied in order to recover the radiation pattern of the deformed antenna array. In this section the performances of the approach are analyzed: the limitations in retrieving the main lobe pattern have been investigated for increasing deformation relevance. A CST numerical study has initially been performed, where geometrical parameters controlling the deformation were progressively increased and the correcting phase shifts consequently computed using Equations 2.10-2.16. The gain of the main lobe has been accordingly evaluated and a threshold has been chosen to define (set) a limit of the projection method effectiveness.

Figure 2.25 illustrates the difference between the peak gain of the retrieved pattern with the one of the planar array, i.e., the one we ideally wanted to retrieve, when the main lobe direction is broadside. As the deformation increases, it can be observed how the performances of the projection method deteriorate: the gain of the antenna attached to the conformal surface drops below the one of the flat array. Parameters controlling the deformation have been swept in the following ranges:

$$\theta_W : \ 0° \div 30° \qquad r_1 : \ 100\,mm \div 150\,mm \qquad r_2 : \ 150\,mm \div 250\,mm \tag{2.17}$$

Furthermore, the planar case ($r_1 = \inf$ and $r_2 = \inf$) has been considered. A reasonable threshold value of ΔGain=1.5 dB has been chosen, which corresponds to a deformation defined by $\theta_W = 30°$, $r_1 = 200$ mm and $r_2 = 125$ mm. This was set as the limit deforma-

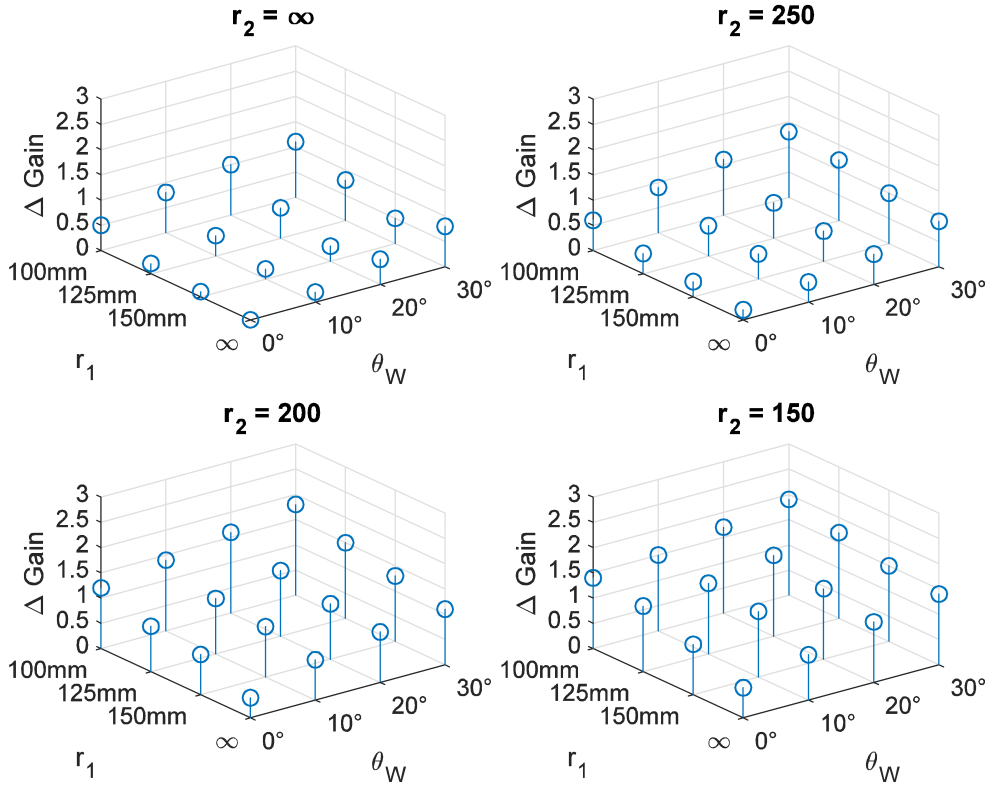

Figure 2.25: Peak gain difference between planar array and conformal array with phase corrections.

$\Delta\phi_{ij}$					
$\delta = 0°$	i,j	***I***	***II***	***III***	***IV***
	I	102.21°	186.78°	159.81°	54.78°
	II	49.71°	138.36°	110.07°	0°
	III	49.71°	138.36°	110.07°	0°
	IV	102.21°	186.78°	159.81°	54.78°
$\delta = 5.625°$	i,j	***I***	***II***	***III***	***IV***
	I	101.25°	185.625°	157.5°	56.25°
	II	50.625°	140.625°	112.5°	0°
	III	50.625°	140.625°	112.5°	0°
	IV	101.25°	185.625°	157.5°	56.25°
$\delta = 22.5°$	i,j	***I***	***II***	***III***	***IV***
	I	112.5°	180°	157.5°	45°
	II	45°	135°	112.5°	0°
	III	45°	135°	112.5°	0°
	IV	112.5°	180°	157.5°	45°

Figure 2.26: Compensating phase shifts for resolution $\delta = 0°, 5.625°, 22.5°$.

tion that can be recovered using the projection method for the considered configuration.

Phase Sensitivity Analysis

When moving to a practical implementation of the projection method, phase corrections as derived in Equations 2.10-2.16 cannot be applied with the same degree of precision of a simulation scenario. In fact, depending on the phase shifter used in a realistic system, a certain degree of approximation has to be assumed. Therefore, the resolution of the phase shifters may influence the effectiveness of the method. For example, if digital phase shifters are used in the setup under consideration, only discrete phase steps are allowed.

In this section, a numerical analysis supported by CST simulations is carried out in order to study the phase sensitivity of the projection method for different approximations of correcting phase shifts. A comparison between the retrieved pattern with different precision induced phases is shown. An evaluation in this regard is believed to be necessary since the equipment costs can vary dramatically as the desired precision level increases, affecting in this way the overall convenience of the method. The surface deformation depicted in Figure 2.24 was maintained while the main lobe direction was tilted towards $\theta = 40°$ in the xz- plane. As stated in [25], in order to retrieve the pattern, it is sufficient to add the compensation for the broadside configuration to the phases imposed to steer the beam.

CST simulations have been performed using the phase shifts described in Figure

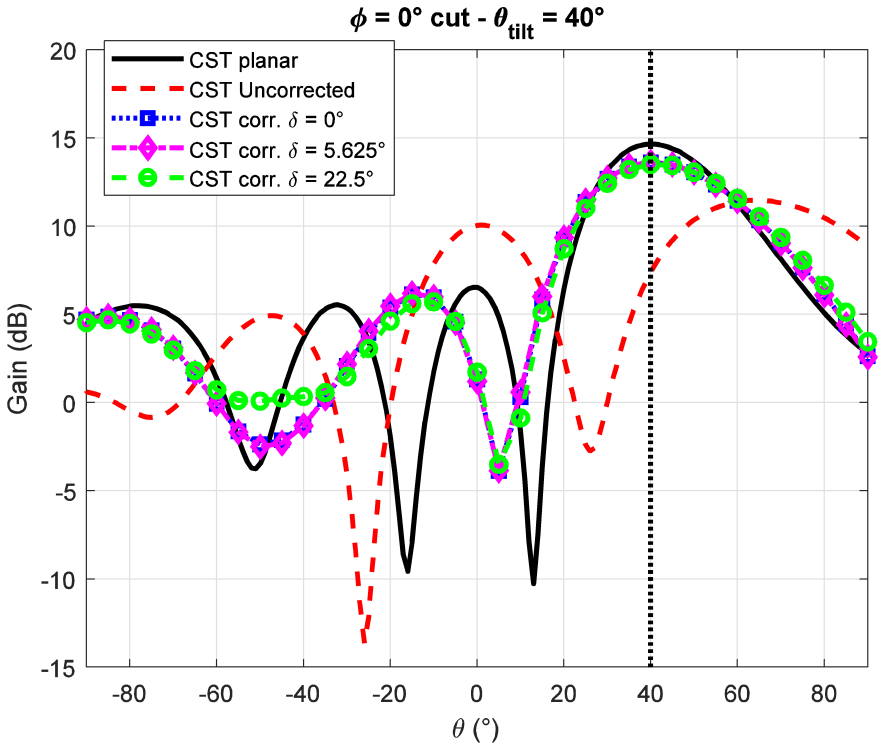

Figure 2.27: Gain pattern of the array retrieved for different phase shifters precision.

2.26. The superscript $\delta(^\circ)$ indicates the rounding made on the phase impressed to array elements with respect to its exact value as derived by the previous analysis. Rows with $\delta = 0^\circ$ indicate the ideal case, where continuum values can be applied, which is assumed as reference for comparison, while $\delta = 5.625^\circ$ and $\delta = 22.5^\circ$ refer respectively, to phase steps of 6-bit or 4-bit digital phase shifters.

Results are depicted in Figure 2.27. Marked lines represent radiation patterns retrieved with different phase precision δ. In order to visually appreciate the effectiveness of the method, the red dashed line shows the simulated radiation pattern of the deformed array while the black solid line is the gain of the planar array (i.e., the one we ideally want to recover).

We can conclude that any of the considered phase precisions allows to recover the pattern with a good degree of accuracy. In fact, the direction of departure is restored together with the main lobe gain. At the same time the side lobe levels are substantially lowered and only small differences can be noticed between patterns retrieved with different δ.

Experimental Validation

A prototype of the array was manufactured and placed on a deformable surface; a picture of the experimental setup is shown in Figure 2.28. The maximum surface deformation obtained after the numerical analysis is shown on the right hand side of the picture. In order to control the input phase of each patch antenna, a network of phase shifters was connected to it. Accordingly with what was said in the previous section, phase shifters steps of $\delta = 22.5^\circ$ have been used for the experimental validation of the method. Figures 2.29, 2.30 show the radiation pattern for the broadside case in the xz- and yz-

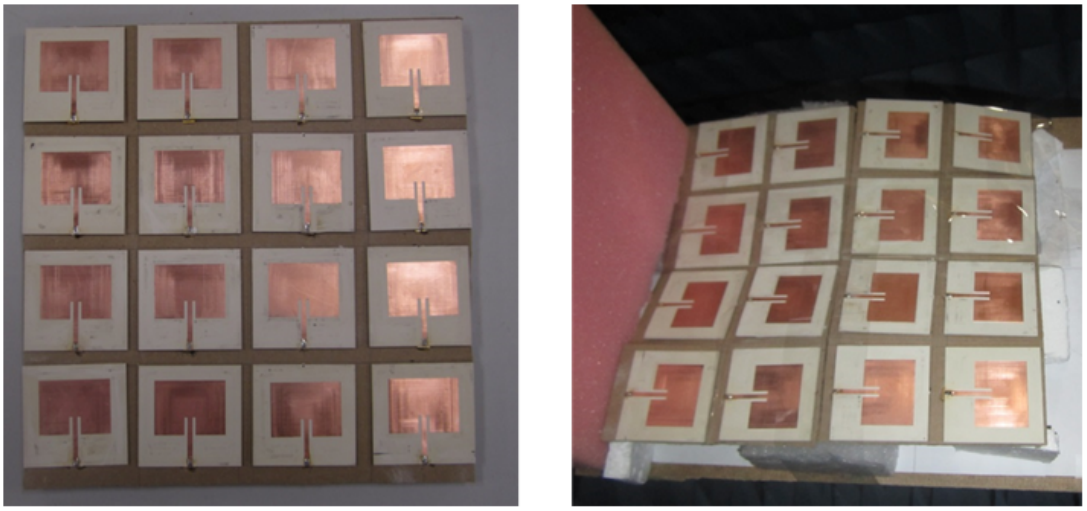

Figure 2.28: Fabricated prototype of the antenna design described in Figure 2.24 (on the right) and of the planar (i.e., undeformed) 4x4 array.

planes, before and after the phase correction. A comparison with the radiation pattern of the initial planar array can be evaluated. Simulated and measured results are plotted respectively with solid/dashed and marked lines. Red lines represent the radiation pattern of the deformed array. A substantial improvement can be appreciated when the correcting phase shifts are applied (blue lines): the main lobe gain figure is retrieved and the broadside direction is restored. At the same time, side lobe levels are lowered and nulls around $\theta = \pm 30^\circ$ are re-established as well as the half-power bandwidth (HPBW).

Furthermore, an experimental validation for the beam steering case is shown in Figure 2.31. The red dashed lines show the distortion induced on the gain pattern when the array was deformed and the main lobe had been tilted of $\theta_{tilt} = 40^\circ$. The blue lines represent the retrieved radiation pattern. A substantial mitigation of the distortion effects can be observed by comparing the latter to the black lines showing the radiation pattern of the planar, undeformed, array. Measurements confirmed simulation results and proved the overall effectiveness of the method.

Conclusions

The projection method has been applied in order to recover the radiation pattern of an asymmetrically deformed antenna array. A limit on the surface deformation has been established, such that the peak gain of the retrieved pattern did not drop below 1.5 dB with respect to the pattern of the planar array; geometrical parameters were fixed accordingly. Furthermore, the phase precision needed by the phase shifters used for a practical implementation has been evaluated. A 4-bit digital phase shifter can be effectively used, thus maintaining the overall setup cost low. For the deformation described by the chosen parameters, experimental results have confirmed the goodness of the method in retrieving the radiation pattern both for a broadside and a 40° tilted beam, even considering a relevant phase shifts approximation.

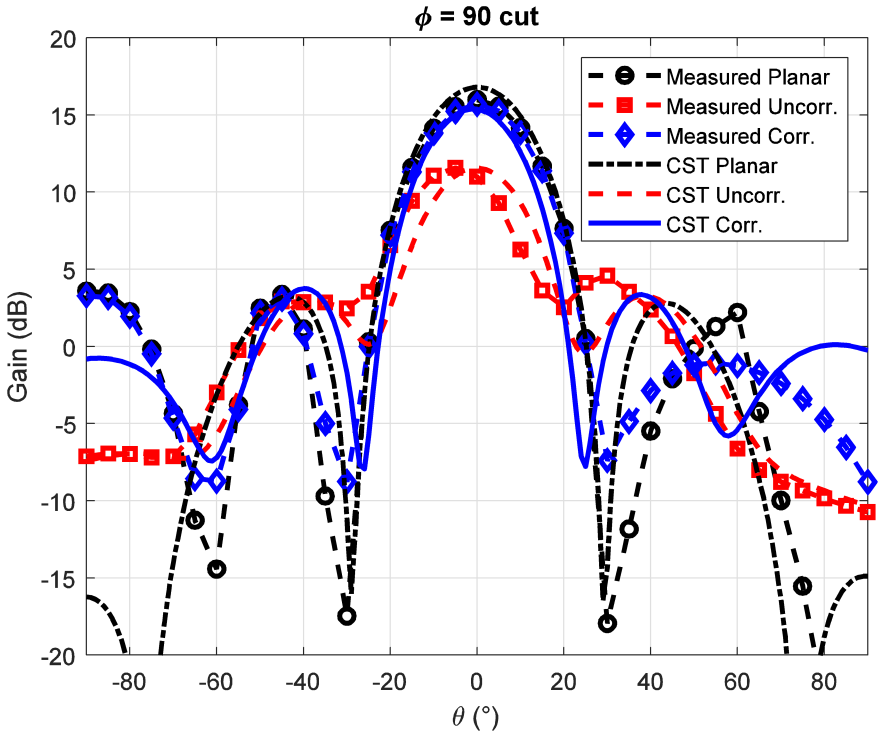

Figure 2.29: Gain pattern of the array in the xz plane.

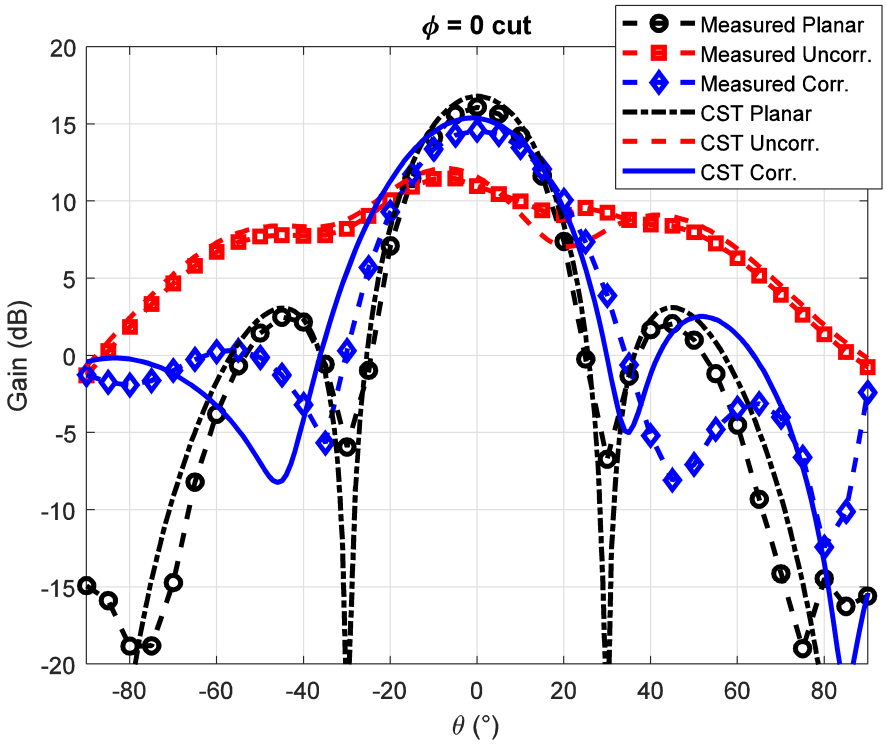

Figure 2.30: Gain pattern of the array in the yz plane.

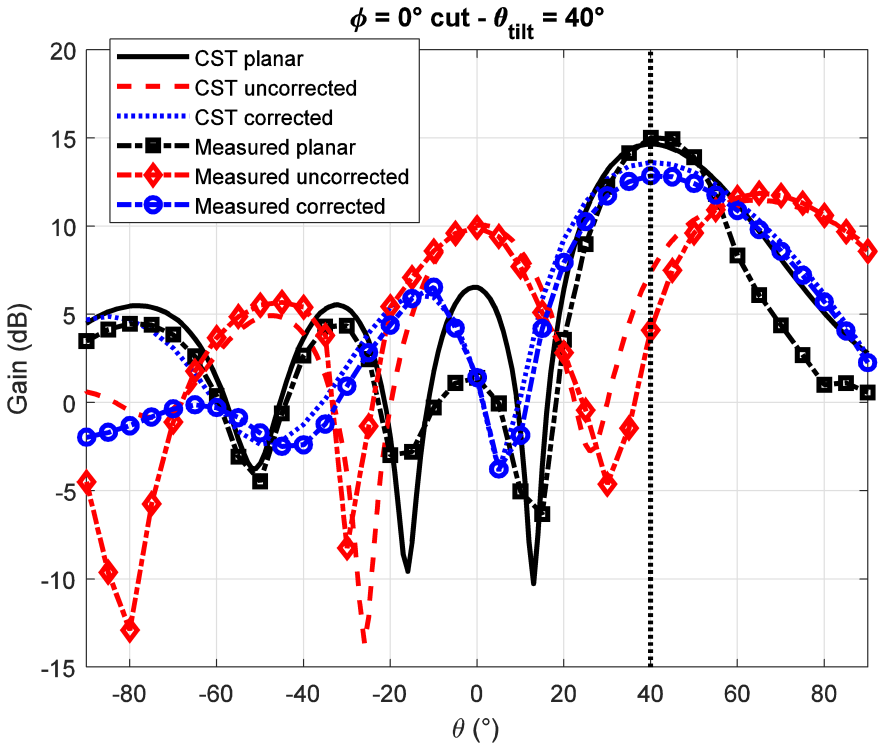

Figure 2.31: Gain pattern of the beam steering array in the yz plane.

2.8 Conclusions

At first, the effectiveness of the projection method in retrieving the radiation properties of different broadside antenna arrays has been studied. I have begun by considering linear broadside patch arrays placed on different deformed surfaces: a 1x4 wedge-shaped array, a 1x4 arc-shaped array, a 1x4 S-shaped array a 1x6 Z-shaped array.

In all these cases the projection method proved to be a good tool to retrieve the main radiation properties of the arrays. However, the effectiveness of the PM is limited to a region centered on the direction of maximum: the correcting capabilities of this method reduce for angles that are far from the broadside direction. Moreover, the higher the entity of deformation of the surface, the least the correcting capabilities of the PM far from the broadside direction.

Then the performance of the projection method were analyzed when applied to a 4x4 array placed on a strongly deformed surface: this pattern recovery technique is capable of retrieving also the radiation properties of a planar antenna, but again, its effectiveness substantially decreases further from the direction of maximum.

As a final step, the capabilities of the PM to correct the radiation properties of an antenna array that steers its beam towards different directions have been studied: a new simplified version of this pattern recovery technique for beam tilting arrays was introduced and it was proved how it is effective in retrieving the radiation properties of a 4x4 and an 8x8 doubly wedge-deformed arrays. Furthermore the sensitivity of the PM to changes of the correcting phase-shifts applied to the array elements has been investigated.

Chapter 3

Millimeter-wave Substrate Integrated Waveguide Probe for Near-Field Skin Cancer Detection

3.1 Summary

During the time I have spent as a visiting Ph.D. student at The University of Queensland (Brisbane, Australia), I have had the pleasure of working with the Microwave Group led by Professor Amin Abbosh. The group deals with the most widespread telecommunications applications, but it is particularly focused on electromagnetic imaging for biomedical applications. In particular, they have been working for several years on the design of novel skin cancer detection devices. I was given the chance of joining them in this research activity: in particular, I have worked on the design of a novel microwave device for skin cancer detection.

As it is explained below, many probes for skin cancer detection can be found in literature and nonetheless, none of them has ever been adopted in practice by clinicians as a real diagnostic aid. This is mainly because these devices are very expensive and/or they are not very practical to use and therefore, they are not competitive with visual screenings performed by dermatologists in terms of cost and time-effectiveness.

I have modeled and tested a millimeter-wave substrate integrated waveguide probe that can detect early-stage skin cancer and that, at the same time, is cheap and easy to use. Therefore this probe has the potential of becoming a widespread practical tool for skin cancer diagnosis.

3.2 Introduction

Skin cancer is among the most dangerous forms of cancer in the world: according to the Australian Bureau of Statistics (ABS), it causes more deaths than transport accidents in Australia [26] and the American Cancer Society (ACS) predicts that around 9320 people are expected to die of skin cancer in 2018 [27]. Moreover, an average of two over three australians [28] and one over five americans [29] are likely to develop skin cancer by the age of seventy. Also in Europe, skin cancer is one of the most commonly diagnosed types

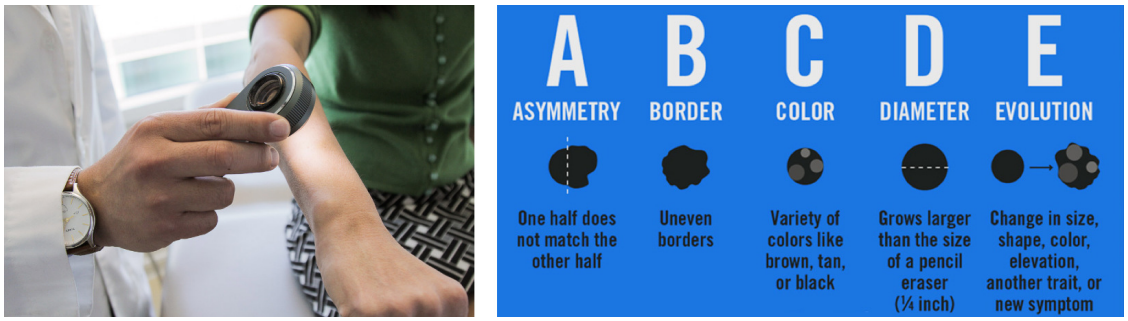

Figure 3.1: Example of visual inspection by a dermatologist with the aid of a dermatoscope to detect the presence of skin cancer (on the left) based on the ABCDE rule (explained on the right).

of tumors. For example in Italy, especially in the Northern regions, the number of newly diagnosed cases has been constantly increasing in the last decade [30].

Among the different types of skin cancers, the most common ones are basal cell carcinoma (BCC), squamous cell carcinoma (SCC) and malignant melanoma (MM). Melanoma of the skin is the third most commonly diagnosed cancer in males (after prostate and bowel cancer) and females (after breast and bowel cancer) in Australia [31]. This type of cancer is the most dangerous one since it can metastasize and therefore spread to other organs leading to death [32].

Looking at the five-years survival rates for melanomas (i.e., the probabilities that a patient survives to cancer after five years since he/she has been diagnosed with it) these strictly depend on the tumor's stage of advancement at the moment of its detection [33]. The survival rate is very low if MM is detected after it has reached distant organs (20%) or after it has reached the lymphnodes (63%), but it is considerably higher (99%) if the tumor is detected at its early-stage [33]. Therefore a prompt detection of skin cancer (and in particular of MM) at its early-stage is crucial for the survival of patients.

Nowadays, skin cancer detection is performed through visual inspection by a dermatologist with the aid of a dermatoscope as depicted in Figure 3.1. The diagnosis is based on the identification of some visual features that typically characterize melanomas and that are summarized by the ABCDE rule (Asymmetry Border Colour Diameter Evolution) schematized in Figure 3.1: there is a high probability that a mole (i.e., a nevus), or more in general a suspect skin portion, is cancerous if it is Asymmetrical (A), and/or if its Borders (B) are irregular, or its Colour (C) is uneven, or its Diameter (D) is larger than around 6mm, or if the mole Evolves (E) quickly over time. Unfortunately, this detection procedure is not very reliable: an experienced dermatologist can reach a diagnostic accuracy rate of around 80%, a senior registrar only reaches 62% and a registrar 56% [34], i.e., barely more accurate than a random guess. A correct diagnosis is particularly difficult to perform in the case of thin, early-stage melanomas, i.e., the most crucial scenario: if a melanoma is not detected at this stage there is a high chance that it will colonize other organs around the body [33] as mentioned above. The weakness of the visual inspection procedure derives from the fact that it is based on the identification of some exterior characteristics of a suspect area for which no exact discrimination threshold exist: for

example, there is no precise rule to determine whether the asymmetry level of a mole is high enough to indicate the presence of cancer.

A more objective discrimination factor between a healthy mole and a cancerous one is provided by the *water content* of the skin cells: in fact, cancerous cells have a water content that is approximately 35% higher than healthy ones [35]. This implies that the dielectric properties of cancerous tissues are quite different with respect to those of healthy tissues (as it is shown in details in Section 3.3 and in particular in Figure 3.4). This property can be used to design a device for skin cancer detection.

3.2.1 Melanoma Progression

As it was mentioned above, melanoma is the most dangerous form of skin cancer since it can metastasize and therefore spread to other organs. BCC and SCC are very rarely deadly and therefore when designing a probe for skin cancer detection, particular attention must be paid to the development process of melanomas. Understanding melanoma progression is the first step to set the requirements for a skin cancer detection probe. First of all, there are four basic types of melanomas: superficial spreading melanoma, lentigo maligna, acral lentiginous melanoma and nodular melanoma.

Superficial spreading melanoma is by far the most common type, accounting for about 70% of all cases. This is the one most often seen in young people. As the name suggests, this melanoma grows along the top layer of the skin for some time before penetrating more deeply. The first sign is the appearance of a flat or slightly raised discolored patch that has irregular borders and is somewhat asymmetrical in form. The color varies, including for example areas of tan, brown, black, red, blue or white. This type of melanoma can occur in a previously benign mole or arise as a new lesion. It can be found almost anywhere on the body but is most likely to occur on the trunk in men, the legs in women, and the upper back in both.

Lentigo maligna also remains close to the skin surface for a while, and usually appears as a flat or mildly elevated mottled tan, brown or dark brown discoloration. This type of in situ melanoma is found most often in the elderly, arising on chronically sun-exposed, damaged skin on the face, ears, arms and upper trunk. When this cancer becomes invasive, it is referred to as lentigo maligna melanoma.

Acral lentiginous melanoma also spreads superficially before penetrating more deeply. It is quite different from the others though, as it usually appears as a black or brown discoloration under the nails or on the soles of the feet or palms of the hands. This type of melanoma is sometimes found on dark-skinned people and tends to advance more often than superficial spreading melanoma and lentigo maligna because it is detected later. It is the most common melanoma in African-Americans and Asians, and the least common among Caucasians.

Nodular melanoma doesn't usually start off by spreading horizontally: in most of the cases it is invasive at the time it is first diagnosed. The malignancy is recognized when it becomes a bump. It is usually black, but occasionally it can also be blue, gray, white, brown, tan, red or skin tone. This is the most aggressive of the melanomas, and is found in 10 to 15 percent of cases.

Regardless of the melanoma type, this form of skin cancer undergoes four stages of

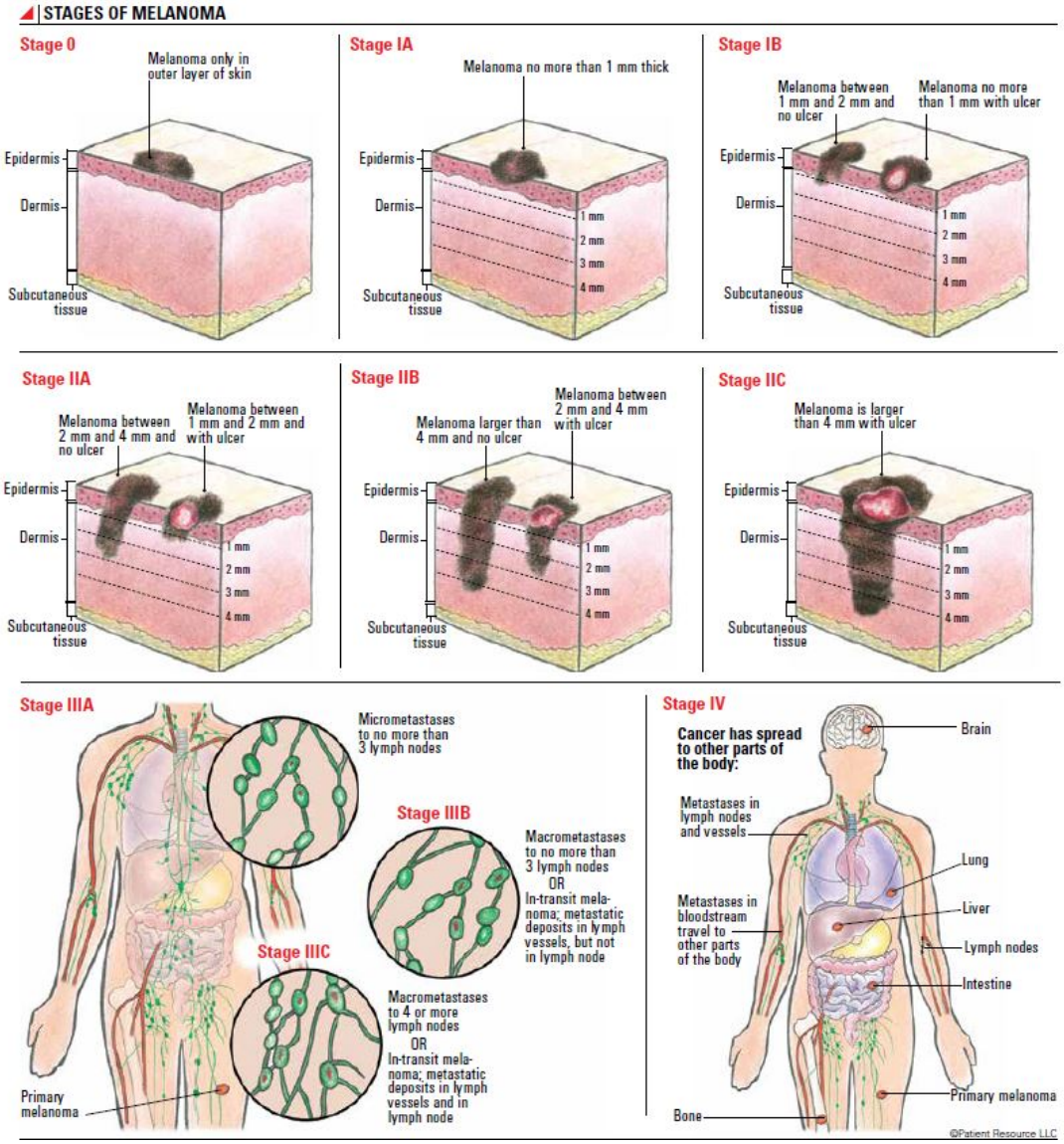

Figure 3.2: Stages of development of melanomas.

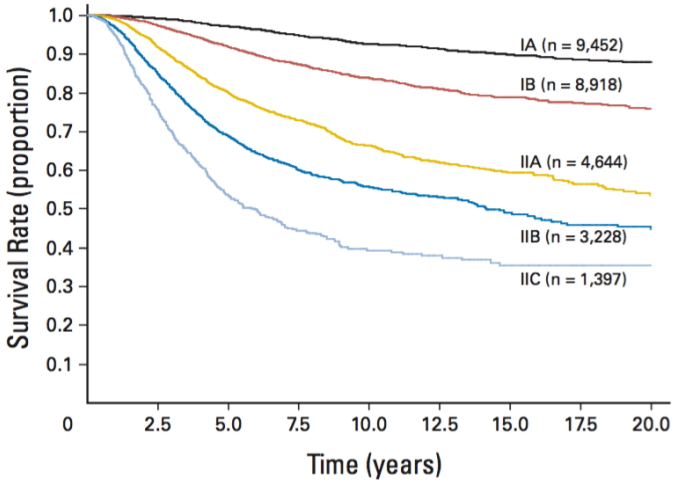

Figure 3.3: Probability of surviving to melanomas at different stages during the years after the diagnosis.

development that are marked by different features of the tumor such as its thickness, level of invasion and ulceration [36]. The characteristics of each stage are summarized in Figure 3.2 that depicts the progression of a melanoma inside the body. Melanomas originate from a group of mutated melanocites, i.e., the cells that are responsible for skin pigmentation and the formation of moles and that are placed at the bottom of the epidermis: in the vast majority of the cases these mutations carry a UV radiation signature [37]. First a melanoma infiltrates the epidermis, then it grows deeper into the dermis and finally it reaches the subcutaneous fat layer: from here it can metastasize and therefore it can colonize other organs inside the body.

Melanomas are considered to be in their early-stage of development if they are in stages 0 or I (first row of Figure 3.2). When they reach stage II (second row in Figure 3.2) they switch to be high-risk, and finally they are categorized as advanced melanomas if they are in stages III and IV (last row of Figure 3.2).

Early stage melanomas are those that are still confined into the epidermis layer or that have just started invading the dermis layer : if cancer is surgically removed at this point, the patient's probabilities of surviving are very high. The survival rate drops for high risk melanomas as it can be seen from Figure 3.3: there is a gap between survival rates of tumour at stage I and those at stage II or III. The probability of not dying of melanomas at stages III or IV are even lower, dropping below 50% after only two-years [36].

Therefore, it is crucial to detect skin cancer at its early stage, i.e., when it is still confined into the epidermis layer and it is still very thin: this implies that a device for skin cancer detection should be able to detect changes in the skin up to a $0.5\,$mm depth, i.e., at the bottom of the epidermis or at the beginning of the dermis. On the other hand, it shouldn't detect anything below the subcutaneous fat layer, otherwise other biological structures (such as for example blood vessels) could be erroneously misinterpreted as tumors.

Another factor to take into account to design a probe for skin cancer detection is that patients that are more likely to develop skin cancer are characterized by a high number of moles (> 50) and suspect regions [37]: therefore the scanning of each single suspect region must be fast.

3.2.2 Literature Review

Relative to other specialties, dermatology has been conservative towards the adoption of advanced technological diagnostic tools for multiple reasons. First of all, most skin diseases can be diagnosed by simple visual inspection and, when needed, a biopsy can be easily obtained since the skin is readily accessible. Apart from that, there are other three main reasons why the devices that have been proposed to accurately detect skin cancer have not been widely adopted by clinicians:

1. they are too expensive,
2. they are unpractical and difficult to use,
3. the screening procedure with these devices is overly time-consuming.

Among the technologies developed to detect skin cancer, some popular ones are multispectral imaging, confocal scanning laser microscopy, ultrasound imaging, magnetic resonance imaging, optical coherence tomography and molecular profiling [38].

Multispectral imaging exploits the fact that light at different wavelengths penetrates the skin at different depths: multispectral images are created by taking a sequence of images at different frequencies of light. In this way it is possible to retrieve information about the distribution of collagen, melanin content and blood vessels. Devices that exploit this technique for the detection of skin cancer, such as MelaFind [39], can achieve perfect *sensitivity* but limited *specificity*: the first parameter measures how many people that have skin cancer are correctly diagnosed with it (i.e., the higher the sensitivity the lower the number of false negative cases), the second parameter instead measures how many healthy people are actually identified as healthy people (i.e., the higher the specificity the lower the number of false positives).

Confocal scanning microscopy is capable of imaging a specific skin region by illuminating it with a light source such as a collimated and focused laser beam and analysing the backscattered light [38]. This technique can image a skin region with a good lateral resolution (between 0.5 and $1\,\mu$m) that allows to resolve inhomogeneities within a tumor. The first drawback is that in this case the penetration depth is between 200 and $300\,\mu$m: this value is high enough on average but not in a worst case scenario of a very thick skin like the one of palms and soles for which a penetration depth of at least $500\,\mu$m is needed. The second drawback is that the devices that use this technique are quite complex in terms of the optics and electronics and therefore quite expensive.

The penetration depth limitation of confocal scanning microscopy is overcome by optical coherence tomography (OCT). This interferometry technique uses a light source to achieve optical sectioning: the light source has a broad bandwidth that can enables this technique to achieve a penetration depth of $500\,\mu$m to 1 mm and an axial and lateral resolution of approximately $15\,\mu$m. Unfortunately OCT devices have the drawback of being quite expensive.

As far as ultrasound imaging is concerned, it can provide information about perfusion patterns of cancer in lymph nodes and other soft tissues (that is necessary to determine the stage of advancement of a tumor), but it cannot be used to diagnose melanomas.

Magnetic resonance imaging has also been studied as a tool for skin cancer detection, but in a similar way as ultrasound imaging, it cannot be used to diagnose melanoma: it can provide other additional information such as the thickness and volume of an already known melanoma.

Waveguides and coaxial cables have also been exploited to build probes with the aim of detecting skin cancer and abnormalities [40] [41]. In [40] an E-plane linear-tapered rectangular waveguide is built for near-field microwave imaging. The dimensions of the waveguide determine its operation frequency as well as the achievable lateral resolution and the sensitivity of the probe. As a rule of thumb, the smaller the waveguide, the higher the operating frequency and the lateral resolution, and the smaller the penetration depth. Therefore, there is a trade-off between the achievable lateral resolution of the probe and its penetration depth. In [40] a good compromise between penetration depth and lateral resolution is achieved by tapering the waveguide in order to focus the E-field on its tip. This probe is well-designed for a general imaging problem but, it presents an important limitation when applied to skin cancer diagnosis. In fact, as it can be seen from Figure 3.4, the permittivity of the skin is quite high around the operation frequency of the probe ($\epsilon_r \approx 22 + j17$ at $20\,\text{GHz}$), and therefore if the probe is used in direct contact with the skin there would be high reflections caused by the permittivity discontinuity between the air that fills the waveguide and the skin: this implicates that the probe must be used at a certain distance from the skin surface. This is a big complication because the probe is very sensitive to changes in the distance at which it is placed from the skin surface, making it unpractical in a realistic scenario where the probe is used on a real patient that wouldn't remain completely still.

The same issue is present in the design presented in [42]: a piezoelectric micro-needle antenna sensor is designed with the specific goal of detecting skin cancer. Even though the probe can effectively fulfill its goal, it cannot be used in direct contact with the skin and this complicates the detection procedure as in [40].

An interesting work has been presented in [43] about a millimeter-wave near-field probe designed for skin cancer detection. The probe is well designed but some limitations are present. First of all, it is quite expensive to fabricate and sensitive to the placement of the inner rod in the outer waveguide, with the result of being difficult to fabricate. Moreover, the tip of the probe is really small (0.6×0.5 mm^2) in order to achieve a sub-millimeter resolution to resolve inhomogeneities within a tumour but in the particular case of skin cancer diagnosis, a sub-millimeter resolution is not required. In fact the requirement for a probe is to detect the presence of skin cancer, i.e., the presence of at least a couple of hundreds of mutated melanocytes, i.e., a group of cells that is around/larger than 3 mm [44].

Therefore a sub-millimeter resolution is not indispensable, especially considering that it implies the use of a really small tip and so the scanning of the probe would take a long time. This is a problem since the fundamental requirement for a skin cancer detection device is to be easy and fast to use: in fact, the two main reasons why nowadays clinicians still rely on visual inspection is that the technology that is available is either

very expensive or takes a very long time. Considering that people that are prone to develop skin cancer have more than 50 moles [37] and that visual inspection by clinicians usually takes a couple of seconds per mole [38], it is unpractical to use a probe that require more than this amount of time to be used. Moreover a probe with a very sharp tip can break the patient's skin. In addition, the probe uses only the variations in amplitude of the reflection coefficient in order to determine whether the tissue is cancerous or not, discarding the information about the frequency variations.

Another interesting work is the one presented in [45]: the authors designed a near-field microwave microscope to detect the presence of lipomas and skin cancer. The first issue with this design is that it operates at 13 GHz, and this value is too low for skin cancer detection: at this frequency in fact the penetration depth is too high and the probe can sense the layers below the skin, e.g., in the subcutaneous fat. This could lead to a misinterpretation of the data, taking for example a blood vessel for a tumor. The authors however specify that the device dimensions can be modified to work at a different frequency. Nonetheless, there is still another major problem with this design: the microscope doesn't work in direct contact with the skin and it is sensitive to the distance at which it is placed with respect to the analysed area similarly to [40], [42].

It is possible to tune the distance between the device and the skin, but this operation needs to be performed for each scanning position in order to ensure a correct diagnosis, and this would make the whole scanning process very long.

The device presented here is a millimeter-wave substrate integrated waveguide probe designed for skin cancer detection in a practical scenario. The proposed probe is cheap and easy to fabricate, easy to use and accurate enough to be able to detect skin cancer at its early stage. It has a lateral resolution of 1 mm and a sensing depth of 0.5 mm. It is designed in order to be used in direct contact with the patient's skin and it can be easily integrated in an array so that the scanning process can be made even faster.

3.3 Skin Model and Phantom

As it has been addressed in the introduction, skin cancer has a water content that is approximately 35% higher than that of healthy skin [35], and therefore the dielectric properties of healthy and cancerous tissues are different as depicted in Figure 3.4. This fact can be exploited to build a probe that can detect the presence of cancer by revealing a change in the permittivity of the skin: this difference eventually manifests in the form of a variation of the reflection coefficient detected by the probe. In order to present the design of the proposed device, it is useful to get some insights about the skin and cancer dielectric properties.

The skin comprises three main layers that are, from the outermost to the deepest one, the stratum corneum (SC), the epidermis (E) and the dermis (D), as it's depicted in Figure 3.5. The thicknesses of these layers (and therefore the thickness of the overall skin layer) vary from person to person and it changes with respect to the body region [46]:

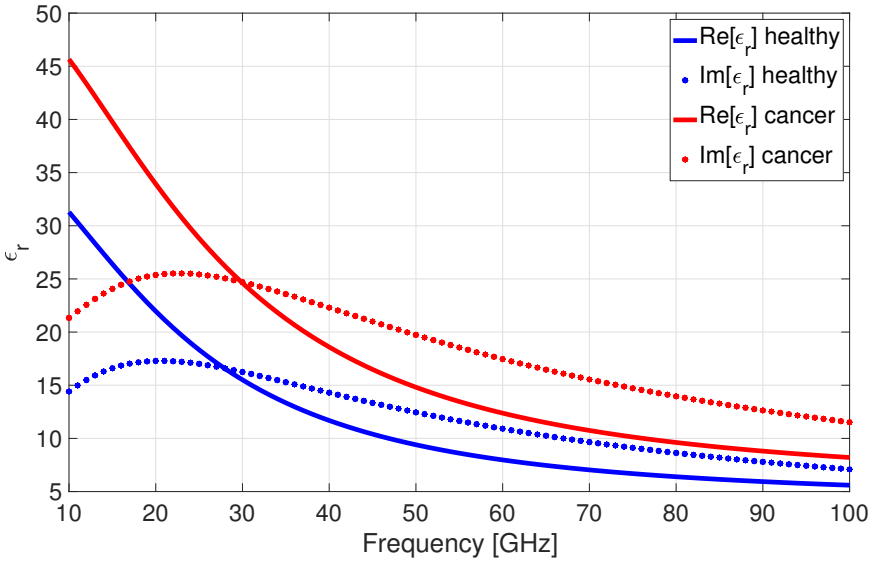

Figure 3.4: Relative permittivity of healthy (blue) and cancerous (red) skin: real (solid lines) and imaginary (dashed lines) parts of ϵ_r.

for example, the thinnest skin can be found on the forearm (around 0.5 mm) while the thickest one can be found on the soles and palms (around 2 mm) [46]. The dielectric properties of the skin also vary from individual to individual and depend from the body region and the skin type (e.g., dry skin, moisturized skin, etc.).

The frequency-dependent complex permittivity of healthy and cancerous skin tissues are usually modeled either by a Cole–Cole or by a Debye function: Gabriel [47], Hwuang [48] and Chahat [49] relied on the former model, while Gandhi [50], Aminzadeh [51] and Alekseev [52] used the second one.

According to Chahat [49], the complex dielectric permittivity $\epsilon_r = \epsilon' + j\epsilon''$ of the skin can be described through a Cole-Cole function:

$$\epsilon_r = \epsilon_\infty + \frac{\Delta\epsilon}{1 + (j\omega\tau)^{1-\alpha}} + \frac{\sigma_s}{j\omega\epsilon_0} \tag{3.1}$$

where ϵ_∞ is the optical permittivity, τ the relaxation time, $\Delta\epsilon = \epsilon_s - \epsilon_\infty$ the magnitude of the dispersion of the fraction of free water in the skin, and ϵ_s the static permittivity; α characterizes the spread in relaxation time, and σ_s is the ionic conductivity. To determine the model parameters over a broad frequency band, optimization has been carried out using an in-house binary genetic algorithm, that lead to the optimized values reported in Table 3.1.

In Aminzadeh [51] a single relaxation Debye model has been used to express the frequency dependency of the complex permittivity of each tissue:

$$\epsilon_r = \epsilon_\infty + \frac{A_p(\epsilon_s - \epsilon_\infty)}{1 + j\omega\tau_p} + \frac{\sigma_s}{j\omega\epsilon_0} \tag{3.2}$$

where the parameters are the same as in Equation 3.1 except for A_p that is defined as the pole amplitude. A genetic algorithm was used to fit and optimize the Debye parameters to the estimated dielectric data, obtaining the values reported in Table 3.2.

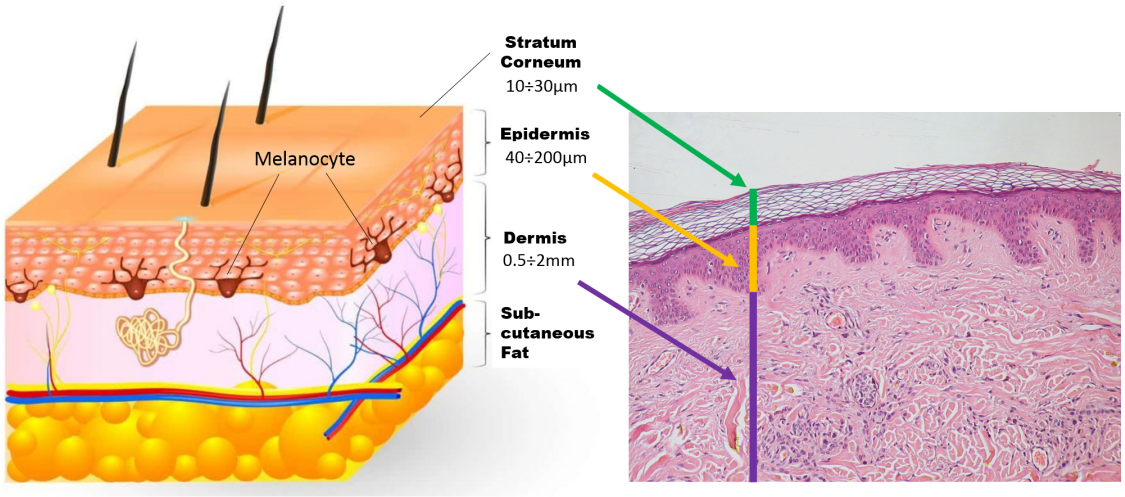

Figure 3.5: Structure of the skin. The drawing on the left depicts the three main skin layers and the interval values (min÷max) of their thicknesses as taken from [1] [2] [3]. The picture on the right is the cross section of a skin portion gathered from a microscope (Source: Wikipedia *Dermis* page).

The two approaches lead to very similar values of frequency-dependent tissues permittivity as it can be seen from the high level of similarity between Equations 3.1 and 3.2. In this work, the dielectric properties of the skin, fat and muscle layers have been taken from the IT'IS Database for thermal and electromagnetic parameters of biological tissues [53]: this database is available on-line and it comprises the dielectric properties from 10 Hz to 100 GHz of numerous body tissues based on Gabriel's dispersion relationship [54].

Considering the skin, this has been modeled as a single layer with dielectric properties that are the average between those of epidermis and dermis, since these two layers have very similar water contents [2] [51]. The stratum corneum has been neglected as it has been done in the vast majority of works reported in [2]: it is made by $10 \div 30$ layers of dead keratynocites and therefore it is very thin ($10 \div 15$ μm).

As far as skin cancer permittivity is concerned, this has been modeled in the same way as in [51], i.e., according to a Debye model with the parameters reported in Table 3.2 for the tumor tissue.

Even if when simulating the interaction with electromagnetic waves, the skin is well

Tissue	ϵ_∞	$\Delta\epsilon$	α	τ_p [ps]	σ_s [S/m]
Skin	8.35	20.5	0.064	7.13	0.5

Table 3.1: Optimized parameters for the Cole–Cole model as reported in [49].

Tissue	ϵ_∞	ϵ_s	A_p	τ_p [ps]	σ_s [S/m]
SC	3.24	4.96	1.074	2.14	0.07
E-D	5	36.55	0.946	6.07	2.60
Tumor	5.45	56.79	0.908	6.35	2.94

Table 3.2: Optimized parameters for the Debye model as reported in [51].

approximated by a semi-infinite homogeneous layer (with the dielectric properties of the epidermis and dermis) [52], a more accurate electromagnetic model comprising the skin, the sub-cutaneous fat and the muscle layers has been adopted in this work to run full-wave numerical simulations in CST. The subcutaneous fat layer and the muscle layer dielectric properties have been set according to [53] and they are reported in Figure 3.6.

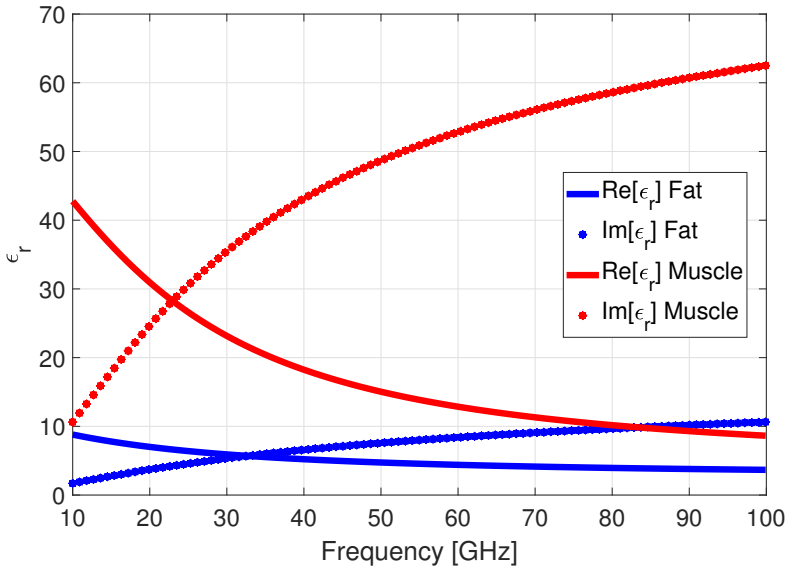

Figure 3.6: Relative permittivity of fat (blue) and muscle (red) tissues: real (solid lines) and imaginary (dashed lines) parts of ϵ_r.

3.3.1 Skin Phantom

In practice, in order to test the fabricated probe, two phantoms were realized: one consisting only on skin-mimicking material and one made by three layers, i.e., skin, fat and muscle. All the tissues recipes are based on corn flour and gelatine. The advantage of realizing a corn flour based skin phantom is that this turns out to be very elastic, like the skin, so a cancer sample can be easily placed both inside the skin or on its surface simply by creating a small whole with a tweezer in the first case, or just scratching the skin surface a bit and then slightly but firmly pushing the cancer sample on the top of the skin. Moreover, since the material is elastic (as the skin), the probe can be easily placed on the surface without any risk of damaging the probe tip because of a solid and rigid skin phantom like the one proposed in [43].

On the other hand, this type of phantom has two main disadvantages. The first one is that it is very hard to measure the probe lateral resolution since, in order to do this, a very small cancer sample (less then 0.5 mm) is needed: this is almost impossible to realize, since the drops of cancer material cannot be made smaller than 1 mm. The other drawback is that the water evaporates quickly from the phantom and therefore the measurements must be taken within a couple of days from the phantom realization, otherwise its dielectric properties change.

In the end, the single layer phantom provided a more reliable solution to test the probe as it will be described in the results section: this is because it is very difficult to

build a three-layers skin phantom with such small thicknesses (especially the skin one). Moreover, the skin layer (i.e., the thinnest) dries very fast and this limits the amount of available time to perform the measurements. As a final remark, a three-layer phantom is not actually required since the sensing depth of the probe at millimeter-wave is limited to the skin layer and therefore it cannot sense anything deeper than this layer as it will be shown in the followings: this is the reason why in the vast majority of the works that can be found in literature, the skin is modeled as a semi-infinite homogeneous layer as it was stressed above [2].

Single-Layer Phantom

In order to realize the single layer phantom that mimic healthy skin, 15.3 g of propylene glycol is mixed with 300 ml of deionized water and then 10 g of gelatine is slowly added while stirring. The mixture is gradually heated to $90°$ C and then it is left to partially cool down. In a separate bowl 100 ml of water is mixed with 80 g of corn flour and added to the gelatine mixture while stirring. Finally, when the mixture cools down to $40°$ C, it is poured in a mould.

The procedure to realize the tumor tissue is similar: 30 g of agar are mixed with 335 ml of deionized water while stirring and the compost is heated up to $90°$ C so that gelatine can be formed. Then the mixture is let to cool down to $40°$ C and at this point 30.4 ml of sunflower oil are mixed with 2.7 ml of dish-washing liquid in order to form an emulsion. The quantities of the different ingredients are reported in Table 3.3. The resulting cancer material solidifies very quickly, and therefore in order to insert it inside the skin phantom, first the healthy skin phantom was created, and then, after this had set, the cancer material was made and with the aid of a metallic pointy tip a few drops were let to rest on a sheet of baking paper. Finally they were then inserted inside the skin phantom with a tweezer. The resulting single layer phantom is depicted in Figure 3.8.

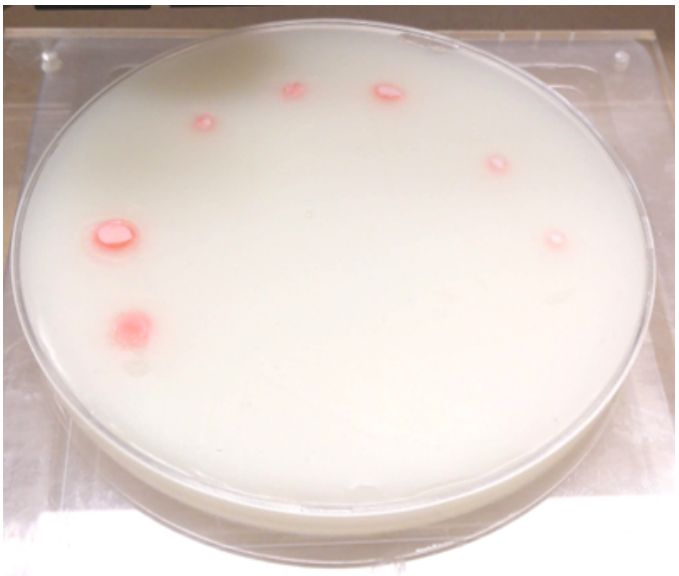

Figure 3.7: Single layer phantom comprising skin-mimicking (white) and cancer (red-ish) material.

Three-Layers Phantom

As far as the three layers phantom is concerned, the skin and cancer materials are realized according to the same procedure presented above.

The fat layer has been realized by mixing 23.4 g of propylene glycol with 200 mL de-ionized water and 35.5 g of gelatine is added slowly while stirring. The mixture is heated gradually to 90° C and then allowed to partially cool. In a separate bowl, 150 mL of grape seed oil is heated to 50° C and added to the partially cooled gelatine mixture. The final mixture is cooled to 40° C. Then 5.2 ml of commercial dish-washing liquid acting as a surfactant is added to form an oil emulsion before being poured into the mould.

To realize the muscle layer, the same procedure as for the tumor is followed just using different materials quantities as it is indicated in the Table 3.3. The resulting three layers phantom is depicted in Figure 3.8.

3.4 Probe Requirements

As it has been stressed above, the skin properties (thickness, humidity and permittivity) change with respect to the person and body part that is considered. Therefore, in order to design a probe that is capable of universally detecting the presence of cancer in every individual and in every part of the body, the probe should operate according to a *differential approach*: it must be able to detect *relative changes* in the dielectric properties of a suspect area with respect to its healthy surroundings (rather than differences with respect to an absolute value taken as a reference for healthy skin).

Moreover, the probe should provide a practical and accurate aid for clinicians to diagnose skin cancer and in particular melanomas. In order to do so, the probe must meet the following requirements.

First of all, the device needs to be practical to use and this means that the probe must work in direct contact with the skin. If this weren't the case, then the probe would be sensitive to the distance from the patient's skin (as the one designed in [45]) and therefore a check and/or and adjustment of its positioning would be required at every scanning step resulting in a highly time-consuming procedure.

Secondly, the probe must be able to detect changes in the dielectric properties of the skin at the bottom of the epidermis and at the same time, it must avoid sensing changes in the permittivity of tissues that are below the subcutaneous fat layer. The reason of this

Material	Healthy skin	Muscle	Fat	Tumor
Water (ml)	400	430	200	335
Corn flour (g)	50	0	0	0
Gelatin (g)	10	114	35.55	0
Agar (g)	0	0	0	30
Propylene glycol (g)	15.3	4.6	23.4	5.4
Grape seed oil	0	25.3	150	30.4
Dishwashing liquid	0	2.3	5.2	2.7

Table 3.3: Ingredients quantities to realize the single-layer and multi-layers phantom.

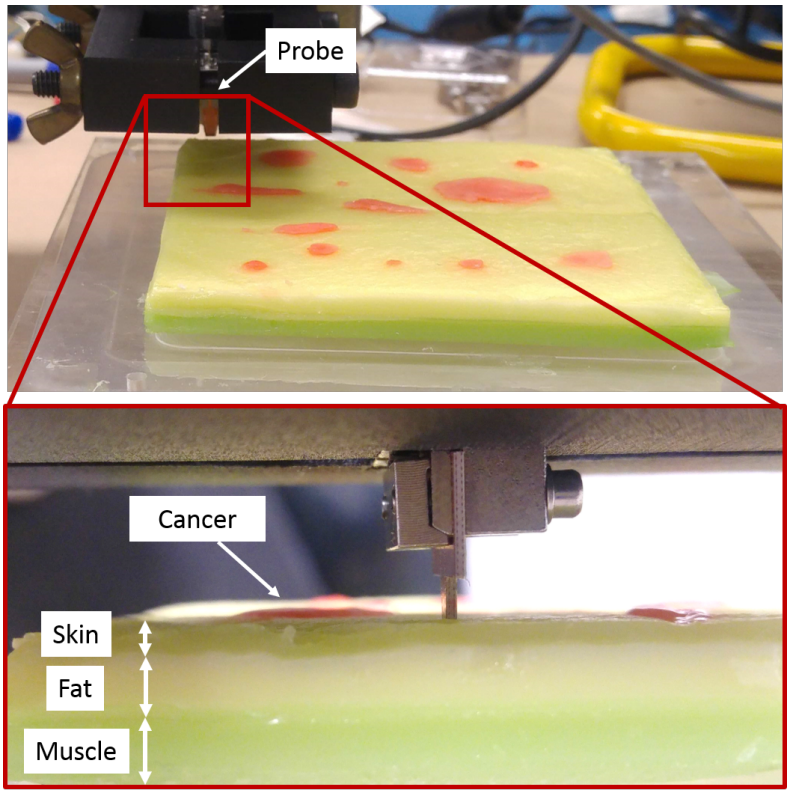

Figure 3.8: Three layers phantom comprising skin (white), fat (yellow), muscle (green) and cancer (red-ish) material.

design choice can be explained considering the development of melanomas as described in Section 3.2.1: this cancer originates from a group of mutated melanocytes, i.e., cells that are placed at the bottom of the epidermis (see Figure 3.5). Melanomas then invade the dermis growing deeper until they reach the subcutaneous fat layer. At this point, since this layer is vascularized, cancerous cells can metastasize and therefore spread around the body and reach other organs, dramatically increasing the patient's death risk.

This means that in order to detect melanomas on time, the correct diagnosis must be done when cancer is still confined in the dermis layer. This is why the probe must be able to detect changes in the dielectric properties of the skin between its surface and the bottom of the dermis layer. At the same time it shouldn't sense targets that are buried deep in the fat layer or other underlying layers: in fact, if the target is a melanoma, then it is present also in the epidermis and the dermis and it can be detected by sensing its presence in these two layers. On the other hand, if the probe can sense changes in permittivity deep in the fat layer, then it could detect the presence of another biological entity (such as a blood vessel), erroneously leading to a false-positive detection of cancer.

In order to translate this sensing depth requirement into a number, one more consideration must be taken into account: the thickness of the skin is highly variable around the body. For this reason, two scenarios have been considered in order to set a numerical value for the required sensing depth of the probe: the minimum skin thickness and the maximum one.

Since cancer begins to grow at the bottom of the epidermis and therefore, when the skin thickness is maximum, the probe must be able to detect its presence deeper in the skin

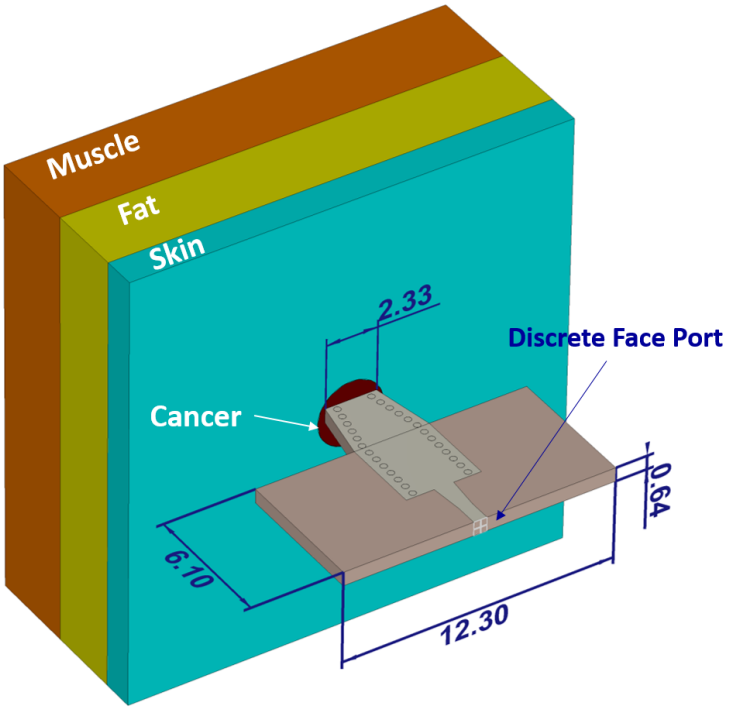

Figure 3.9: Design of the probe as it has been simulated in CST with main dimensions indicated (mm): the device in direct contact with the three-layers skin model.

with respect to the thin skin case. This means that the thickest skin scenario represents a *lower bound* on the sensing depth of the probe: the probe must detect changes in the skin permittivity at a depth that is *at least* the maximum thickness value of the epidermis, i.e., $200\,\mu$m [46].

On the other hand, when the skin thickness is minimum, the underlying layers are closer to the skin surface, and therefore to the probe: this sets an *upper bound* to the sensing depth. Therefore, since in this case the probe must avoid to detect biological entities that are buried deep in the subcutaneous fat layer, its sensing depth must not be greater than the minimum skin thickness (epidermis + dermis), i.e., 0.5 mm.

The final requirement is about the lateral resolution of the probe. An early-stage melanoma is very rarely smaller than 2 mm [44] but, in order to be absolutely sure that the probe works in all possible cases, the requirement for it has been set to have a lateral resolution of 1 mm.

The requirements on the sensing depth and on the lateral resolution are needed to set the operation frequency of the probe. In fact there is always a trade-off between the achievable sensing depth and lateral resolution of the probe: the higher the frequency, the smaller the wavelength and so the higher the lateral resolution and the lower the sensing depth; on the other hand, the lower the frequency, the bigger the wavelength and so the lower the lateral resolution and the higher the sensing depth.

As it will be shown below, a good frequency band is the one between 35 and 45 GHz. The band is quite wide, and this is dictated by another requirement, i.e., the device must be able to operate on every type of skin: in fact, since the skin dielectric properties vary between person to person and with respect to the hydration and moisturizing level, a

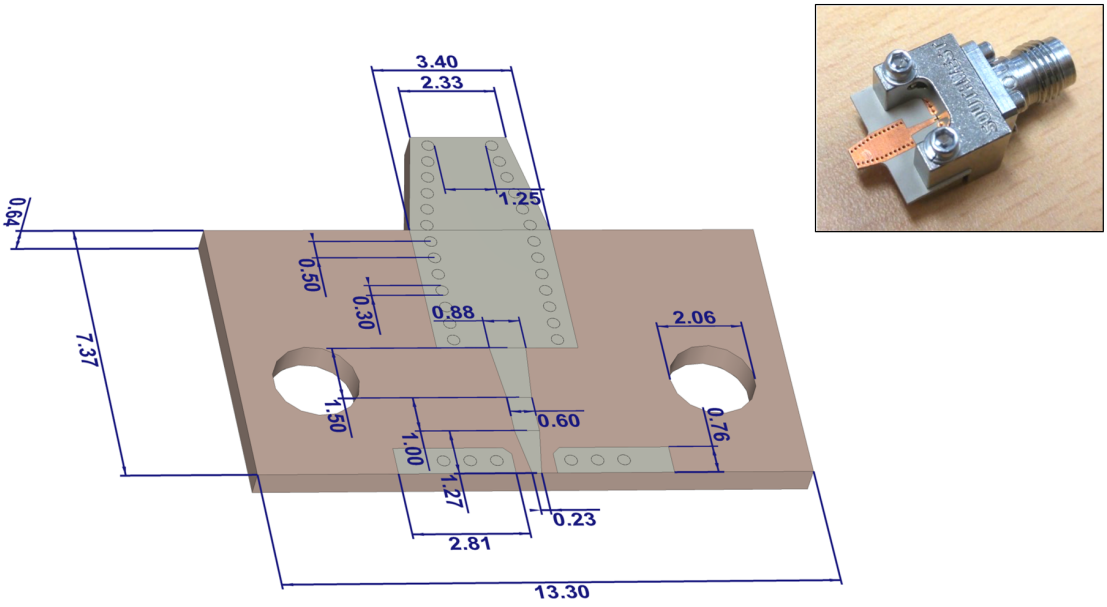

Figure 3.10: CAD model of the fabricated probe prototype with all the dimensions (mm) and picture of the device attached to the high-frequency end-launch connector that has been used to take the measurements.

wide frequency band ensures that no cases are left out.

3.5 Probe Design

A substrate integrated waveguide (SIW) probe is proposed in order to fulfill the requirements described in the previous section. The design of the probe as it has been simulated in CST is presented in Figure 3.9 together with its main dimensions. The probe is based on a tapered SIW that makes the device cheap and easy-to-fabricate. The pitch, i.e., the distance between adjacent vias, has been set to 0.5 mm, and the vias diameter is 0.3 mm that is perfectly compatible with what is available on the market.

The SIW is realized on a 0.64 mm thick Rogers RO2310 panel: this high dielectric constant material ($\mathrm{Re}[\epsilon_r] = 10.2$) allows the probe to work in direct contact with the skin in the frequency band of interest (thanks to a good matching between the two materials). This wouldn't be the case if a low permittivity material were used as the substrate, nor if a standard metallic waveguide (filled with air) were adopted. The probe is fed through a microstrip line that is tapered at the end to provide a good transition between the microstrip and the waveguide.

The probe tip is tapered as well: this increases the electric field along the probe and it focuses it on a small region (correspondent to the tip's face) on the skin surface. In Figure 3.13 the decrease of the E-field inside the skin is reported. As it can be seen, the penetration depth of the probe is 0.4 mm: this value simply indicates at which depth the electric field decreases of $1/e$ with respect to the maximum value, i.e., the one on the skin surface. The penetration depth *is not* the same as the *sensing depth*: the latter is defined as the maximum depth at which the probe can sense changes in the dielectric properties of the skin (as it will be explained in the results section).

The probe dimensions such as tapering angle of the tip, pitch between vias and SIW width have been tuned in two rounds of CST Microwave Studio simulations. First the probe dimensions were optimized when the device is in direct contact with the skin to provide a good match between the two. Then, after this first optimization round, a few different probe models with comparable matching performance were selected and further simulations were run including cancer into the skin in order to determine the best prototype, i.e., the one that is more sensitive to the presence of cancer in terms of reflection coefficient's change.

The probe was then fabricated and a 2.40 mm high frequency end launch connector from Southwest Microwave (model number: 1492-04A-5) was attached to it as it can be seen from Figure 3.10. It can be noticed that the CAD model of the final prototype is slightly different with respect to the one that was simulated in CST (Figure 3.9): an additional tapered microstrip line is added at the very beginning of the microstrip line that feeds the probe in Figure 3.9 together with two metallic patches with vias placed on either sides of the tapered line. This adjustment was required in order to use the end-launch connector. In fact, the inner part of the connector's coaxial cable is attached to the probe through a very thin pin, while the outer part of the coaxial cable touches the two patches at the sides of the tapered microstrip line: therefore, if the microstrip line is not narrow enough, there is a chance that both the inner pin and the outer part of the coaxial cable touch the microstrip line, causing a short circuit. Moreover two holes have been drilled in the substrate in order to screw the connector to the probe.

3.6 Results and Discussion

The probe has been tested both through full-wave numerical simulations in CST Microwave Studio and through measurements on the phantom realized as it was described in Section 3.3.1. The simulations have been useful both to develop the initial design of the probe and to determine some of the properties of the device. In fact, due to the limitations that have been pointed out in Section 3.3.1, it is quite complicate to determine the penetration depth and lateral resolution of the probe since it is difficult to realize a cancer target of specific and arbitrary small dimensions (diameter and height) and to accurately place it at a specific depth inside the skin phantom.

3.6.1 Preliminary Simulative Results

As a first step, a preliminary model of the probe was designed in CST and tested in order to prove its effectiveness in detecting a very small early-stage tumor. From Figure 3.11 it can be noticed how this prototype is slightly different from the one reported in Figure 3.9: the substrate width is smaller, the SIW is shorter, the tip is slightly wider (because the vias diameter is slightly larger, i.e., 0.5 mm).

Since the epidermis and dermis thicknesses strongly vary along the body, two different skin models were considered: a very thin layer of skin of 0.49 mm corresponding to the forearm, and a thick layer of 1.02 mm corresponding to the soles. The first represents the worst case scenario as far as the electric field penetration in the underlying tissues is concerned, the second one is the case in which it is more difficult to detect the presence

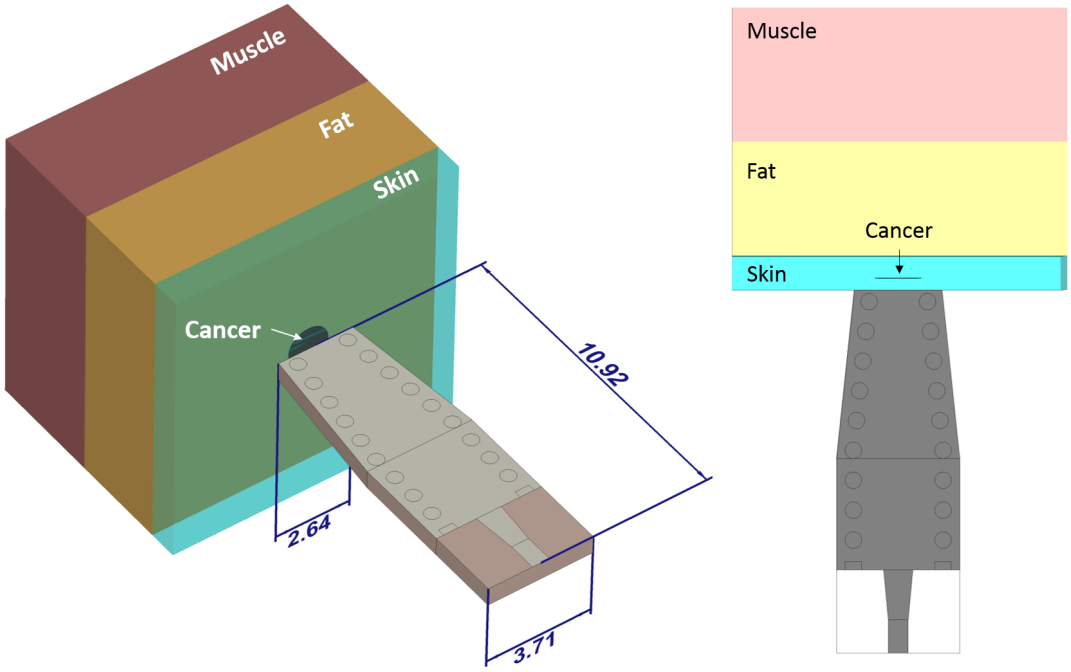

Figure 3.11: Preliminary design of the probe as it has been simulated in CST: the main differences with respect to the dimensions of Figure 3.9 are indicated (in mm): in this model the cancer target is buried inside the skin in correspondence of the bottom of the epidermis.

of cancer at the bottom of the epidermis since this is very thick. The probe is designed to work in both cases.

As far as the skin model is concerned, the subcutaneous fat layer and the muscle layers are 3.4 and 4 mm thick respectively. Skin cancer is modeled as a very thin disk (height equal to 20μm and varying diameter between 0.2 and 1.4 mm) placed inside the skin at a depth that corresponds to the bottom of the epidermis: 40μm in the thin skin case and 0.37mm in the thick skin case. This is a very good approximation of an early-stage melanoma in accordance to what was said in Section 3.3.

The performance of this probe have been published in [55]. Figure 3.12 reports the absolute value of the reflection coefficient seen by the probe when this is fed through a 50Ω discrete face port and it's facing healthy or diseased skin. The probe operates according to a differential approach: given a suspect region, the device first measures $|S_{11}|$ in correspondence of a portion of surrounding healthy skin, then it measures $|S_{11}|$ in correspondence of the potentially cancerous area and finally it compares the two measurements looking for relevant differences between the two. In particular, we are looking for changes in the frequency position and amplitude of the peaks of $|S_{11}|$: three such peaks can be seen from Figure 3.12 at around 41, 44.5, and 48 GHz. The three minima of $|S_{11}|$ shift of around 100 MHz when the probe is facing skin with a cancer target buried in it (the reference $|S_{11}|$ being the case in which the probe is facing only healthy skin). Therefore the probe operates in a wide frequency band that goes from 40 to 50 GHz that ensures that all skin types can be analyzed by the probe independently

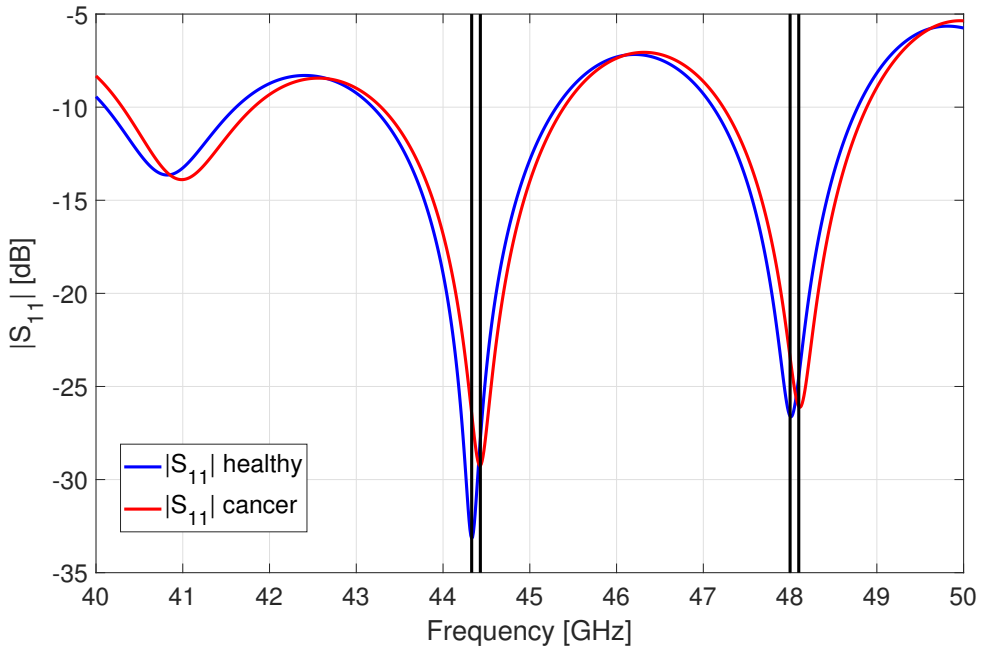

Figure 3.12: Absolute value of the reflection coefficient seen by the probe designed in CST as in Figure 3.11 when placed on thin healthy skin (blue) and when a cancer disk of height 20μm and diameter 0.8 mm is present at a depth of 40μm (red).

of the skin hydration level and of the changes in dielectric properties depending on the individual and on the body sites: the three peaks will slightly shift in frequency but there will always be one within the frequency range of interest.

From simulations, the best performance have been obtained in this case in correspondence of the third peak of $|S_{11}|$ in Figure 3.12, i.e., the one around 48 GHz: this means that in correspondence of this peak the largest difference between healthy and cancerous skin is observed. From Figure 3.13 it can be noticed that at this frequency the penetration depth is 0.4 mm that is enough for the electric field to penetrate at the bottom of the epidermis even in body sites in which this is thick; at the same time the field is almost null at the end of the subcutaneous fat, thus preventing undesired radiation into underlying tissues when thin skin is analyzed.

The tapered tip allows to increase the electric field at the end of the probe, i.e., on the skin's surface and to focus it in a small region correspondent to the probe tip face on the skin surface as it can be seen from Figures 3.14, 3.15. It is worth mentioning that the input power in CST is quite high $(0.5\,\text{W})$, but the main purpose of the pictures is to give an idea of the general behavior of the electric field inside the probe and the skin.

The results for thin and thick skin models and varying cancer diameters are reported in Figure 3.16. Thin skin represents the best case scenario for tumor detection, since cancer is closer to the probe: a frequency shift of 100 MHz (indicated by black vertical lines) can be observed in the $|S_{11}|$ peak in the case of the smallest cancer diameter $(0.2\,\text{mm})$ with respect to the healthy tissue. And for larger cancer sizes the shift is even slightly higher. When the epidermis and dermis are thicker instead, the minimum detectable frequency shift is lower, i.e., 70 MHz for the smallest tumor diameter (slightly higher for

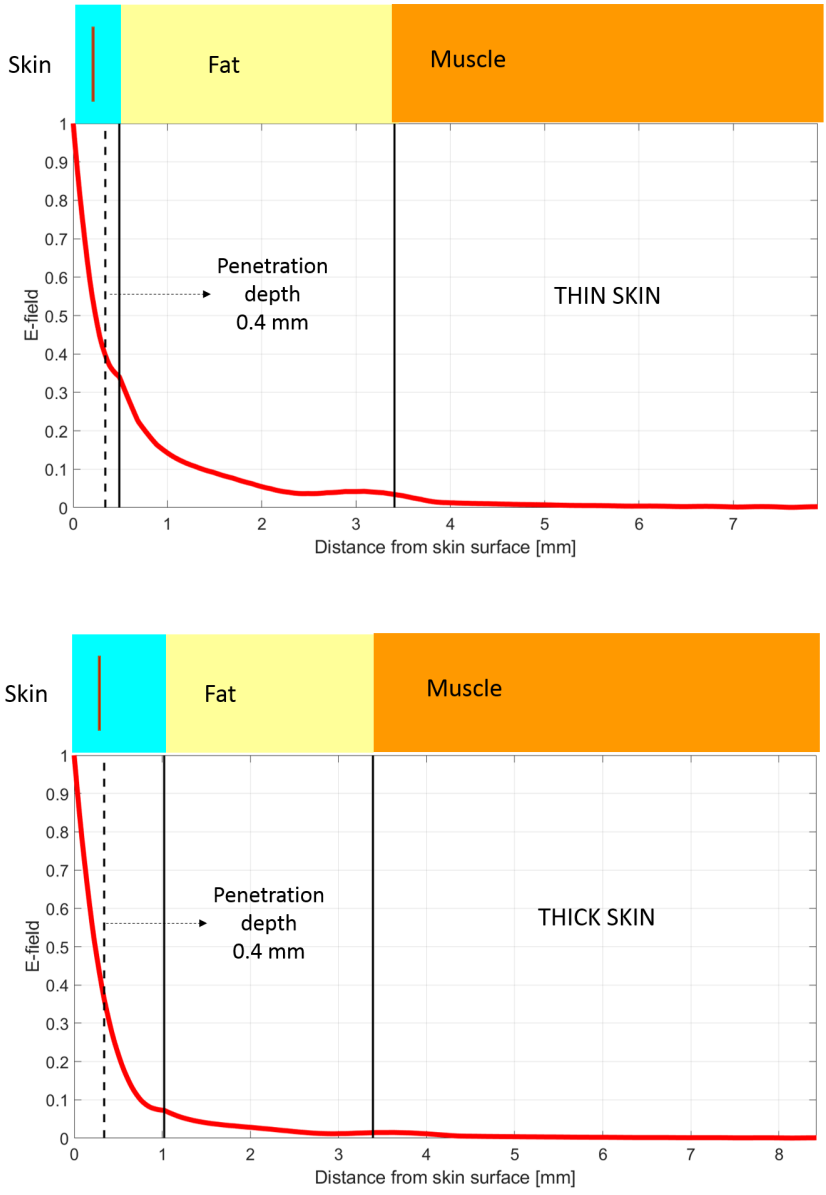

Figure 3.13: Relative decrease of the E-field inside the skin and underlying layers: as it can be seen the E-field decreases very quickly, being almost negligible after the skin layer.

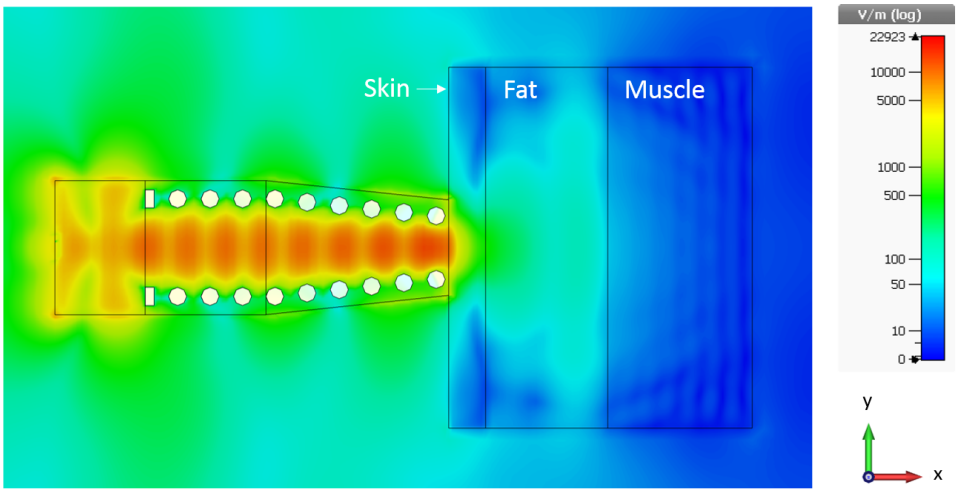

Figure 3.14: CST simulated electric field (RMS value [V/m]) along the probe and inside the skin for an input power of 0.5 W: the field increases towards the tip due to the tapering and then rapidly decreases inside the skin.

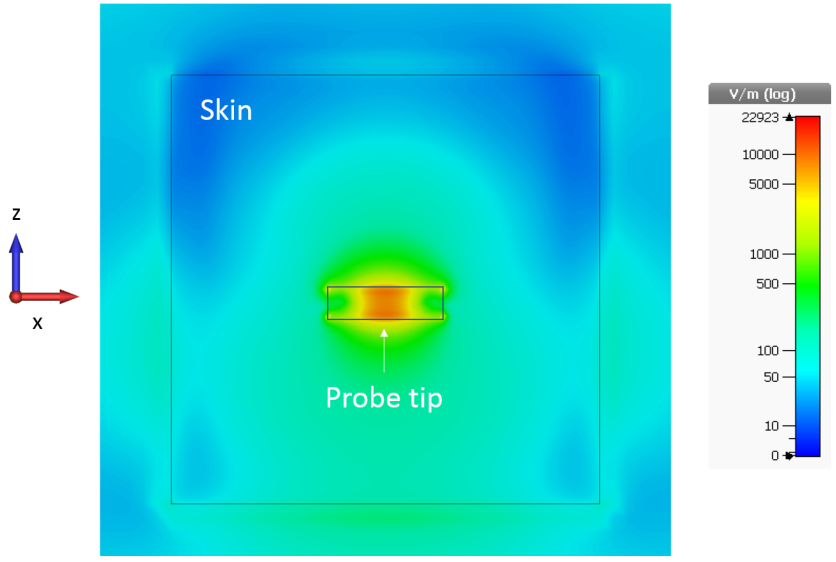

Figure 3.15: CST simulated electric field (RMS value [V/m]) on the outer skin surface that is in direct contact with the probe for an input power of 0.5 W: the field is focused on a narrow area corresponding to the probe's tip.

larger sizes), since cancer is further from the probe in this case. However, even if the shift is smaller, it is still clearly detectable.

3.6.2 Measurements Results

Since the probe described in the above section proved to be effective in simulations, its design has been slightly modified in order to fabricate it. The final design is the one presented in Section 3.4 and depicted in Figure 3.9 and this is different with respect to the one just described above and depicted in Figure 3.11 with respect to the following aspects: the vias diameter was reduced to 0.3 mm, i.e., the smallest value achievable by the manufacturer, and as a consequence also the probe tip was reduced; the substrate was enlarged in order to be wide enough to host the screws through which the high-frequency end-launch is fixed to the board, and for the same reason two holes were drilled in the substrate in correspondence of the screws position. Despite these differences, the main features of the probe don't change: as it can be seen from Figures 3.17-3.18, once again the electric field increases on the probe tip thanks to the tapered design and it's confined on a small region in correspondence of the probe tip face on the skin surface. It is worth mentioning again that the input power in CST is quite high, i.e., 0.5 W, but the main purpose of the pictures is to give a general idea of the behavior of the electric field inside the probe and the skin. In practice, the measurements that are presented here have been obtained with an input power of 1 mW.

As far as the measurements are concerned, the experimental set-up is depicted in Figure 4.19: the end-launch connector to which the probe is attached is connected through a high-frequency cable to a VNA (Field Fox) that works up to 50 GHz. The probe is fixed to a CNC machine thanks to an ad-hoc support that was designed to keep it in position and prevent it to rotate during the scanning process. The skin phantom is placed under the probe and then the CNC machine is activated to determine at which height the probe must be positioned in order to get the measurements. Once the probe is in direct contact with the surface of the skin phantom, no significant differences are detected with respect to the pressure of the probe on the phantom. The probe height has been set in such a way that it resembles the pressure that would be applied on a human being in a realistic scenario: a pressure for which the probe is firmly placed on the skin that is bent a little bit, as it is shown in Figure 4.19. At this point the acquisition of the data begins: the probe is scanned on a 2D grid with a step of 1 mm in both direction. In order not to damage the skin phantom, the probe is lifted after taking each measurement, i.e., it is lifted before it is shifted so that it doesn't scratch the phantom.

For each position of the probe on the scanning grid, the reflection coefficient is recorded three times: this has been done to determine whether there were significant changes between subsequent measurements. Figure 3.20 reports an example of a recorded measurement in correspondence of healthy skin (i.e., the phantom depicted in Figure 3.7). After the scanning is completed, the collected data is analyzed according to the following procedure. Since the data are quite noisy, as a first thing a Gaussian-shaped moving average filter is used to clean out the data from the noise. The window size of the filter has been set to 20: this value is high enough to effectively remove the noise, and at the same time is low enough not to compromise the information contained in the data. The main

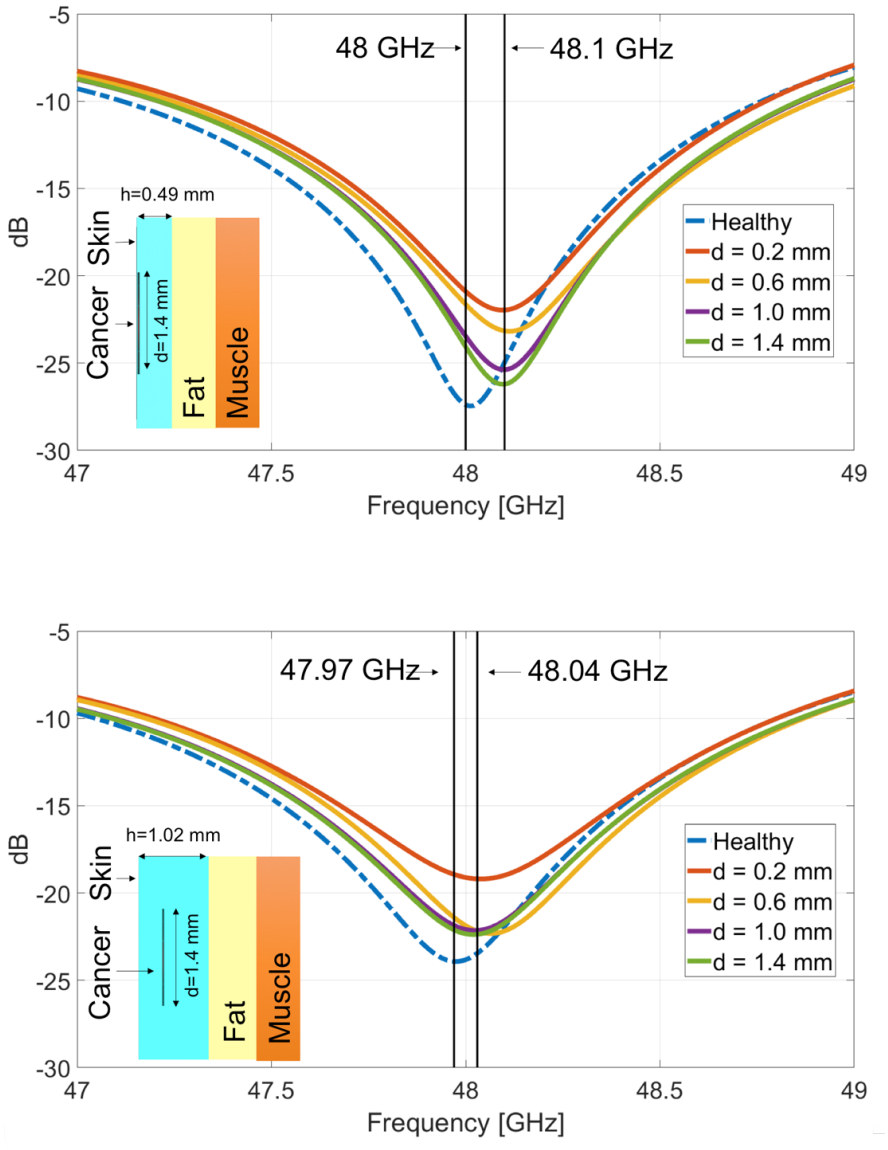

Figure 3.16: $|S_{11}|$ for thin (top figure) and thick (bottom figure) skin of height 0.49 and 1.02 mm respectively. Cancer is placed at a depth of 40μm and 0.37 mm in the skin and its diameter varies from $d = 0.2$ to $d = 1.4$ mm. Vertical lines indicate the minimum detectable frequency shift in the peak position (inset figures not drawn to scale).

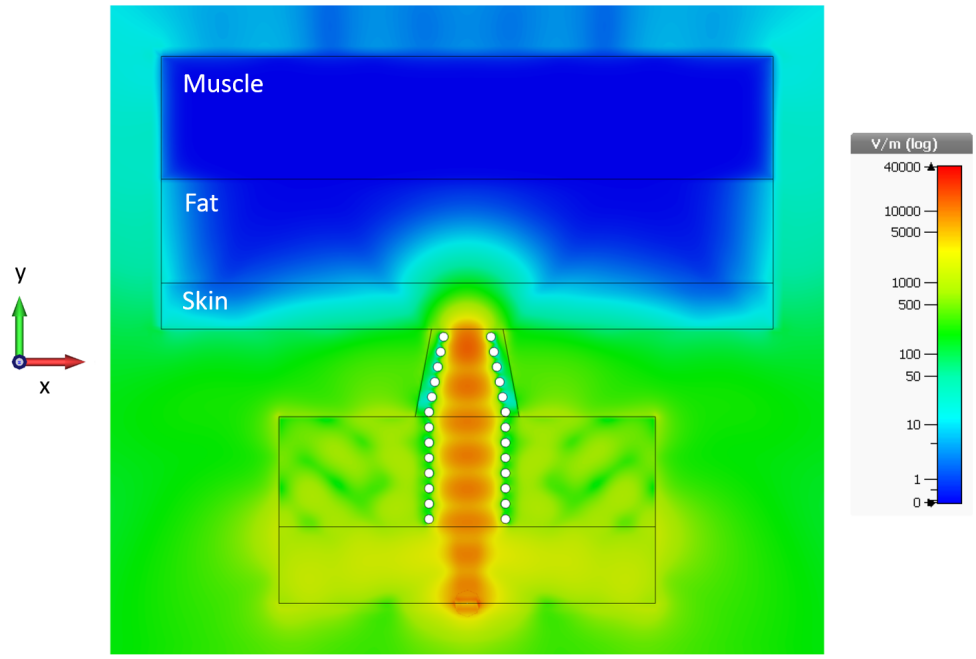

Figure 3.17: Simulated electric field (RMS value [V/m]) along the probe and inside the skin in CST for an input power of 0.5 W: the field increases towards the tip due to the tapering and then rapidly decreases inside the skin

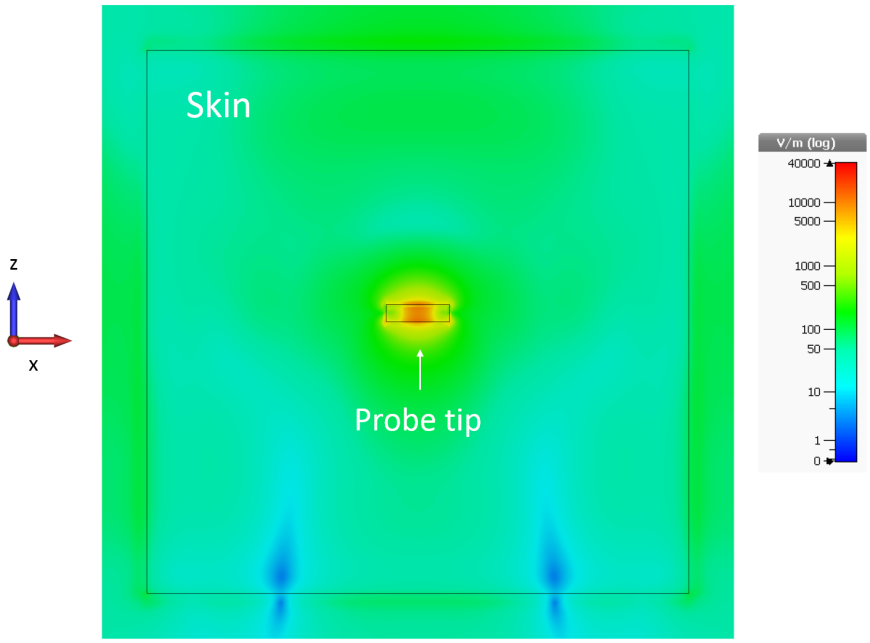

Figure 3.18: Simulated electric field (RMS value [V/m]) on the outer skin surface that is in direct contact with the probe in CST for an input power of 0.5 W: the field is focused on a narrow area corresponding to the probe's tip.

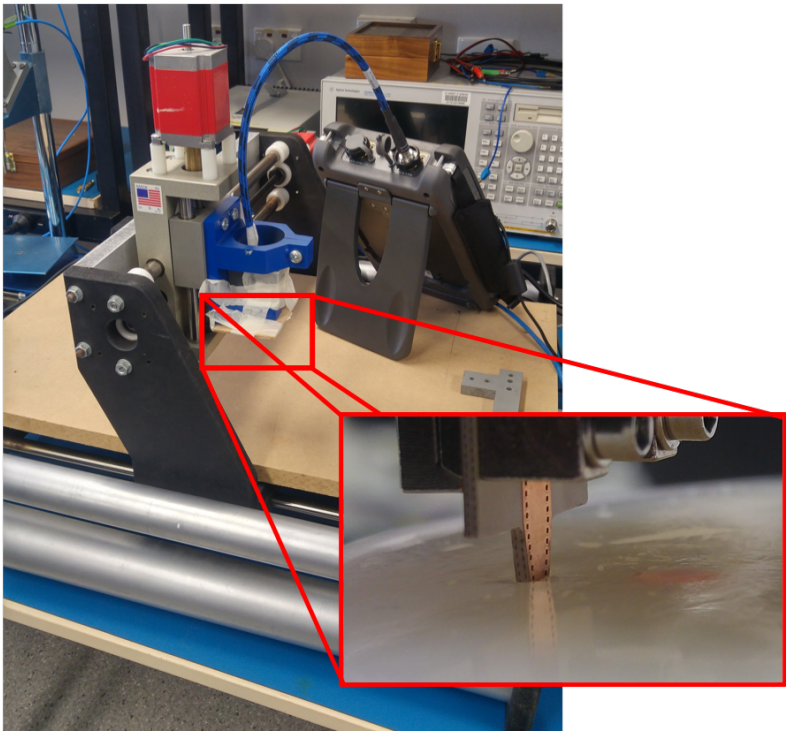

Figure 3.19: Experimental set-up and detail of the correct positioning of the probe on the skin phantom surface: the set-up consists of a VNA attached to the probe that is scanned thanks to a CNC machine.

cause of the noise is to be found in the high frequency connector: according to Southwest Microwave (i.e., the company that produced the connector), the high dielectric constant of the substrate does not work well with the connector, causing most of the noise in the data. Figure 3.20 reports a comparison between the raw and filtered data: it is clear how the moving average filter effectively reduces the noise, especially by comparing the data in the frequency range $42.5 \div 46$ GHz. From this figure it is also possible to notice the three resonant frequencies of the amplitude of the reflection coefficient (highlighted in green): as it was mentioned in the previous section, the probe effectiveness is strictly connected to these peaks.

It must be mentioned that the probe operation frequency is slightly down-shifted with respect to the simulations (as it can be seen by a quick comparison of Figures 3.12 and 3.20) and the main reason of this is the connector. Nonetheless, the probe has been designed to operate between 35 and 45 GHz, hence the down-shift of the operation frequency in the practical scenario does not represent an issue.

Finally the analysis of the acquired data was performed: for each of the three regions highlighted in Figure 3.20, the frequency position and the amplitude of each peak were recorded and mapped into the space domain, i.e., on the 2D scanning grid.

Single-Layer Skin Phantom

Figures 3.21-3.23 depict the 2D and 3D imaging of a 5x5 mm^2 cancer target placed on the surface of the single layer skin phantom in correspondence of the three frequency ranges of interests highlighted in Figure 3.20: it is clear as in all the three cases, the probe

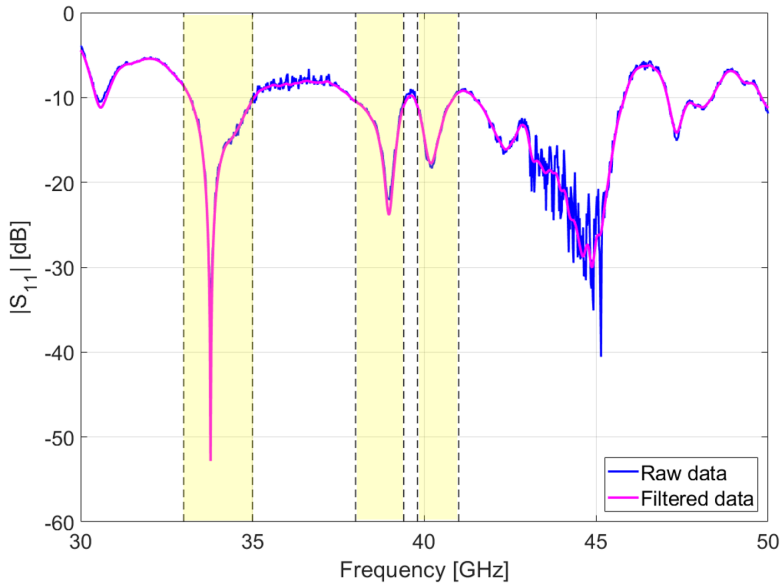

Figure 3.20: Example of a measurement acquisition from the probe before and after data smoothing: the probe acquires three different measurements, then the first one is smoothed through a Gaussian-shaped moving average filter. The effect of the filter is particularly visible in the frequency range $42.5 \div 46$ GHz. The intervals around the local minima are highlighted in green.

is capable of detecting the presence of cancer by revealing changes both in the frequency position and amplitude of the reflection coefficient in all three frequency ranges.

Three-Layers Skin Phantom

The probe was also tested on the three-layers skin phantom depicted in Figure 3.8, but in this case there have been some issues in the measurements acquisition process. In fact, the three layers skin phantom, that is made by three very thin layers of different materials that mimic skin, fat and muscle respectively, is constituted mainly of water corn flour and gelatine (see Section 3.3.1): this leads to a fast evaporation of water from the phantom leading it to shrink during the measurements acquisition as depicted in Figure 3.24.

Nonetheless, the acquired data have been analyzed and led to the 2D imaging presented in Figure 3.25. It can be easily seen how the quality of the image is compromised due to the phantom shrinkage: anyway, even in this case the different spots of cancer material can be identified even in this case.

3.7 Further Simulative Results

In order to determine the sensing depth and the lateral resolution of the probe, i.e., the smallest cancer in termas of horizontal dimensions that can be detected by the probe, further full-wave numerical simulations were performed. In fact, as it was pointed out above, it is difficult to realize an arbitrarily small cancer phantom and place it at a very specific depth inside the skin: on the other hand this is very handy to do in simulations.

First of all, in order to establish the sensing depth of the probe, its definition is needed:

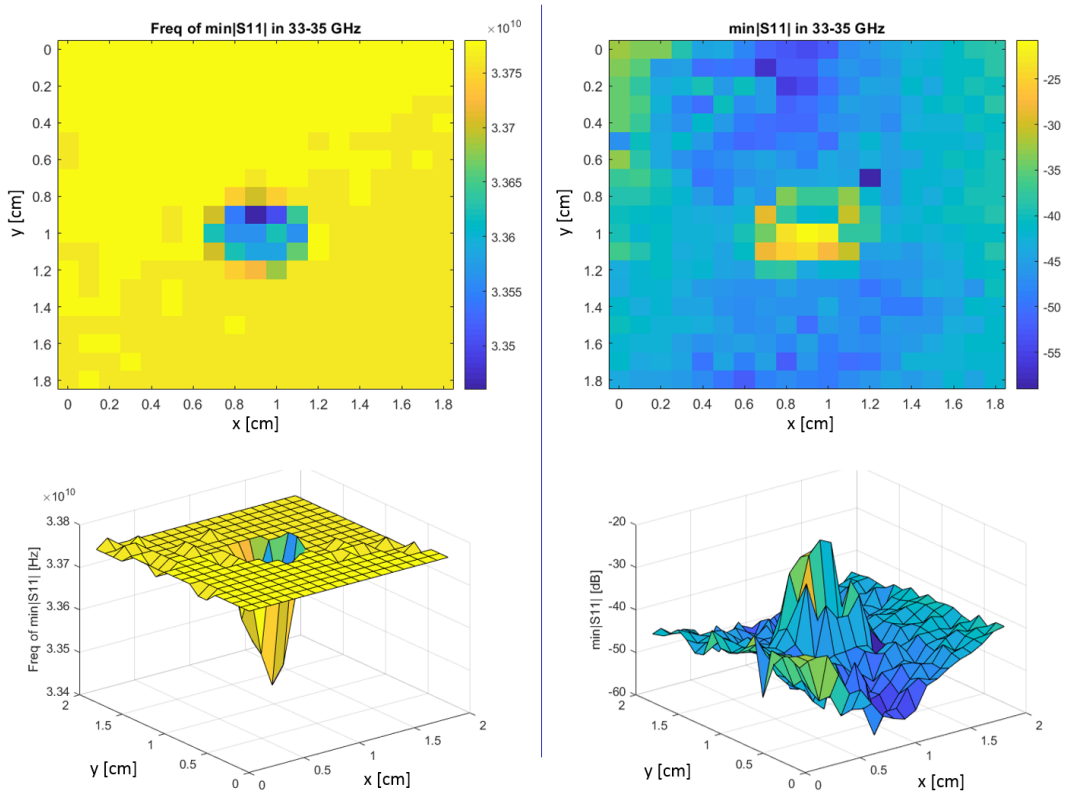

Figure 3.21: 2D (top) and 3D (bottom) imaging of a 5 mm x 5 mm cylindrical cancer target by tracking changes in the frequency (left side of the picture) and amplitude (right side of the picture) of the minimum value of $|S_{11}|$ in the frequency interval $33 \div 35$ GHz (see Figure 3.20).

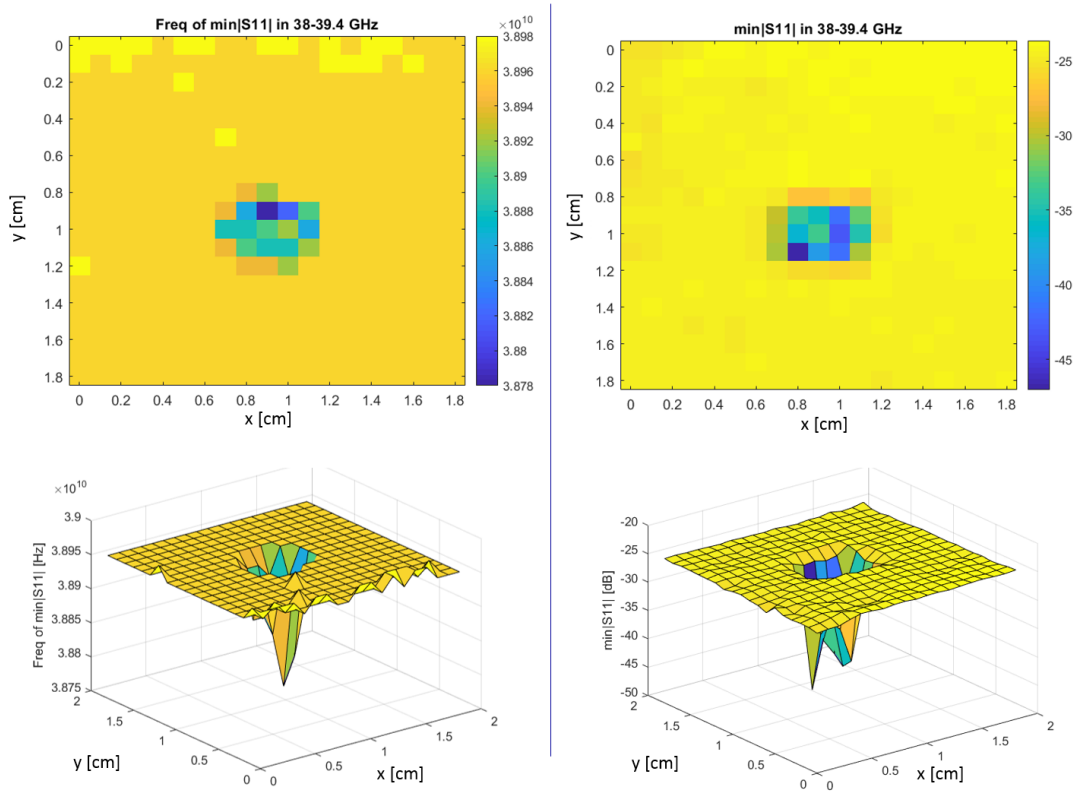

Figure 3.22: 2D (top) and 3D (bottom) imaging of a 5 mm x 5 mm cylindrical cancer target by tracking changes in the frequency (left side of the picture) and amplitude (right side of the picture) of the minimum value of $|S_{11}|$ in the frequency interval $38 \div 39.4$ GHz (see Figure 3.20).

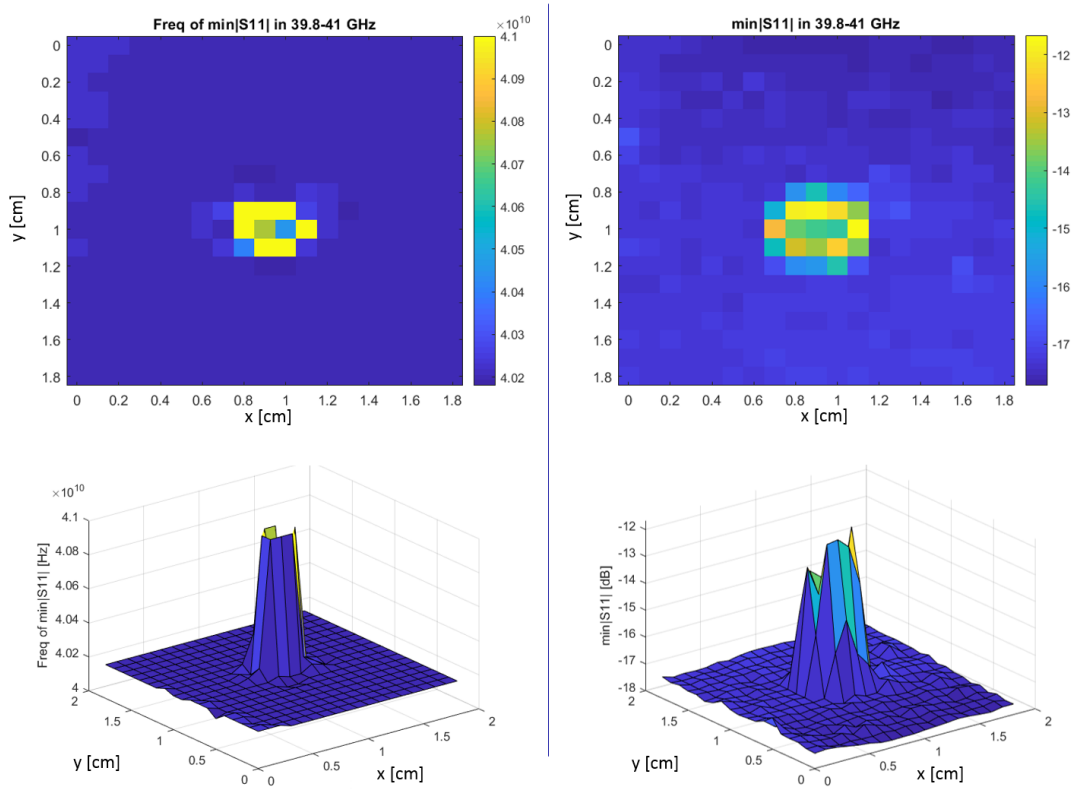

Figure 3.23: 2D (top) and 3D (bottom) imaging of a 5 mm x 5 mm cylindrical cancer target by tracking changes in the frequency (left side of the picture) and amplitude (right side of the picture) of the minimum value of $|S_{11}|$ in the frequency interval $39.8 \div 41$ GHz (see Figure 3.20).

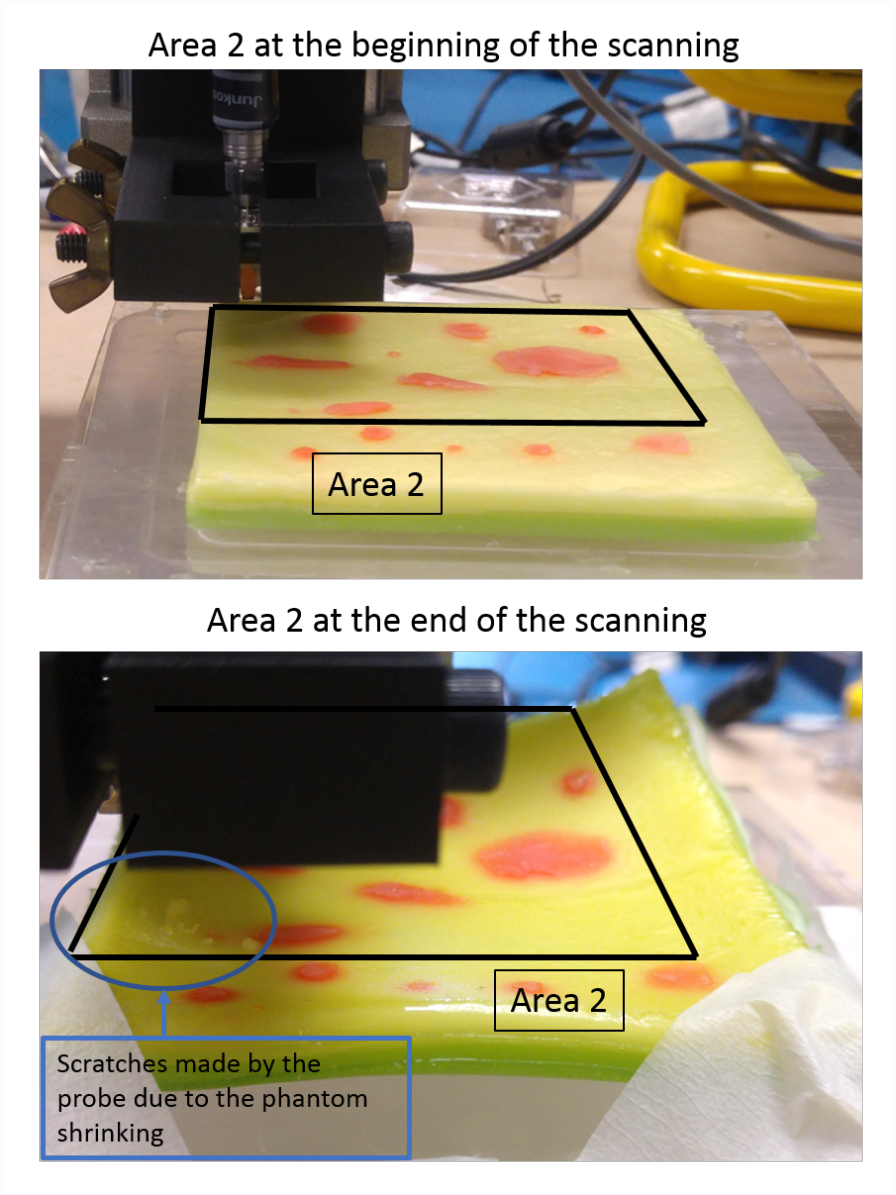

Figure 3.24: Three-layers skin phantom at the beginning and at the end of the scanning process.

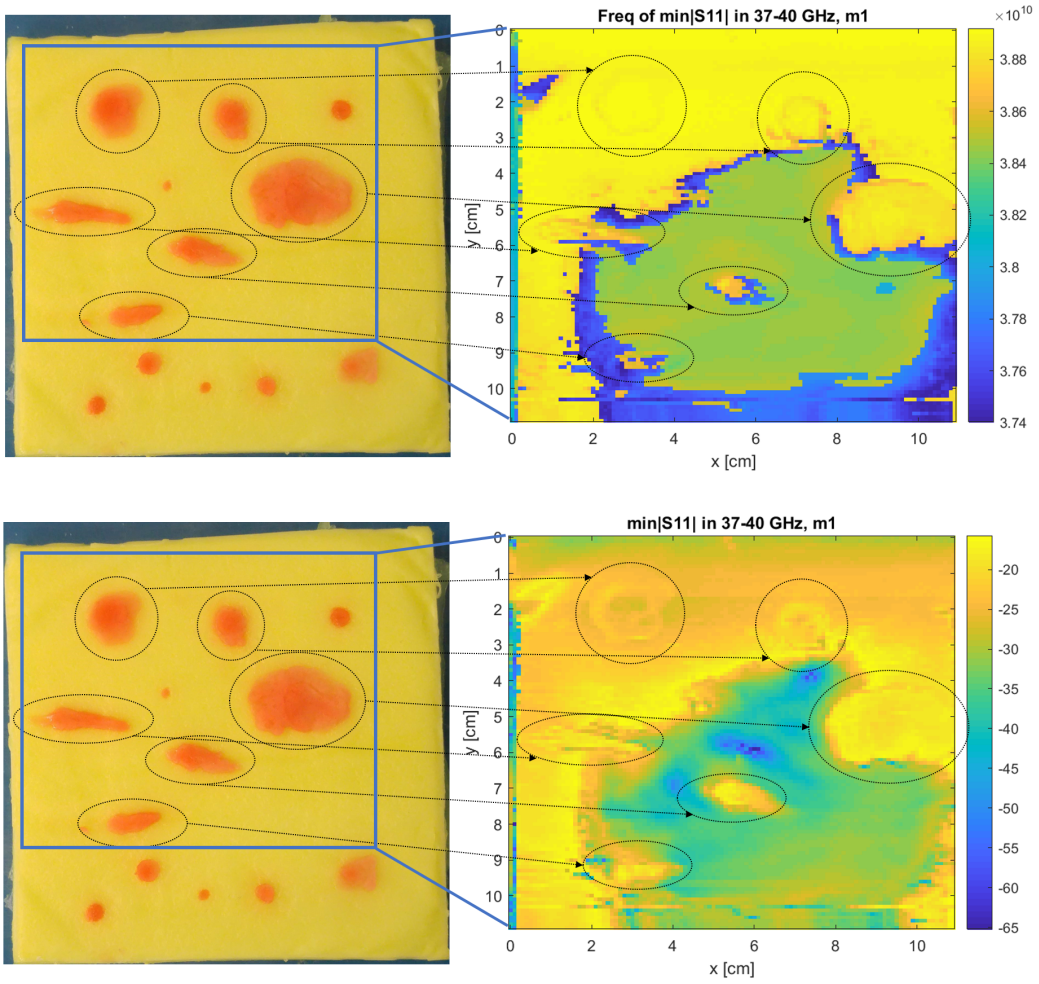

Figure 3.25: 2D imaging of the three-layers skin phantom: changes in frequency (top) and amplitude (bottom) of the reflection coefficient minimum in the frequency range $37 \div 40\,\mathrm{GHz}$.

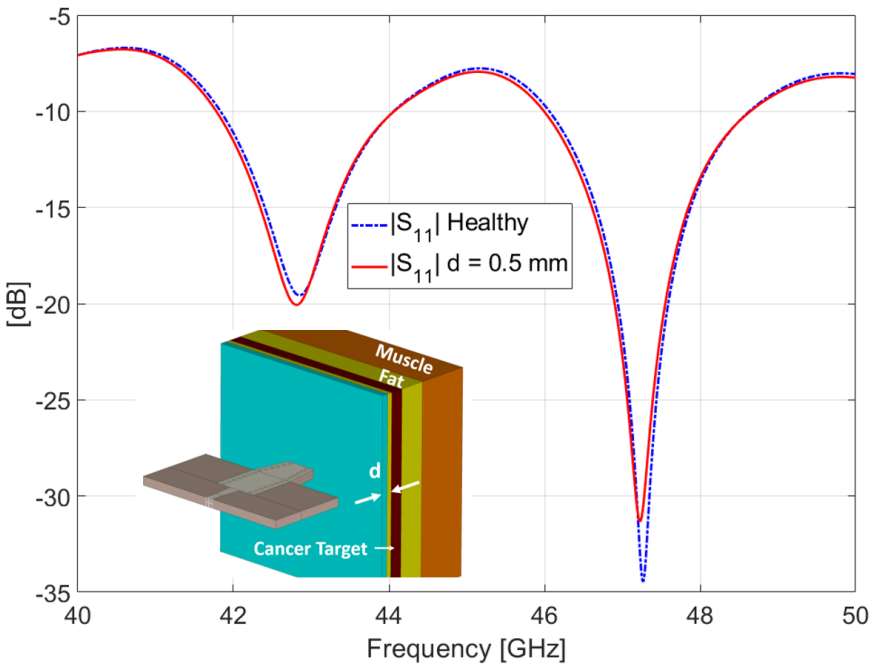

Figure 3.26: Comparison between the reflection coefficient measured by the probe with healthy skin and with a cancer target placed at distance d as described in Figure 3.27. In the top graph the target is placed right after the end of the skin layer, while in the bottom one the target is placed at the penetration depth of the probe

this concept in fact, is not the same as the penetration depth (i.e., the depth at which the E-field is $E = 1/e \cdot E_{ref}$).

Definition 1. *The sensing depth of a skin cancer detecting device is the maximum distance from the skin surface such that, if a cancer target is placed at this distance, it can be detected by the device.*

As it can be seen from Figure 3.26, the sensing depth of the probe is 0.5 mm: this value is high enough to detect the presence of a cancer buried at the bottom of the epidermis in a piece of thick skin (around 2 mm thick), and at the same time it is low enough not to detect targets placed in the fat layer in the case of thin skin (around 0.5 mm thick). In order to determine this value, a cancer target was placed at a depth d from the skin surface (as it is shown in details in Figure 3.27), and the worst case scenario of thin skin (0.5 mm thick) was assumed: the aim was to assess that the probe cannot sense anything underneath the subcutaneous fat layer. A parameter sweep was performed in CST with d (i.e., the depth of the cancer target from the skin surface) varying in the interval 0 – 4 mm with steps of 0.2 mm. For each of these values the reflection coefficient was obtained through simulations and then compared with the one acquired for the healthy skin scenario. The cancer target was modeled as a box with the same lateral dimensions as the skin phantom (see Figure 3.27): in this way we are sure that the variations of the reflection coefficient depend exclusively on the depth at which the target is placed and not on its diameter or shape.

As far as the lateral resolution of the probe is concerned, this is 0.2 mm, and therefore the device can detect the presence of very small early-stage tumors. This can be seen from

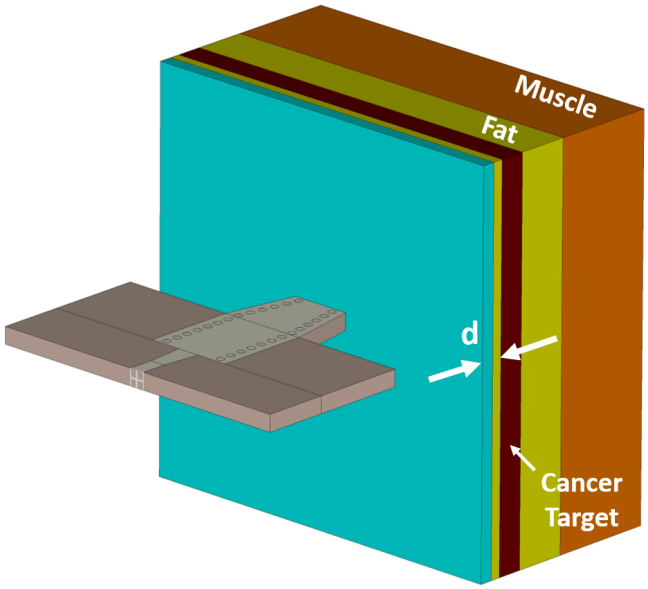

Figure 3.27: Simulative scenario to determine the sensing depth of the probe.

Figure 3.28. In order to determine this value, simulations were run by scanning the probe along a line parallel to its longer tip's face and perpendicular to a cancer target placed at the center of a uniform skin layer. In a similar fashion with respect to what was done to determine the sensing depth, the target was modeled as a tumor parallelepiped with the same dimensions of the skin layer into which it is inserted except for its width (that is varied to determine the sensing depth of the probe): this was done in order to be sure that the only responsible for the change in the $|S_{11}|$ is the width of the cancer, and not its depth, position, and so on and so forth.

Moreover, it can be noticed how the probe's sensitivity varies with respect to which face is orthogonal to the horizontal cancer target during the scanning: as expected, when the probe is scanned along a line that is parallel to its wider tip's face (see Figure 3.28), it can achieve a higher resolution than when it is scanned in the other direction. This fact can be clearly seen by a comparison between Figures 3.28 and 3.29: these report the results of the probe scanning in correspondence of the minimum discernable target in the two cases, i.e., 0.2 mm and 0.5 mm respectively.

3.8 Future Work

One of the advantages of the approach presented so far, is the use of the information about the changes in both frequency and amplitude of the reflection coefficient: the vast majority of the works that can be found in literature rely only on the information about the amplitude. The additional information regarding the changes in the frequency position of the minima of $|S_{11}|$ can be a powerful tool to make the overall approach more reliable. Therefore as a next step, it would be interesting to build a function that combines these two information. The function should approximately look like this:

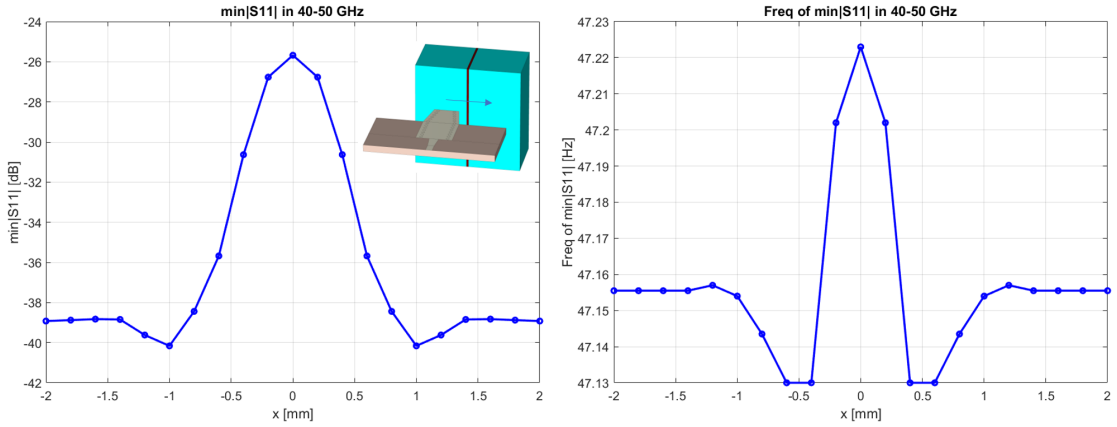

Figure 3.28: Minimum of $|S_{11}|$ (left) and correspondent frequency (right) as detected by the probe while it is scanned along a line parallel to its wider tip edge (see inset), and in correspondence of the minimum detectable target (0.2 mm wide).

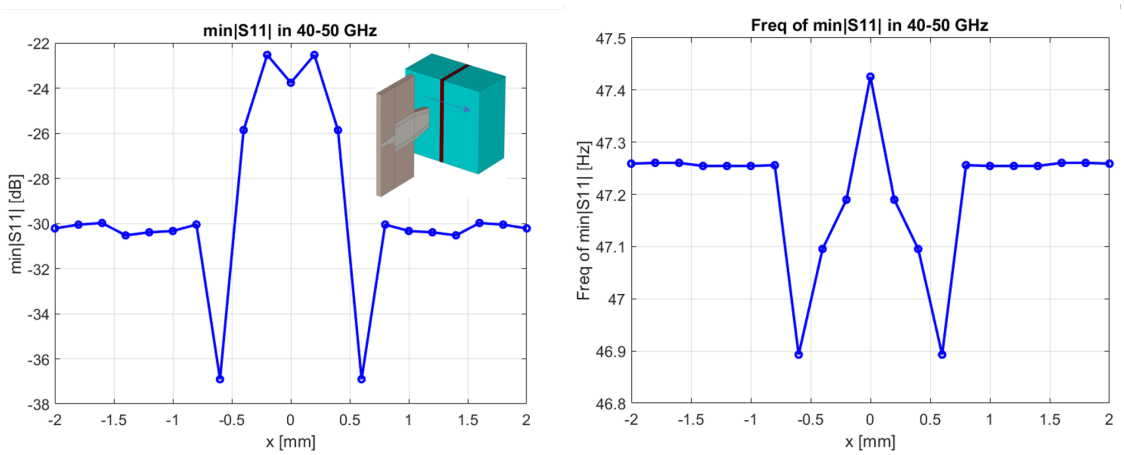

Figure 3.29: Minimum of $|S_{11}|$ (left) and correspondent frequency (right) as detected by the probe while it is scanned along a line parallel to its wider tip edge (see inset), and in correspondence of the minimum detectable target (0.2 mm wide).

$$C(x,y) = a\frac{||S_{11}(f_m^h)| - |S_{11}(f_m(x,y))||}{|S_{11}(f_m^h)|} + b\frac{|f_m^h - f_m(x,y)|}{f_m^h} \tag{3.3}$$

where f_m^h represents the frequency of the minimum of $|S_{11}|$ at the beginning of the scan, i.e., on the healthy region, and $f_m(x,y)$ represents the frequency of the minimum of $|S_{11}|$ at the current position (x,y).

3.9 Conclusions

A millimeter-wave near-field probe designed for early-stage skin cancer detection was presented. The probe is fed through a microstrip line and it is based on SIW technology, hence it is cheap and easy to fabricate. Moreover the substrate has a dielectric constant that ensures that the probe can be used in direct contact with the skin, making it practical and easy to use. The probe has been designed in order to work according to a differential approach, and to be able to detect a cancer target as small as 0.2 mm in diameter buried as deep as the bottom of the epidermis layer both in thin and thick skin (i.e., at 0.5 mm). An array of such probes can be built making the scanning procedure even faster and easier. Furthermore, even though a VNA was used to monitor changes in the reflection coefficient, this is not necessary, and as a future improvement, a system can be built in such a way that it comprises only the probe and a MMIC to analyze the collected data. In this way, a practical, cheap and easy-to-use system can be realized providing a concrete aid in the detection of early-stage skin cancer.

Chapter 4

Study and Design of Gaseous Plasma Antennas

4.1 Summary

Gaseous Plasma Antennas (GPAs) are antennas that exploit partially or fully ionized gas to transmit and/or receive electromagnetic (EM) waves. They present some interesting advantages with respect to their metallic counterparts: they can be electrically (rather than mechanically) reconfigured with respect to some antenna parameters and they are also transparent to EM waves when the plasma is off and when the frequency of the impinging EM signal is above the plasma frequency. However, this interesting technology presents some important limitations: for example, it is difficult to match plasma loads and to fabricate small plasma antennas that operate in the GHz regime.

During my Ph.D. I have worked on the design of three plasma antennas: a reconfigurable metal-plasma Yagi-Uda antenna, an active plasma dipole working at roughly 1 GHz and a crossed dipole working at the same frequency. Both works have been conducted in collaboration with CISAS B. Colombo, an aerospace engineering research center of the University of Padova.

The active and crossed plasma dipoles provided good results in full-wave numerical simulations (in CST Microwave Studio), but proved to be cumbersome to fabricate and feed in practice: in fact, when dealing with CST simulations, it is sufficient to place a discrete face port in the gap between the two arms of a dipole in order to feed it, while in practice the design of a proper signal coupler represents a challenge. Moreover, the electrodes and the other equipment used to generate the plasma have a non-negligible influence on the operation frequency of the dipole, making it harder to realize an antenna that operates at frequencies higher than some hundreds of Megahertz.

As far as the hybrid Yagi-Uda antenna is concerned, this proved to be a good solution to exploit plasma reconfigurability features avoiding at the same time some of the issues related to this technology: the use of a classic metal dipole as the active element of the antenna simplifies the feeding of the structure, and at the same time the adoption of plasma discharges as directors allows to create an antenna that can be reconfigured with respect to its gain.

This chapter is organized as follow. First the main advantages and issues of GPAs are

presented in the introduction, then a brief description of the plasma model used in all the simulations is introduced and finally the antennas that have been studied and designed are presented: the hybrid metal-plasma Yagi-Uda antenna, the active plasma dipole and the crossed plasma dipole.

4.2 Introduction: Gaseous Plasma Antennas

Traditional antennas exploit metallic components to radiate and/or receive electromagnetic waves. In recent years there has been an increasing interest in another type of antennas, namely Gaseous Plasma Antennas (GPAs), whose radiating properties rely on partially or fully ionised gas, i.e., plasma, rather than on metallic conductors [56] [57].

In GPAs, a neutral gas is confined into a dielectric vessel such as a glass cylinder, monopole or loop: plasma can be artificially generated from this gas by different excitation means, like for example by heating the gas or subjecting it to a strong electromagnetic field to the point where it becomes ionised and increasingly electrically conductive, and so its behaviour is dominated by electromagnetic fields [58]. In fact, when the plasma is turned on, the electrons orbiting atomic nuclei are stripped away, thus creating free electrons (whose number is related to the gas temperature and density) that makes the plasma behave like an electric conductor that is able to transmit and receive EM signals. When the plasma is turned off, it reverts to a neutral gas that is confined in a dielectric enclosure, thus being transparent to any electromagnetic wave.

4.2.1 Gaseous Plasma Antennas: Advantages

Plasma antennas have a number of potential advantages over conventional metal antennas since their properties can be electrically (rather than mechanically) controlled. This makes plasma antennas appealing for a number of applications, some of which are briefly discussed in the followings [57] [59].

First of all, when a plasma discharge is unenergized, the gas reverts to its neutral state and so it stops behaving as a conductor. This feature makes plasma antennas difficult to be detected by a radar, once the plasma vessel and excitation system are properly designed and if the antenna is energized only when the communication takes place. This property leads to a potential interest in plasma antennas for military applications.

Secondly, plasma antennas are transparent to EM waves whose frequency is above the plasma frequency; this feature makes plasma antennas interesting when dealing with applications that need many antennas (or antenna arrays) used for different communication systems that must be stacked together due to space constraints (e.g., ship-borne maritime communications) and that operate at different frequencies. In this case plasma elements are an interesting alternative to conventional metallic ones since they can provide significantly lower mutual coupling values among the different arrays; as a matter of fact, unenergized plasma elements do not interfere with active elements, and the coupling among plasma antennas working at different frequencies is significantly lower than the one provided by metallic antennas.

Additionally, plasma elements can be energized and de-energized on time scales of microseconds; as a result, the signal degradation caused by antenna ringing can be greatly

reduced by using a plasma antenna transmitting at high rates and that is switched off at the end of each bit.

Finally, the radiation properties of a plasma antenna can be changed by electrically controlling the plasma parameters (e.g., density), which can be achieved by tuning the power delivered to the plasma. Therefore plasma antennas can be rapidly reconfigured with respect to their radiation pattern, input impedance, and working frequency.

4.2.2 Gaseous Plasma Antennas: Issues

Even though plasma antennas have some interesting advantages with respect to their metallic counterparts, the usage of plasma discharges as antennas in communication systems can be hindered by several issues such as the noise introduced by the plasma, the complexity of the plasma antenna, and the availability of suitable technology solutions to generate the plasma.

The noise introduced by the plasma is strongly related to the way the plasma is generated, and this fact has been holding back the use of plasma antennas for many years. Different plasma generation techniques are available: laser-initiated atmospheric discharge [60], DC/AC discharge [61], and radio-frequency (RF) surface-wave plasmas [62]. Both DC and low-frequency AC methods introduced a rather high noise level when generating the plasma. RF surface wave generation and the pulsing power technique made it possible to obtain not only lower noise levels, but also higher plasma density and reduced power consumption [57].

Another obstacle to the exploitation of plasma antennas can be identified in the inherent complexity of plasma antennas. Specifically, a plasma antenna comprises not just the plasma, but also the equipment needed to generate it (e.g., the metallic electrodes in the case of a RF surface-wave-generated plasma). Furthermore, the plasma density in an actual plasma discharge is nonuniform, with a non-uniformity that depends on the plasma generation technology; before considering the actual realization of a plasma antenna, it is therefore necessary to develop a representative prototype of the plasma discharge the antenna will be comprised of, and to measure the plasma density therein. As a result, the presence of electrodes, and the nonuniform plasma distribution within the discharge are expected to affect the radiation properties of the actual plasma antenna, and are to be taken into account in the design, and realization of an actual plasma antenna.

Other critical aspects towards the realization of an actual plasma antenna, are the availability of the proper technology to ignite, and sustain the plasma, and the capability of developing customized dielectric vessels whose shape and dimensions must be carefully chosen according to the antenna type (e.g., monopole, dipole) and operating frequency.

4.3 Plasma Model

In all the designs presented in this chapter, the plasma discharges are modeled in the same way, regardless of their usage as active or passive elements. Specifically, the discharges are made of a weakly ionized plasma in which the thermal motion of the ions can be discarded, and the density is not disturbed by an impinging EM wave. Under these assumptions, the cold-plasma approximation and the fluid model are well justified to represent the

plasma response [63]; in addition, we have assumed that the plasma discharges have been preformed by some excitation circuits, whose effect on the radiation properties of the antenna is not considered in this work. The main analysis and design tool that has been used throughout all the works presented here is CST Microwave Studio: in this simulation environment the relative dielectric permittivity of the plasma is well described by a Drude model that reads:

$$\epsilon_r = \left(1 - \frac{\omega_p^2}{\omega^2 + \nu^2}\right) - j\frac{\nu}{\omega}\left(\frac{\omega_p^2}{\omega^2 + \nu^2}\right) \tag{4.1}$$

where:

- $\omega = 2\pi f$ is the angular frequency of the incident EM wave (i.e., the signal),
- ν is the momentum-transfer collision frequency of electrons with heavy particles (ions/atoms),
- $\omega_p = [n_e e^2/m_e\epsilon_0]^{1/2}$ is the electron plasma frequency,
- m_e and e are the electron mass and charge respectively,
- ϵ_0 is the free space permittivity,
- n_e is the local plasma electron density that is assumed to be uniform within the discharge.

Figure 4.1 reports the real and imaginary parts of the relative dielectric permittivity of the plasma ϵ_r in the low GHz regime, i.e., the range close to the frequencies of interest when the plasma frequency and collision frequency are $\omega_p = 178.4$ GHz and $\nu = 103.28$ MHz respectively. These values are those used to model the preliminary ideal plasma discharges used as directors of the hybrid Yag-Uda antenna presented in [5].

By turning off the plasma discharges, the electrons and ions that form the plasma recombine to yield a neutral gas, whose permittivity is approximately the same as that of free space: this is defined as the *off* state of the plasma.

Similarly to what has been done for optical antennas [64], the length of the plasma discharge has been calculated by taking into account the effective wavelength λ_{eff} experienced by the plasma, which is shorter than the free-space wavelength [65]. To this end, we have calculated the modes of the cylindrical plasma discharge that can sustain surface-wave propagation for frequencies below the electron plasma frequency ω_p. The plasma discharge can be regarded as an open waveguide that is filled with a uniform non-magnetized plasma endowed with relative dielectric permittivity ϵ_r. The modes of this cylindrical waveguide are solutions of the equation:

$$\frac{k_{\perp p}}{\epsilon_r}\frac{I_0(k_{\perp p}r_p)}{I_1(k_{\perp p}r_p)} + k_{\perp 0}\frac{K_0(k_{\perp 0}r_p)}{K_1(k_{\perp 0}r_p)} = 0 \tag{4.2}$$

where:

- r_p is the plasma radius,

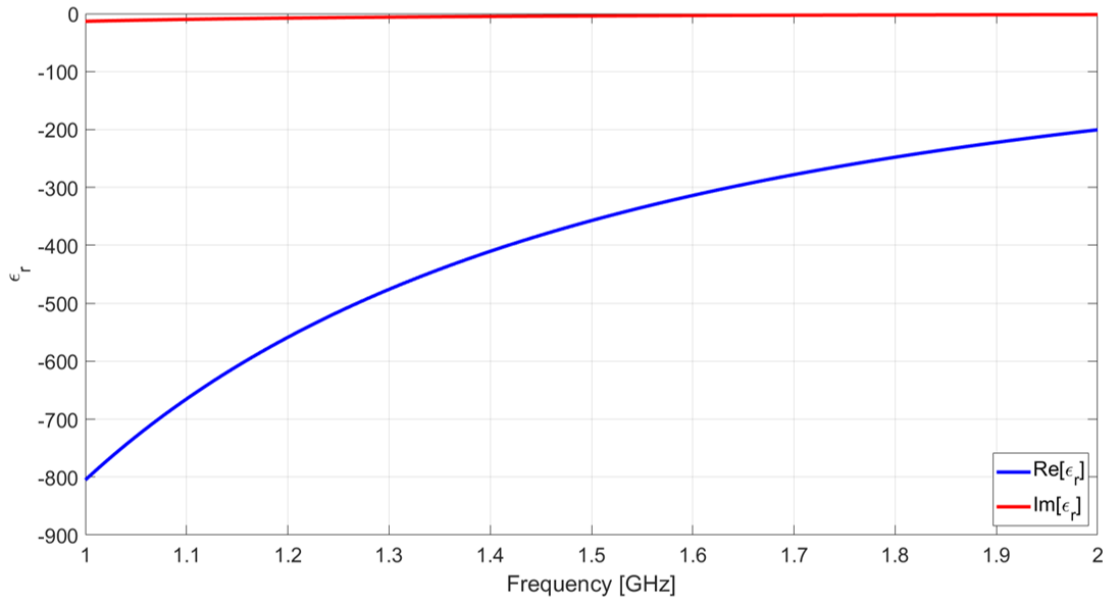

Figure 4.1: The relative dielectric permittivity of the plasma when the plasma frequency and collision frequency are $\omega_p = 178.4$ GHz and $\nu = 103.28$ MHz respectively: real (bottom blue curve) and imaginary (top red curve) part.

- $k_{\perp p} = \left(\beta^2 - \omega^2 \epsilon_r / c^2\right)^{1/2}$ is the transverse propagation constant in the plasma,
- $k_{\perp 0} = \left(\beta^2 - \omega^2 / c^2\right)^{1/2}$ is the transverse propagation constant in free space,
- β denotes the propagation constant along the plasma column,
- I_i and K_i with $i = 0, 1$, are modified Bessel functions of the first and second kind, respectively.

This allows to determine the effective wavelength of the plasma at the frequency of interest and hence to set the length of the plasma discharges accordingly.

4.4 Hybrid Metal-Plasma Yagi-Uda Antenna

In order to exploit the reconfigurability of plasma antennas and at the same time to overcome some of the issues related to the usage of plasma discharges as radiating elements, a hybrid metal-plasma Yagi-Uda antenna for microwave applications (also addressed as *hybrid antenna*) has been designed: the active element and the reflector of this antenna are constituted by classic dipoles, while two plasma discharges are used as directors. In this way the antenna can be reconfigured with respect to its gain simply by turning on/off the plasma discharges. In particular, the directors of the antenna are constituted of micro-plasma discharges that allow to realize very *thin* and short plasma tubes, thus overcoming some issues related to the use in the GHz regime of classic *thick* plasma discharges. At the same time the use of a conventional metallic dipole as the active element of the antenna allows to solve the impedance matching problems related to the usage of plasma dipoles as active element: in fact, a plasma discharge used as a

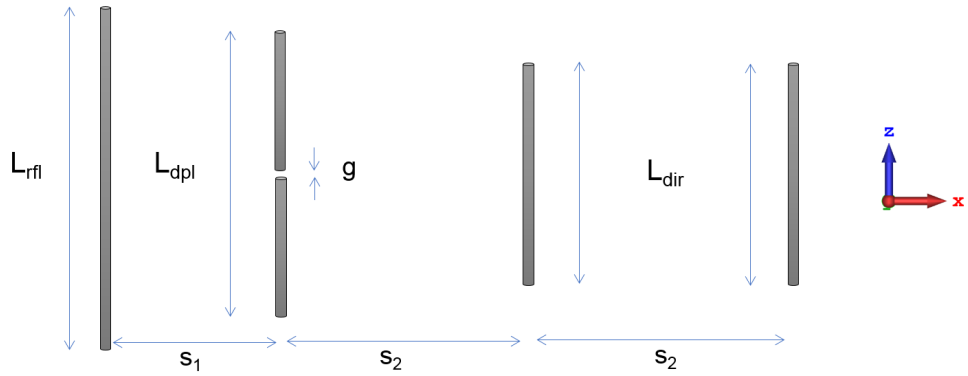

Figure 4.2: CST model of the classic (i.e., metallic) Yagi-Uda antenna.

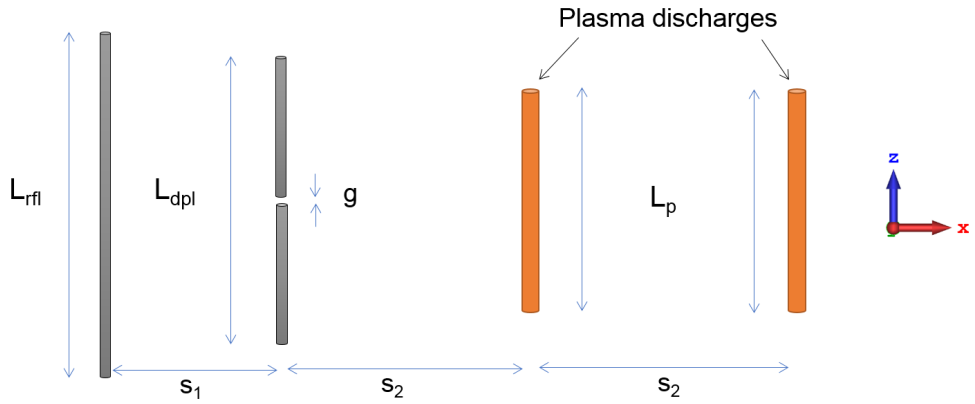

Figure 4.3: CST model of the preliminary design of the hybrid metal-plasma Yagi-Uda antenna.

radiating element might show low input impedance values (i.e., $< 5\ \Omega$ [66]), thus leading to matching issues, and ultimately, to low total efficiency values.

4.4.1 Hybrid Antenna: Preliminary Study

First of all, a feasibility study of the hybrid antenna operating at 1.55 GHz was published in [5]. This work presents a basic version of the antenna designed in CST Microwave Studio: the plasma directors are modeled simply as two cylinders made of a uniform Drude material, neglecting both the glass vessels and the electrodes, and considering ideal values of plasma and collision frequency that are not easily achievable in practice. Moreover, the *off* state of the plasma discharges is modeled merely by excluding the plasma cylinders from simulations.

Antenna Design

First of all, a classic metallic Yagi-Uda antenna was considered and taken as reference to assess the performance of the hybrid antenna. As it can be seen from Figure 4.2, the antenna comprises a reflector, a half-wavelength dipole (i.e., the active element), and two directors; all the elements are cylindrically shaped, and modeled as Perfectly Electric

Conductors (PEC) in CST. The operating frequency of the antenna, i.e., the resonance frequency, was set to $f = 1.55$ GHz, leading to a free-space wavelength $\lambda_0 = 193.55$ mm. To maximize the gain and the total efficiency of this Yagi-Uda antenna, the dimensions of the antenna elements were adjusted according to the common design rules that can be found in [24].

Specifically, referring to Figure 4.2, the length of the reflector is $L_{rfl} = 90.91$ mm, the dipole has a length of $L_{dpl} = 85.45$ mm, and the metal directors $L_{dir} = 73.82$ mm. The distance between the reflector and the dipole is $s_1 = 45.45$ mm, while we have a spacing of $s_2 = 61.82$ mm between the dipole and the first director; the latter is also the distance between the two directors. Finally, all the elements have the same radius, i.e., $r = 0.54$ mm. The dipole is fed through a 50 Ω discrete face-port that is placed in a gap $g = 1.4$ mm between the two halves of the dipole.

As far as the hybrid metal-plasma Yagi-Uda antenna is concerned, this has the same dimensions of the classic antenna, but the directors have been replaced by plasma discharges whose dimensions need to be carefully revised due to the dispersive response of the plasma. The plasma that constitutes the two directors is modeled as described in Section 4.3 and therefore at the frequency of interest $f = 1.55$ GHz the effective wavelength is $\lambda_{eff} = 98.5$ mm, that is associated with a discharge length $L_p = \lambda_{eff}/2 = 49.25$ mm. Therefore the directors have been modeled as two cylindrical plasma discharges of length L_p, and radius $r_p = 1.25$ mm. The hybrid antenna is depicted in Figure 4.3: all the dimensions except for the length and diameter of the plasma directors are the same as for the classic metallic Yagi-Uda antenna. It has to be mentioned that a parametric sweep has been performed in CST in order to determine the best values of s_1 and s_2 but no substantial differences were revealed in terms of gain and efficiency with respect to the values of these parameters used to design the classic metallic Yagi-Uda antenna. Therefore these parameters were kept unchanged. The value of r_p was chosen as the minimum radius achievable by a realistic glass envelope.

Results

The first result involves the impedance of the antenna. As mentioned in the introduction, when a plasma discharge acts as a radiating element, the real part of the impedance at the first resonance (short resonance) is very small, i.e., a few Ωs, leading to matching issues in practical scenarios. The solution to this issue proposed in [5] consists in the adoption of a metal dipole as the active element of the hybrid antenna. In this way, the real part of the antenna impedance is $Re[Z] = 50.82\ \Omega$ at the resonance, i.e., an optimal value for a practical implementation of the antenna.

The resonance frequency is $f = 1.55$ GHz as expected: this can be seen from Figure 4.4 that shows the magnitude of the reflection coefficient of the antenna with no directors (asterisks), one director (triangles) and two directors (circles). Moreover, it can be noticed how the frequency behavior of the hybrid antenna is in perfect agreement with the frequency behavior of its metallic counterpart (Figure 4.5): a part from small changes, the two plots are almost identical. From CST simulations it results also that the efficiency of the hybrid antenna is 98%, both with one and two directors.

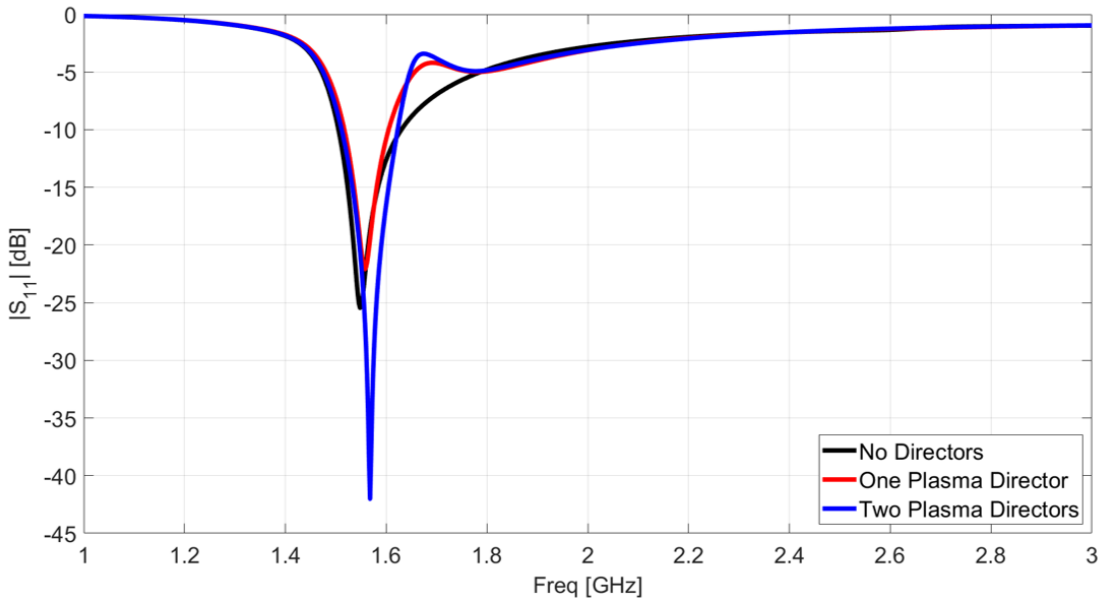

Figure 4.4: Magnitude of the reflection coefficient $|S_{11}|$ [dB] of the hybrid Yagi with: zero (black), one (red) and two (blue) directors.

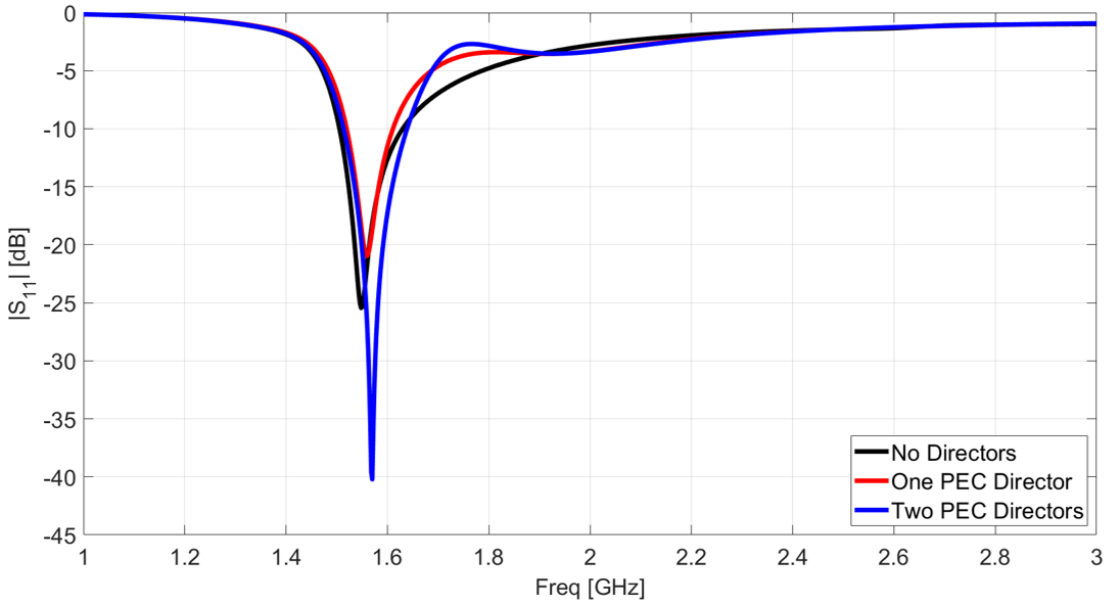

Figure 4.5: Magnitude of the reflection coefficient $|S_{11}|$ [dB] of the classic metallic Yagi-Uda antenna with: zero (black), one (red) and two (blue) directors.

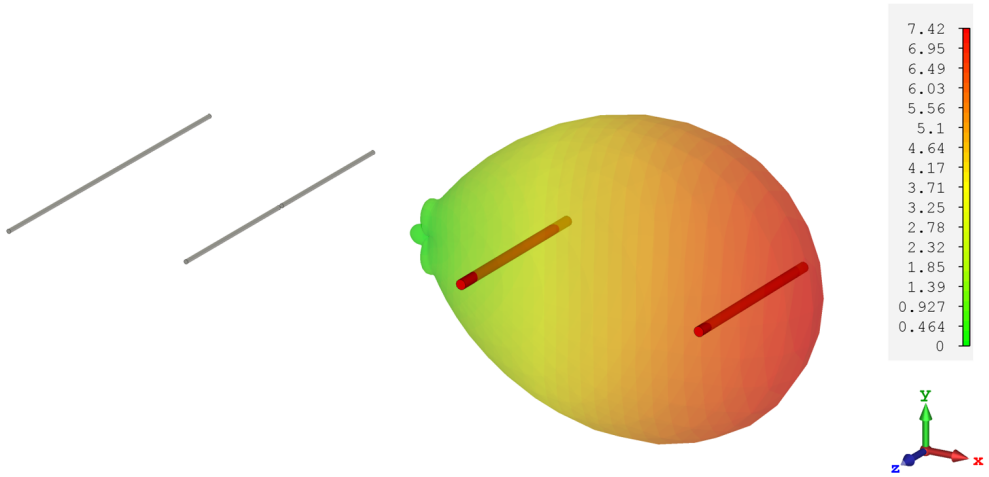

Figure 4.6: Gain of the hybrid Yagi (linear scale) with two directors.

As far as the gain of the hybrid antenna is concerned, three cases have been analyzed: the antenna with no directors, with one, and with two directors. Figure 4.6 shows the three-dimensional gain of the antenna with two directors and shows how the plasma directors are effective in shaping the radiation pattern of the antenna. As shown in Figures 4.7, 4.8, the gain of the antenna increases as the number of directors does the same; specifically, the gain (linear values) is 4.46 with no directors, 6.34 with one director, 7.42 with two directors.

To show the effectiveness of the plasma directors, a comparison between the hybrid antenna and the conventional metal antenna has been performed. Figures 4.9, 4.10 depict the gain of the antenna on the E-plane (i.e., xz-plane in Figures 4.2 4.3) with one/two plasma directors and with one/two metal directors, while Figures 4.11, 4.12 show the gain in the H-plane (i.e., xy-plane) for the same configurations.

It can be seen as in all the cases (one/two directors, E/H-plane) the gain of the hybrid antenna is very close to the one of the classic metal antenna, thus proving that the hybrid antenna is capable of providing both high gain and reconfigurability. In fact, by turning on or off the plasma directors, the gain of the hybrid antenna can be controlled: the higher the number of active plasma directors, the higher the achieved gain. The similarities between the classic and hybrid antennas with respect to the performance, can be noticed also by comparing the electric field behavior in the two case: from Figures 4.13, 4.14 it can be easily evinced that this is very similar in the two cases.

Conclusions

The design of a new hybrid metal-plasma Yagi-Uda antenna working at 1.55 GHz has been presented: the active element is a conventional half wavelength metallic dipole while two micro-plasma discharges have been chosen as directors of the antenna. In this way, reconfigurability with respect to the gain can be achieved by turning on or off the directors; at the same time plasma loads matching issues are avoided thanks to the choice of a metallic dipole as the active element of the antenna. Moreover, this hybrid design choice leads to good results in terms of gain with respect to the classic metal Yagi antenna,

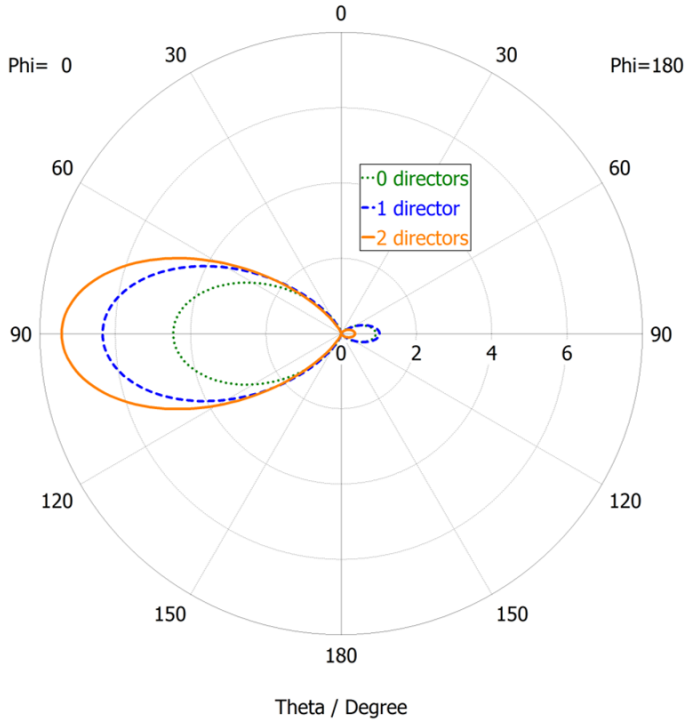

Figure 4.7: Gain of the hybrid Yagi (linear scale) on the E-plane (i.e., xz-plane, see Figure 4.3 with: no director (dotted line), one director (dashed line), two directors (solid line).

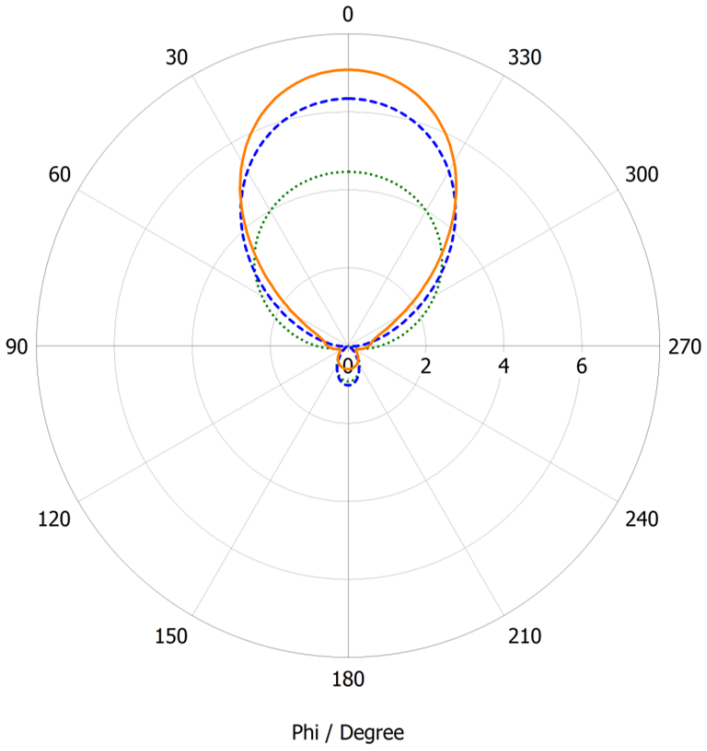

Figure 4.8: Gain of the hybrid Yagi (linear scale) on the E-plane (i.e., xz-plane, see Figure 4.3 with: no director (dotted line), one director (dashed line), two directors (solid line).

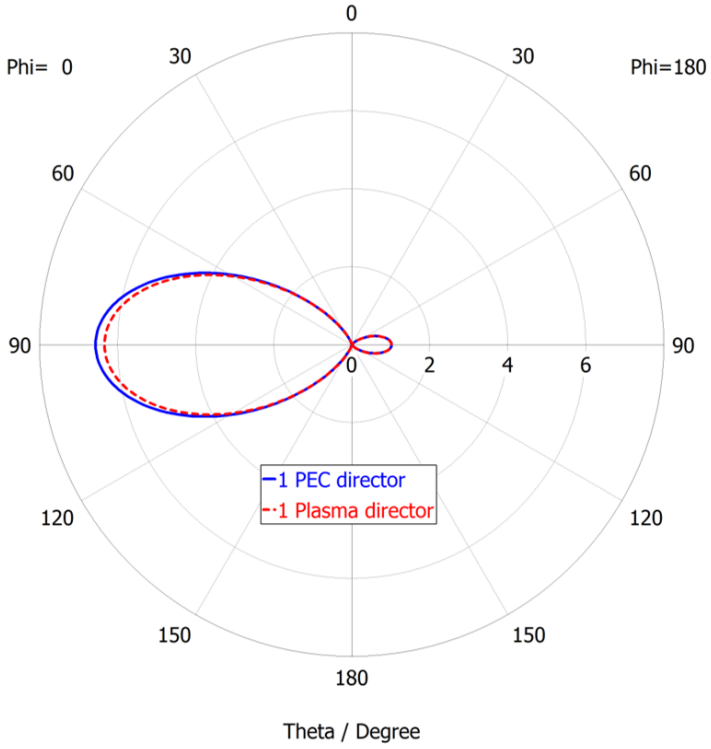

Figure 4.9: Comparison between the gain (linear scale) of the hybrid Yagi (dashed line) and the metal Yagi (solid line) on the E-plane (xz-plane, see Figure 4.3 with one director.

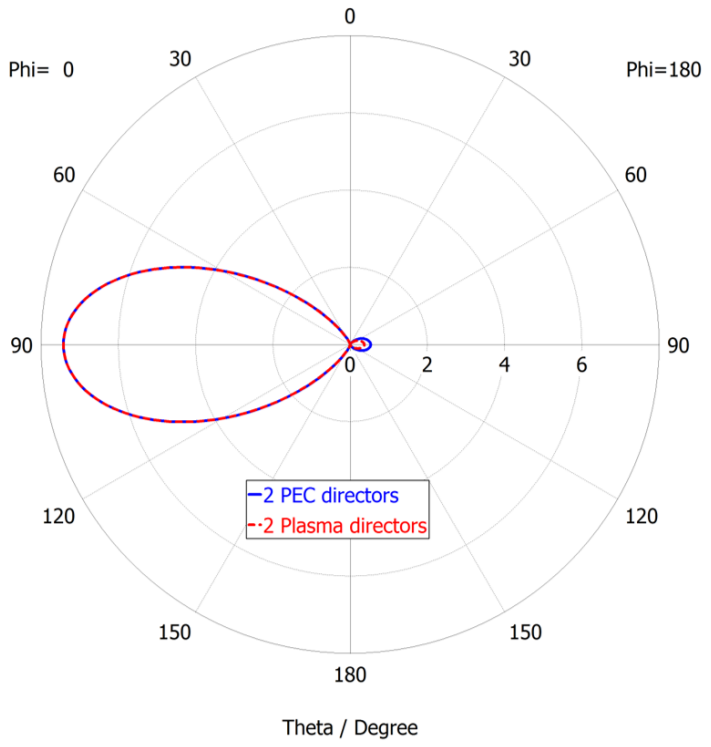

Figure 4.10: Comparison between the gain (linear scale) of the hybrid Yagi (dashed line) and the metal Yagi (solid line) on the E-plane (xz-plane, see Figure 4.3 with two directors.

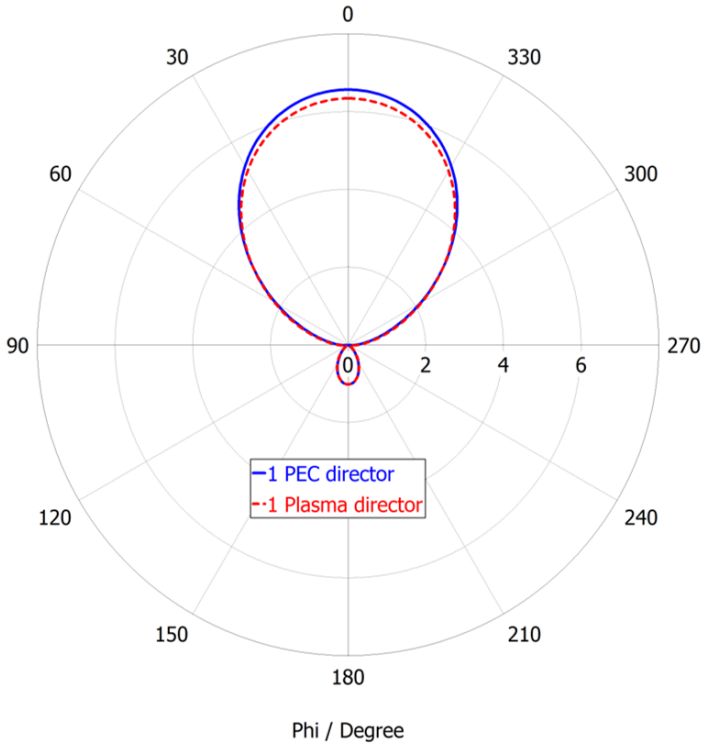

Figure 4.11: Comparison between the gain (linear scale) of the hybrid Yagi (dashed line) and the metal Yagi (solid line) on the H-plane (xy-plane, see Figure 4.3 with one director.

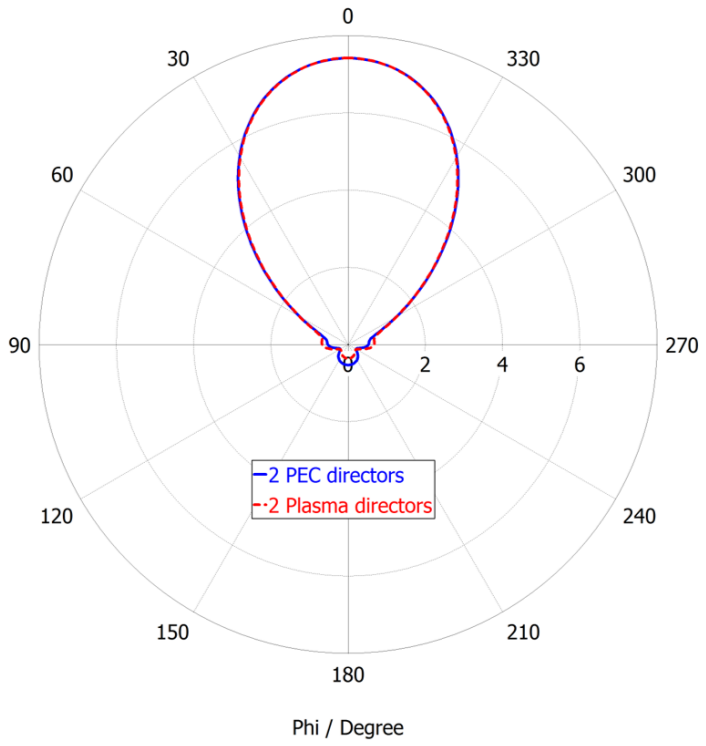

Figure 4.12: Comparison between the gain (linear scale) of the hybrid Yagi (dashed line) and the metal Yagi (solid line) on the H-plane (xy-plane, see Figure 4.3 with two directors.

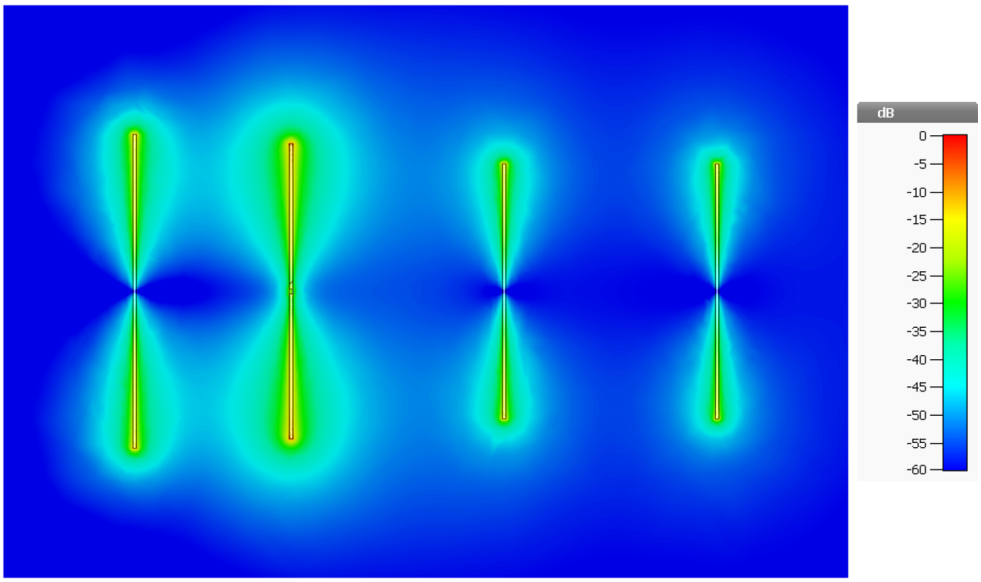

Figure 4.13: Electric field behavior (RMS, logarithmic scale) on the classic metallic Yagi-Uda antenna.

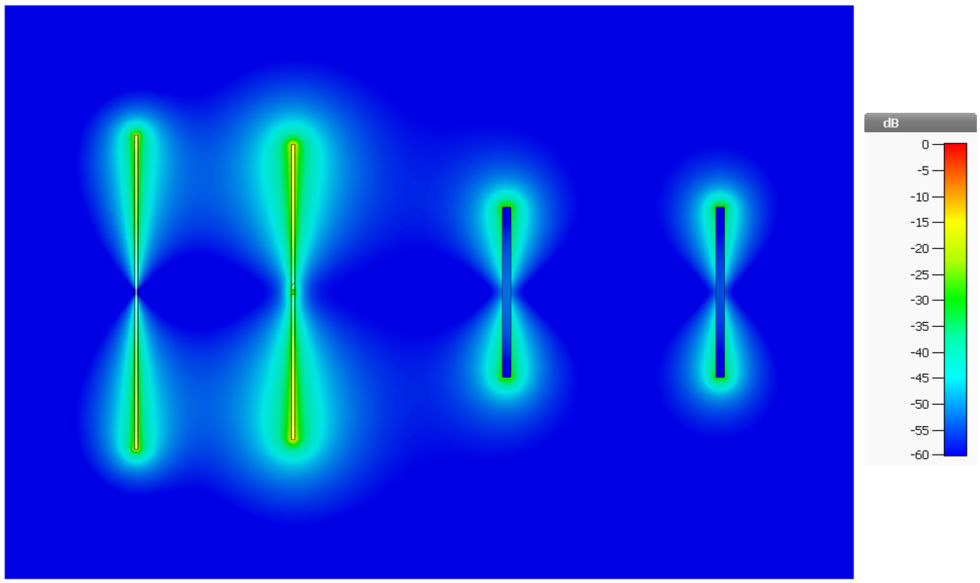

Figure 4.14: Electric field behavior (RMS, logarithmic scale) on the hybrid metal-plasma Yagi-Uda antenna.

thus paving the way to a new class of hybrid reconfigurable antennas operating at high frequencies.

4.4.2 Hybrid Antenna: Realistic Design

The results presented in [5] were obtained under some simplified assumptions. Therefore, as a second step, a more realistic model of the hybrid Yagi-Uda antenna was studied and published in [4]. The major differences between the two models presented in [5] and [4] are the following:

1. the plasma directors comprise both the dielectric vessels and the electrodes instead of being modeled simply as uniform cylinders made of Drude material;
2. the collision frequency and plasma dimensions have been set to more realistic values obtained through experimental characterizations of different plasma discharges;
3. the *off* state of the plasma directors is modeled including the glass cylinders filled with neutral gas (i.e., unenergized plasma) in the simulations;
4. and finally the overall design of the Yagi-Uda antenna was revised according to the above-mentioned differences, i.e., the dimensions of the elements and the distances between them were checked and modified in order to obtain optimal performances.

Realistic Antenna Design

The substantial difference with respect to the work presented in [5] concerns the model of the plasma directors. The weakly-ionized gaseous plasma is again modeled as a dispersive Drude material that follows Equation 4.1, the operating frequency of the antenna is again 1.55 GHz, and also the plasma frequency is $\omega_p = 178.4$ GHz as in [5] since it has been shown by experimental measurements that this is an easily-achievable value in real scenarios.

Regarding the collision frequency that accounts for the dissipation processes inside the plasma, this has been chosen significantly different from [5]: it is $\nu = 2.5067$ GHz instead of $\nu = 0.10328$ GHz, i.e., much higher, since in actual realization of plasma discharges this is a more realistic value.

Therefore the values of ϵ_r are significantly different with respect to [5] and this can be clearly evinced from Figure 4.15 in which the real and imaginary parts of the relative permittivity are reported for the two scenarios. At the frequency of interest 1.55 GHz the real and imaginary parts of ϵ_r are $\mathrm{Re}[\epsilon_r] = -314$ and $\mathrm{Im}[\epsilon_r] = -81$ in this work, while they were $\mathrm{Re}[\epsilon_r] = -334$ and $\mathrm{Im}[\epsilon_r] = -4$ in [5]. There is an important difference between the values of $\mathrm{Im}[\epsilon_r]$ in the two cases: the great increase in the imaginary part of the permittivity (that translates in an increase in the losses of the antenna) is caused by the substantial change in the collision frequency that is much higher now and that indeed accounts for the dissipation processes inside the plasma.

As far as the plasma directors dimensions are concerned, we chose to change the diameter of the discharge from 2.5 mm to 3 mm since in real cases it is more easy to

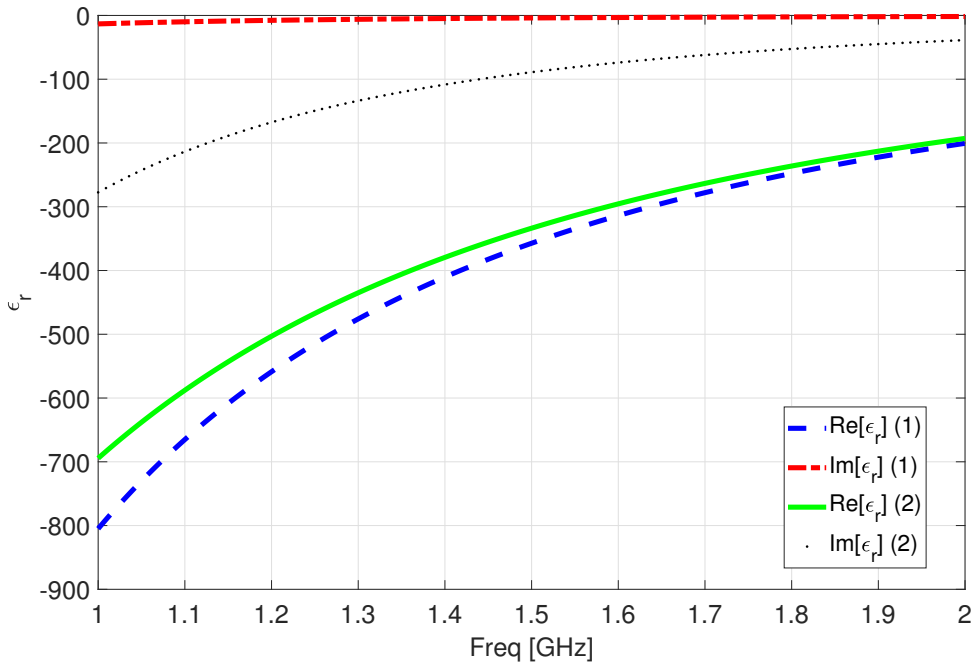

Figure 4.15: Comparison between the relative dielectric permittivity of the dispersive plasma in [4] (2) and in [5] (1): imaginary part (circles for [5], squares for [4]) and real part (downward triangle for [5], upward for [4]).

confine plasma in vessels with a larger diameter, and since 3 mm has proven to be a feasible dimension as it was proven by actually realizing such a plasma discharge.

Moreover the simulative model of the plasma directors includes now the dielectric vessels and the metallic electrodes used to generate the plasma in the CST simulations. The gaseous plasma is confined into a glass cylinder (pyrex material from CST library) of internal radius $r_{int} = r_{plasma} = 3$ mm and thickness of 0.6 mm: these values have been chosen according to real glass tubes that have been realized to confine the plasma in an experimental setup. Finally the glass cylinder is closed at the two extremities by two metallic electrodes of 1 mm thickness that resemble those used to generate the plasma by RF surface wave technique. A detail of the director designed in CST Microwave Studio is reported in Figure 4.16.

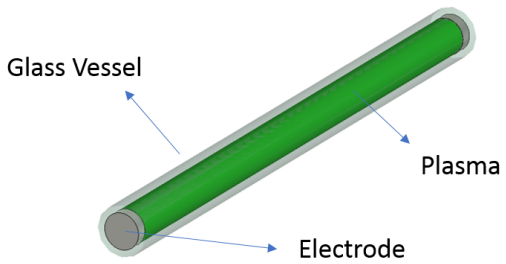

Figure 4.16: Design of the realistic plasma director in CST Microwave Studio.

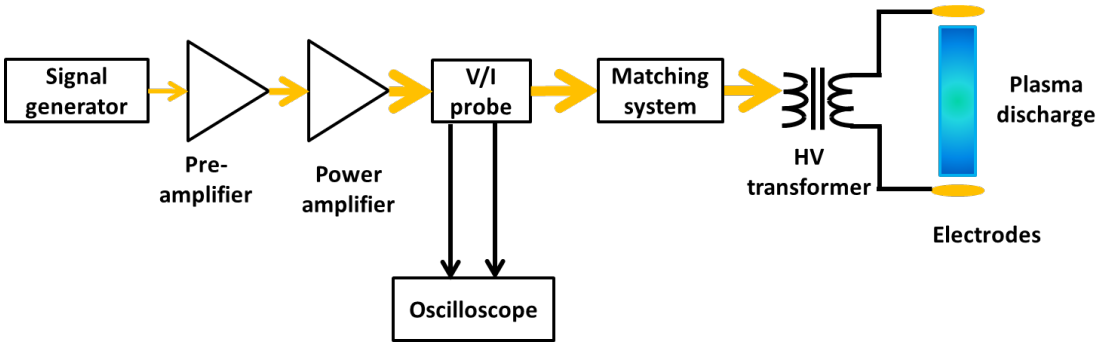

Figure 4.17: The scheme of the RF plasma generation system.

In order to optimize the properties of the Yagi-Uda antenna when the two discharges are used as directors, we increased of 4 mm the distance between the two directors (this value was obtained performing optimization through a parameter sweep in CST). The last thing to point out about the model of our antenna concerns the *off* state of the plasma directors: in [5] when one or both the plasma bars were un-energized, they have been simply excluded from the simulations; in this work instead, we included the glass cylinders and metal electrodes in the simulations, replacing the plasma cylinder with vacuum when the plasma is off.

The experimental setup of the plasma director

To realize the plasma directors, we have relied on a capacitive discharge [61] that has been driven by a 50 Ω Radio Frequency (RF) power source; the RF power has been fed in the $1.8 \div 15$ MHz range of frequencies through a matching network for efficient power transfer to the plasma, as illustrated in Figure 4.17. The signals are carried by means of RG-58 coaxial cables, while RF power is conveyed via RG-214 coaxial cables. The plasma has been generated by a couple of high voltage electrodes (see Figure 4.18) that have been placed internally at the far ends of the cylindrical pyrex vessel while being sealed with the prescribed argon gas atmosphere of 2 mbar. The pyrex vessel has an inner diameter of 3 mm, and an outer diameter of 4 mm; the two electrodes have been placed at a distance such that it is possible to realize a plasma column like the one identified in the antenna design phase.

To estimate the actual plasma density distribution within the plasma discharge, a microwave interferometer was used [67], which is capable of plasma density measurements regardless of the gas type; specifically, the plasma density value is related to the phase shift produced on a microwave signal traveling through the plasma. The instrument works in the 10^{16}-$7 \cdot 10^{19}$ m^{-3} range of plasma density values, is movable along the plasma source, and measures density in a plasma slab that is extended across the diameter of the source (see Figure 4.19). The plasma frequency value that was used in this work agrees with the measurements that were performed.

Results and Discussion

In this section the main results concerning the realistic metal plasma antenna are reported and compared with those obtained in [5] for its ideal counterpart. The results

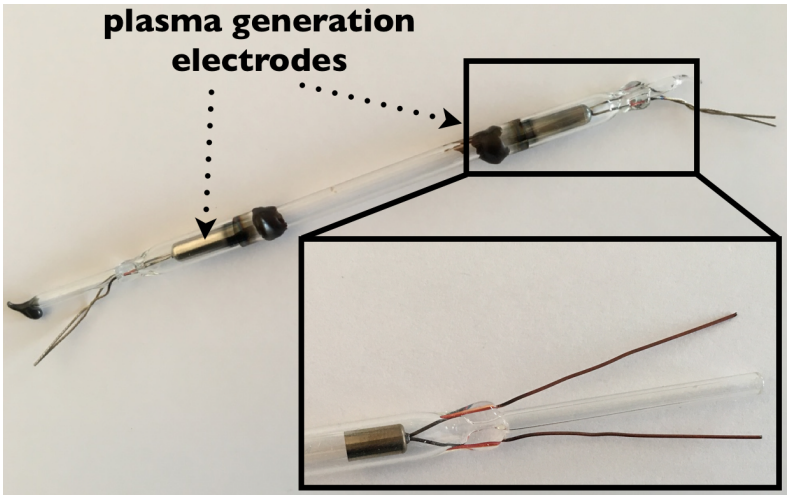

Figure 4.18: The experimental plasma discharge that has been used as director (Inset: the high voltage electrode).

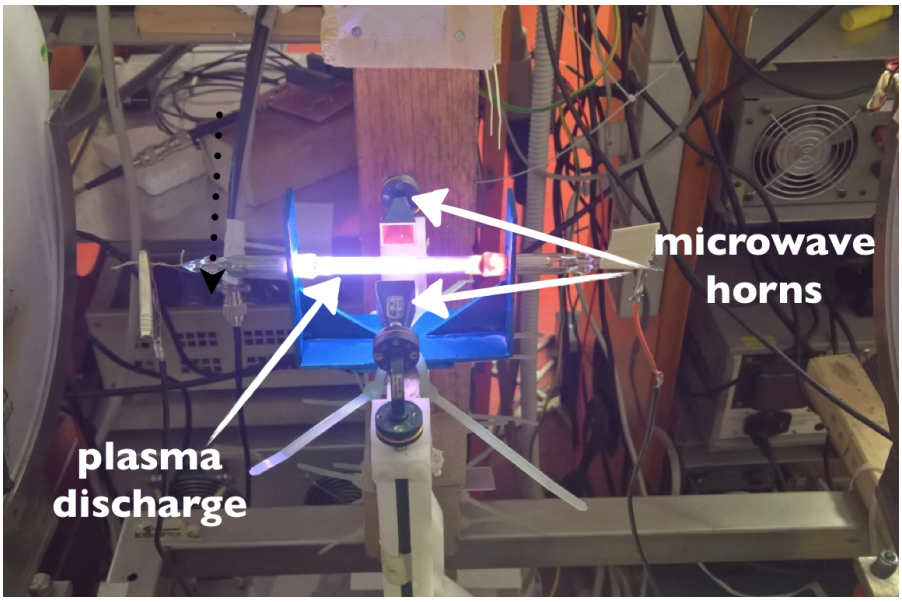

Figure 4.19: The experimental set-up with the plasma discharge between the two horns of the microwave interferometer for plasma density measurement.

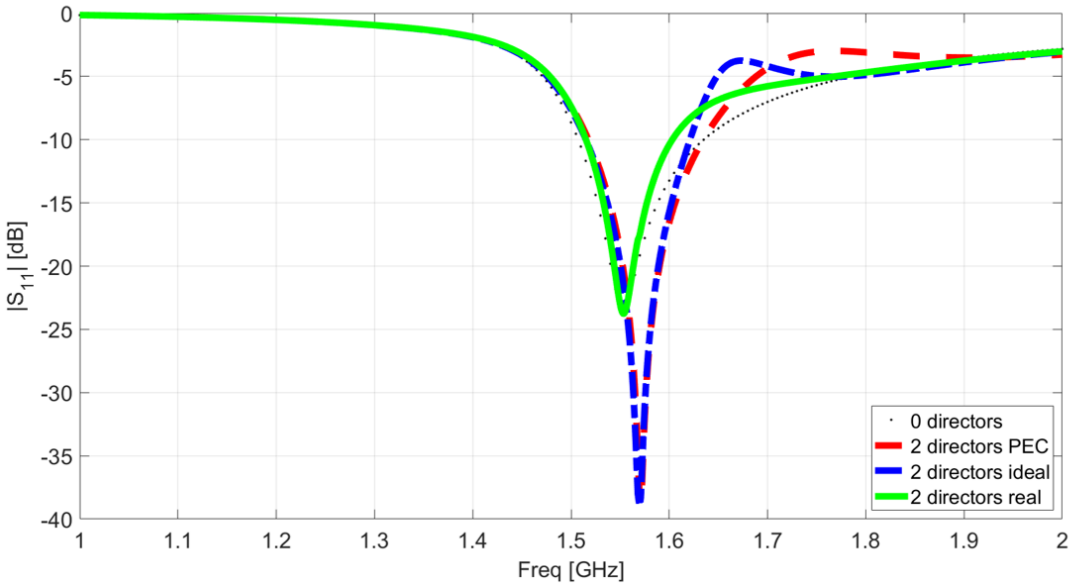

Figure 4.20: Reflection coefficient S_{11} for the Yagi-Uda antenna with: no directors (stars), two PEC directors (triangles), two ideal plasma directors (circles) and two realistic plasma directors (squares).

were obtained through full-wave numerical simulations in CST Microwave Studio. The analysis was carried out in the frequency range $1 \div 2$GHz and concerns mainly two metrics: (a) the reflection coefficient S_{11} and the input impedance; (b) the radiation properties of the antenna, i.e., farfield gain and efficiency and its reconfigurability.

As a first step, Figure 4.20 reports the magnitude of the reflection coefficient $|S_{11}|$ for the Yagi-Uda antenna with zero and two metal directors, for the hybrid Yagi-Uda with two ideal plasma directors [5] and for the antenna with the two realistic directors [4]. These three configurations were chosen as representative since they account for the starting condition, i.e., the antenna with no director that is designed to resonate at $f = 1.55$GHz, and the condition of maximum possible detuning for the antenna, i.e., when two directors are present; the other cases involving one director are omitted for ease of read of the graphs but are similar to and in perfect agreement with the results shown in the figure. As it can be seen, the reflection coefficient at the operating frequency is well below -15dB in all the three cases, thus confirming that the realistic plasma discharges that were conceived in this work do not detune the antenna.

In Figures 4.21, 4.22 the real and imaginary parts of the input impedance Z are reported again for the classic metal antenna, for the ideal hybrid Yagi-Uda and for the realistic hybrid antenna both with two directors. It can be seen how at the operation frequency $f = 1.55$GHz $\Im\{Z\}$ is almost zero for the three antennas, while $\Re\{Z\}$ changes: it is 45 Ω for the classic antenna and for the hybrid ideal one, while it is 43 Ω for the realistic one. It can be noticed however how also in the case in which a realistic discharge is considered the idea of using a metal dipole as the active element of the antenna proves to be a good solution in order to avoid the matching issues caused by the low input impedance of plasma antennas [68].

As far as the reconfigurability of the antenna is concerned, Figures 4.23, 4.24 depict the gain of the hybrid realistic Yagi-Uda antenna with zero, one and two directors in linear scale (for ease of read) in the *E*-plane (*xz*-plane) and *H*-plane (*xy*-plane) respectively. As stated above, when one or two directors are switched off, the vessel and electrodes have been included in the CST simulations and nonetheless we can see how reconfigurability with respect to the gain can still be achieved: the higher the number of *on* directors, the higher the gain.

Then we compared the gain of the realistic hybrid antenna both with its ideal counterpart [5] and with the classic metal antenna. Figures 4.25, 4.26 report the gain for the three antennas with one director switched on, on the E-plane and H-plane respectively: it can be seen how the gain of the antenna with the realistic plasma director is lower than those of the antenna with the ideal plasma director and than the one with the metal director (5.13 vs 6.02 and 6.25). Nonetheless the plot is in linear scale and therefore there is around 1 dB of difference between the maximum achievable gain in the three cases. The fact that the gain with the realistic plasma director is lower than in the case of the ideal one is reasonable considering that the collision frequency that accounts for the dissipation processes is considerably higher in the realistic case.

Figures 4.27, 4.28 report the same plot but this time with both the plasma directors on. Analogous considerations can be made as in the previous case: the gain for the realistic antenna is 5.6 that is lower than that of the ideal one (6.63) and of course lower than the one of the classic Yagi-Uda (7.1); but again, the values are in linear scale so the difference between the gain of the ideal and realistic hybrid antenna is less than 1 dB.

The last case concerns the antenna when both the directors are turned off: in the ideal case, the directors were excluded from simulations, while in the realistic case, the dielectric vessels and electrodes are included. The results are not reported graphically since the two radiation patterns are almost identical. This proves, as it was expected, that the main factor that influences the radiation pattern of the antenna is the plasma collision frequency, i.e., the parameter that accounts for the dissipative processes and that in this work is significantly higher than in [5].

As far as the efficiency is concerned, as expected this is lower in the realistic case in which losses are higher (this translates in a greater value of the collision frequency as commented previously): the efficiency is approximately 100% for the metal Yagi-Uda, 98% for the ideal hybrid Yagi-Uda and 80% for the realistic one.

4.4.3 Conclusions and Future Work

In [5] and [4] the study and design of a reconfigurable metal-plasma Yagi-Uda antenna for microwave applications has been presented: plasma discharges have been suitably designed to be used as directors of the antenna in order to achieve reconfigurability with respect to the gain. These plasma directors were designed starting from [5] and they were modified in order to resemble more realistic plasma discharges: the dielectric vessel and metallic electrodes were included in the model and moreover the dimensions and plasma parameters of the discharges were set according to experimental measurements of real plasma antennas.

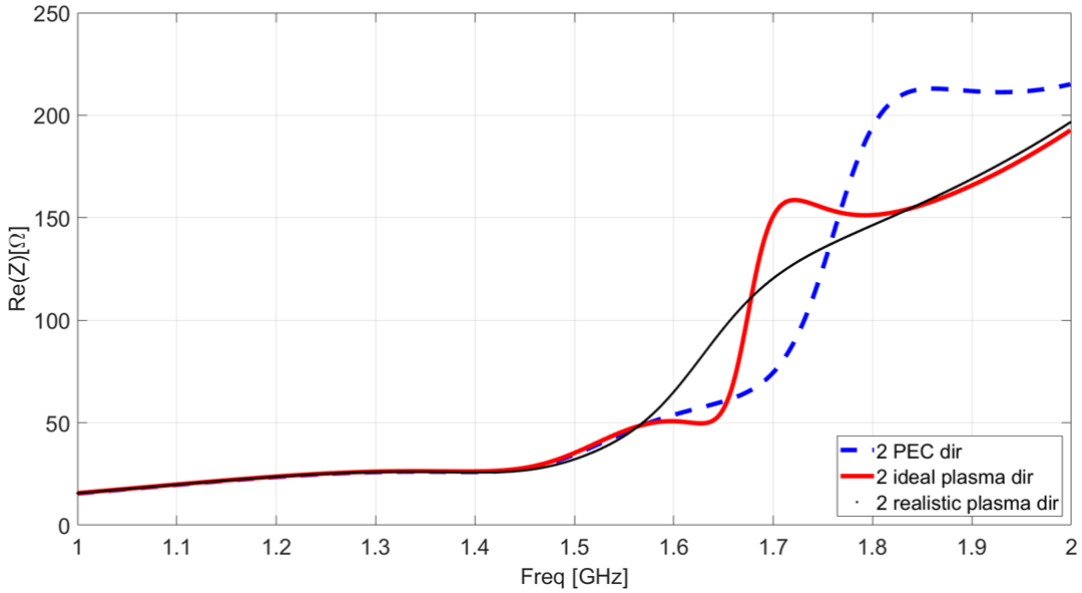

Figure 4.21: Real part of the input impedance of the Yagi-Uda antenna with: two PEC directors (triangles), two ideal plasma directors (circles) and two realistic plasma directors (squares).

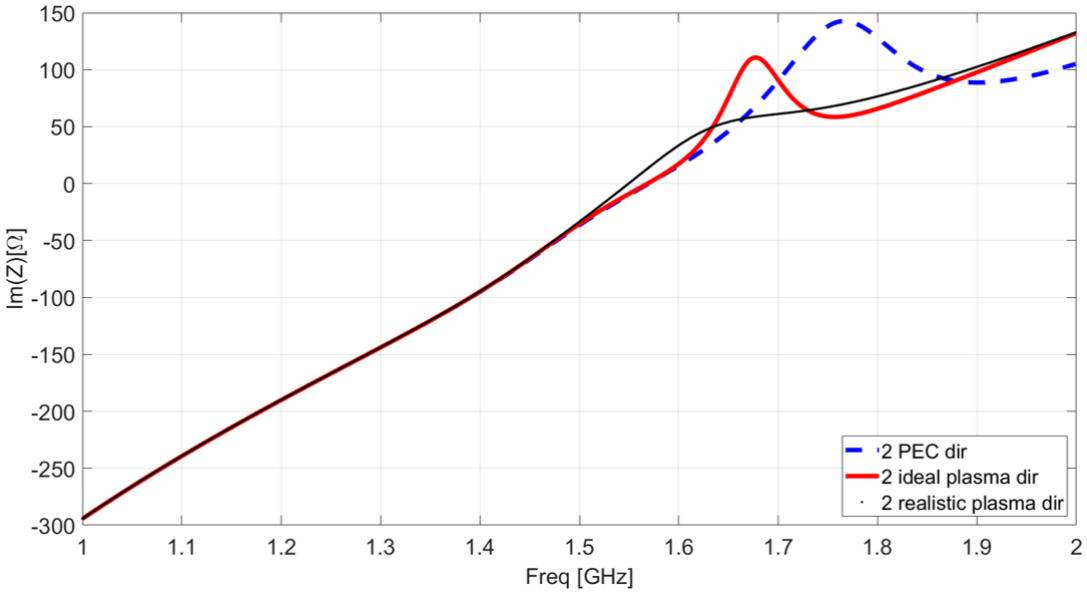

Figure 4.22: Imaginary part of the input impedance of the Yagi-Uda antenna with: two PEC directors (triangles), two ideal plasma directors (circles) and two realistic plasma directors (squares).

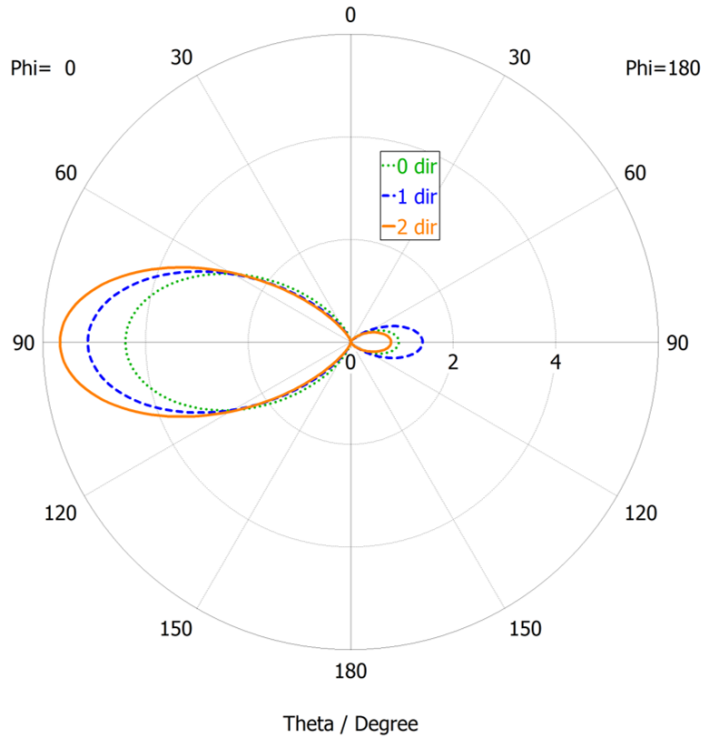

Figure 4.23: Farfield gain of the realistic hybrid antenna on the *E*-plane, i.e., *xz*-plane (see Figure 4.3 for coordinates system) with zero (dotted line), one (dashed line) and two directors (solid line).

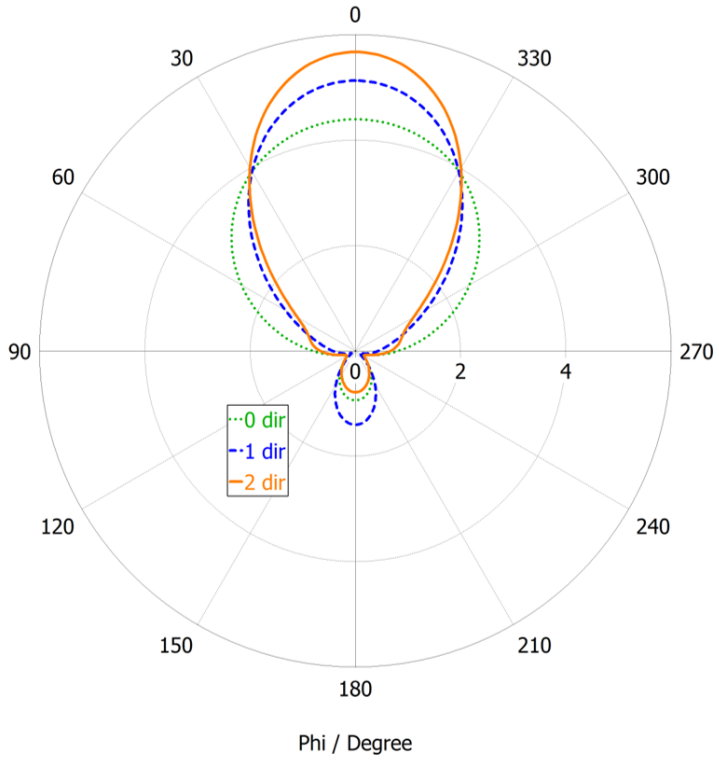

Figure 4.24: Farfield gain of the realistic hybrid antenna on the *H*-plane, i.e., *xy*-plane (see Figure 4.3 for coordinates system) with zero (dotted line), one (dashed line) and two directors (solid line).

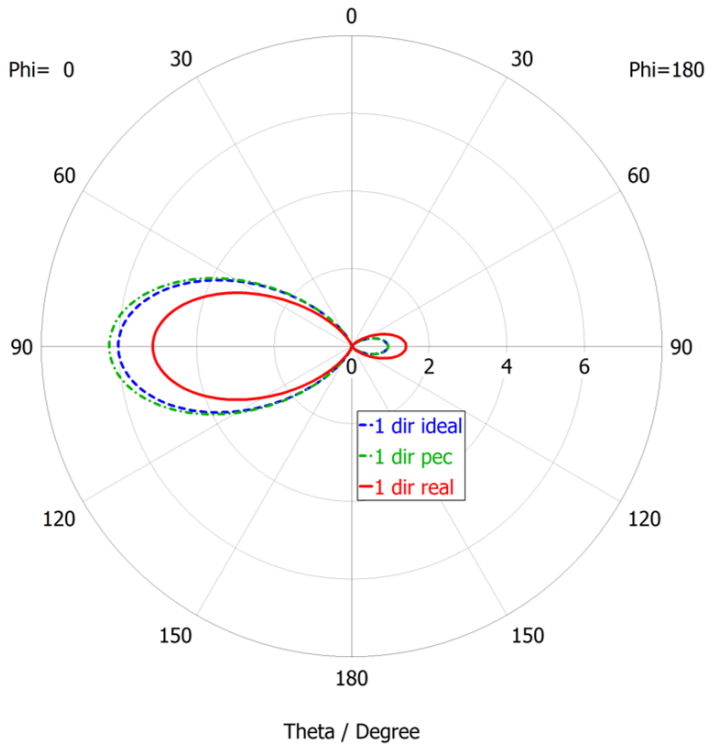

Figure 4.25: Farfield gain of the Yagi-Uda antenna on the *E*-plane, i.e., *xz*-plane (see Figure 4.3 for coordinates system) with: one PEC director, 1 ideal plasma director and 1 realistic plasma director of the realistic hybrid antenna.

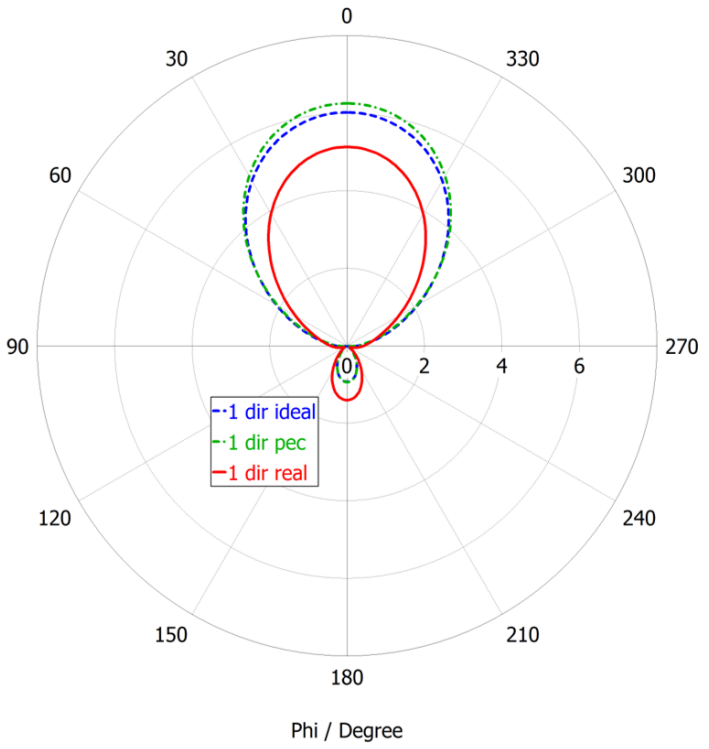

Figure 4.26: Farfield gain of the Yagi-Uda antenna on the *H*-plane, i.e., *xz*-plane (see Figure 4.3 for coordinates system) with: one PEC director, one ideal plasma director and one realistic plasma director of the realistic hybrid antenna.

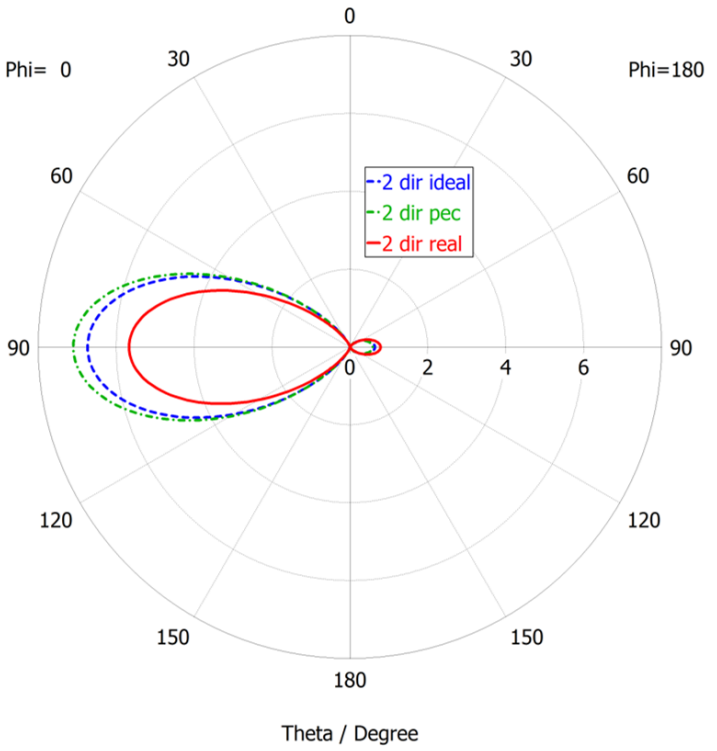

Figure 4.27: Farfield gain of the Yagi-Uda antenna on the *E*-plane, i.e., *xz*-plane (see Figure 4.3 for coordinates system) with: two PEC directors, two ideal plasma director and two realistic plasma directors of the realistic hybrid antenna.

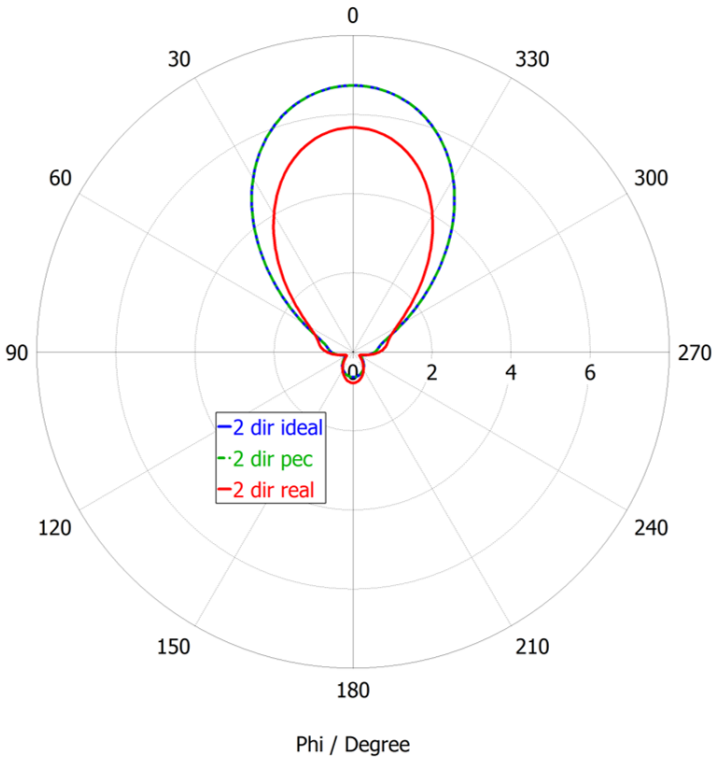

Figure 4.28: Farfield gain of the Yagi-Uda antenna on the *H*-plane, i.e., *xz*-plane (see Figure 4.3 for coordinates system) with: two PEC directors, two ideal plasma director and two realistic plasma directors of the realistic hybrid antenna.

It has been shown that the performance of the antenna are very good as compared to [5]. Moreover it is clear from the results that reconfigurability with respect to the gain can still be achieved even with realistic plasma discharges used as directors. Of course, the radiation pattern is affected by the considerably higher value of the collision frequency, i.e., by the fact that dissipative processes are stronger in this case.

As a future step, we aim at considering plasma discharges with a non-uniform density, i.e., a density that changes axially along the cylindrical vessel and that resembles even better the behavior of a realistic plasma discharge.

Therefore this study paves the way to the actual realization of the conceived hybrid metal-plasma Yagi-Uda antenna. However, it must be pointed out that, in order to characterize and measure our proposed antenna not only in terms of its reflection coefficient but also in terms of its radiation pattern, there are still some issues to face, mainly related to the rather complicated setup that is needed to ignite and sustain the plasma inside the two directors.

4.5 Crossed Plasma Dipole for Satellite Communications

Among the different possible applications of plasma antennas, satellite communication (SatCom) is among the most promising ones. This is the object of a collaboration between the department of information engineering of the University of Padova and CISAS B. Colombo (an aerospace research center of the University of Padova) that aims at performing fundamental research to improve plasma technology performances. The final goal is to design and develop a new generation of space-born antennas and in particular:

1. to perform a feasibility study of a L band ($1-2$ GHz) antenna based on plasma elements targeting navigation and interlink-satellite communication;
2. to identify system requirements and specifications, and expected performances;
3. to strongly improve plasma technology to be used in plasma antenna arrays;
4. to design and develop a technology demonstrator of the most promising plasma application.

As part of this project, our research group has started working on the numerical simulations of a crossed plasma dipole. The remaining part of this chapter reports the preliminary simulative results obtained for this geometry and it is organized as follows: first the requirements for a SatCom antenna are presented, then the basic features of an active plasma dipole are introduced in order to understand the design of a plasma crossed dipole and finally the simulative results obtained in CST for the plasma crossed dipole are reported.

4.5.1 Introduction and Antenna Requirements

Satellite communications (SatCom) play a vital role in the global telecommunications system, which is based on thousands of artificial satellites that orbit Earth, and rely analog and digital signals that carry voice, video, and data to and from many locations

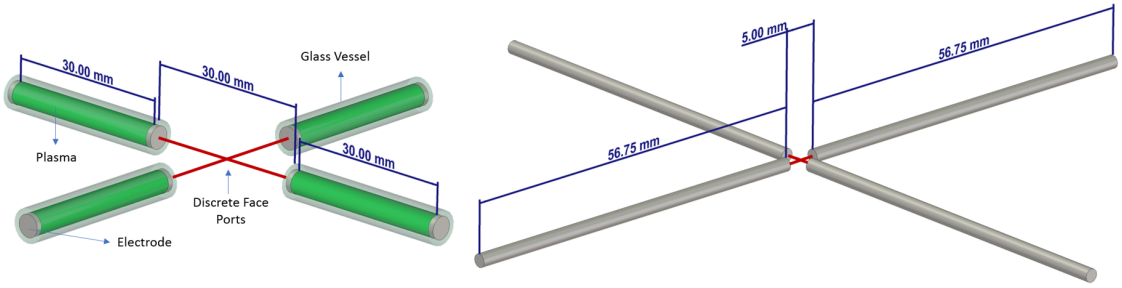

Figure 4.29: CST model of a crossed plasma dipole that includes electrodes and glass vessels and that operates at 1.17 GHZ (on the left) and its metallic counterpart working as well at 1.16 GHz (on the right).

worldwide. A SatCom system comprises a ground segment, which features either fixed or mobile transmission and reception, and a space segment, which is basically the satellite. Navigation systems (i.e., systems that provide geolocation and time information) as for example the European Galileo, require improvements on the navigation antennas: this is confirmed by the growing demand to identify and implement antennas that can enhance the capability of the constellation by ensuring more robust GPS service especially in GPS-denied environments or in regions where service is inconsistent.

In order to design a suitable innovative GPS antenna, it is fundamental to understand the main requirements that such an antenna must meet. The two main specifications are to cover the L frequency band and to use Circular Polarization (CP). This second requirement is mainly justified by two reasons:

1. changing relative orientation of a circularly polarized antenna does not cause polarization fading as it is the case of linear polarization;

2. circular polarization does not suffer from Faraday rotation.

For these reasons, two popular choice for GPS antennas are array of helix and patch antennas [69]. Moreover, a GPS antenna should be broadband covering the whole frequency range, since multiband antennas usually present stronger radiation pattern asymmetry and lower polarization purity.

So far we have been involved in a feasibility study of a plasma antenna element capable to radiate a circularly polarized signal in a frequency range roughly between 1-2 GHz. A possible solution to obtain circular polarization is to use the plasma equivalent of the well-known metallic *Crossed Dipole antenna* (also known as *Turnstile antenna*): as it can be seen from Figure 4.29, this antenna consists of two plasma dipoles mounted at right angles with respect to each other and fed through currents that are $90°$ out-of-phase. The picture depicts also its metallic counterpart: both antennas work at 1.17 GHz and it can be observed how the four arms of the plasma Turnstile antenna are almost half the length of the metallic ones as expected since the plasma effective wavelength is much shorter than the free space one (see Section 4.3).

In this section the preliminary results concerning this antenna obtained through full-wave numerical simulations are presented: first those concerning a single plasma

dipole (i.e., the basic element of the crossed dipole antenna) are presented, then the crossed dipole antenna is introduced and finally the effects of the plasma parameters on the antenna parameters are described.

4.5.2 Active Plasma Dipole Antenna

As a first step, a single plasma dipole antenna has been designed and simulated in CST Microwave Studio: this antenna represents the basic element of the crossed dipole antenna that is presented afterwards. It consists of just one of the two dipoles depicted in Figure 4.29: this comprises two 1 mm-thick cylindrical glass vessels with a diameter of 4 mm, two 1 mm-thick cylindrical metallic electrodes at the extremities of each vessel and two cylinders of plasma material inside the two vessels (represented in green). The two arms of the dipole are 30 mm long and they are separated by a gap of 30 mm inside which a 50 Ω discrete face port is placed to feed the antenna.

The plasma material has been modeled as a Drude material as presented in Section 4.3. In this specific case, the plasma frequency is $\omega_p = 170$ GHz (with plasma density in the order of 10^{19} m^{-3}) and the collision frequency is $\nu = 3.71$ GHz (with a neutral gas pressure of approximately 1.5 mbar).

Figures 4.30-4.32 report in order the imaginary and real part of the input impedance and the magnitude of the reflection coefficient for both the plasma dipole and the classic dipole. It can be seen that the resonance frequency, i.e., the frequency at which the imaginary part of the input impedance is zero, is approximately 1.17 GHz for both dipoles, and at this frequency the real part of the input impedance is 92.76 Ω for the plasma dipole and 72 Ω for the metallic dipole. Figure 4.33 depicts the directivity of the plasma and metallic dipoles at the resonance frequency in logarithmic scale: it can be seen that the shape of the radiation pattern is the same in both cases even if for the plasma dipole, the maximum is slightly lower than for its metallic counterpart (2.02 dB vs. 2.12 dB). As a final remark, it is worth mentioning that the total efficiency of the plasma antenna is considerably lower than the one of the metallic dipole, i.e., 61% vs. 98%.

4.5.3 Crossed Plasma Dipole

A crossed plasma dipole has been designed in CST Microwave Studio exploiting the design of the single plasma dipole presented above. As it can be seen from Figure 4.29, the antenna consists of two plasma dipoles placed orthogonally with respect to each other. Each dipole comprises two glass cylinders closed by metallic electrodes: the cylinders have a length of 30 mm, a diameter of 4 mm and a thickness of 1 mm and the electrodes are 1 mm thick as well. The two halves of the dipoles are separated by a gap of 30 mm into which a 50 Ω discrete face port is placed in order to feed the antennas. Figure 4.29 depicts also the metallic equivalent of the plasma crossed dipole, i.e., a classic Turnstile antenna resonating at 1.17 GHz: it can be noted how the arms of this antenna are considerably larger than the plasma ones as it is expected since the effective wavelength in the plasma is much shorter than the one in free space.

As far as the plasma material is concerned, this has been modeled in the exact same way as it was done for the single plasma dipole, and also the plasma frequency and

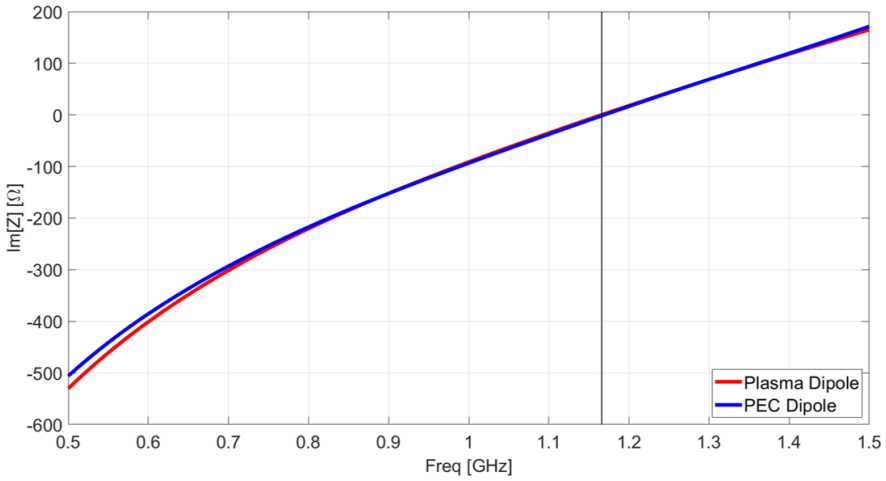

Figure 4.30: Imaginary part of the input impedance of the active plasma (red) and PEC (blue) dipoles: the black vertical line at 1.17 GHz indicates the resonance frequency, i.e., the frequency at which the imaginary part of Z is zero.

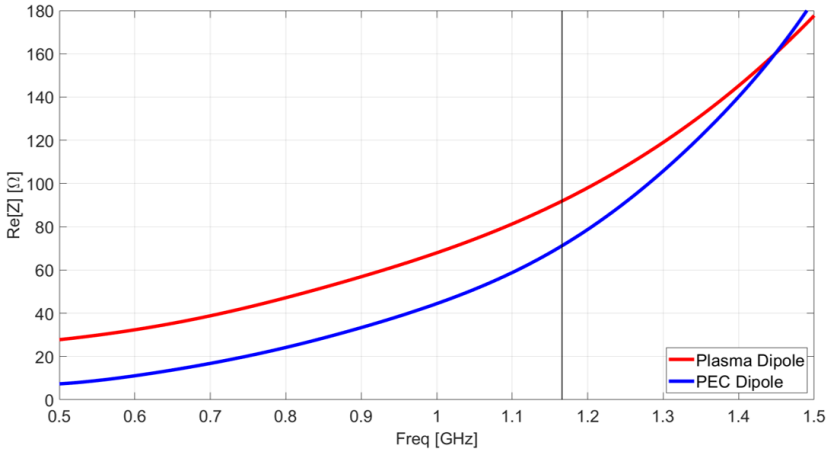

Figure 4.31: Real part of the input impedance of the active plasma (red) and PEC (blue) dipoles: at the resonance frequency (black vertical line at 1.17 GHz) Re[Z]=92 Ω.

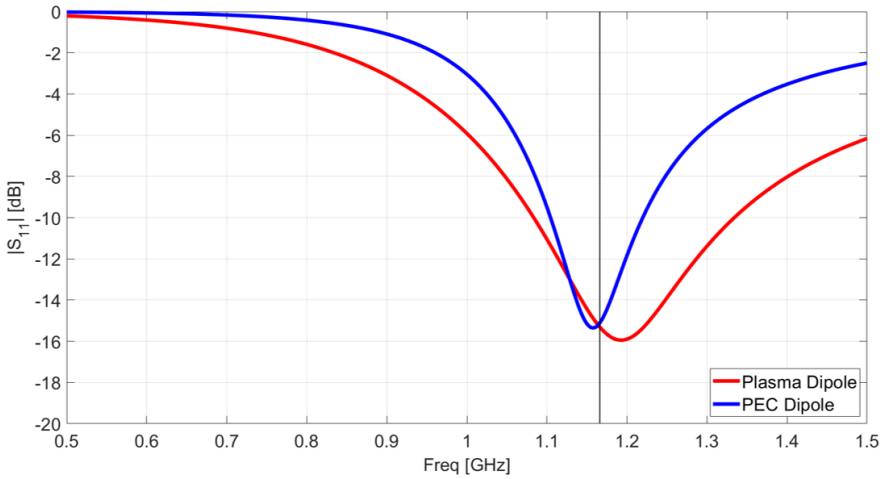

Figure 4.32: Reflection coefficient (magnitude) of the active plasma (red) and PEC (blue) dipoles: the black vertical line at 1.17 GHz indicates the resonance frequency.

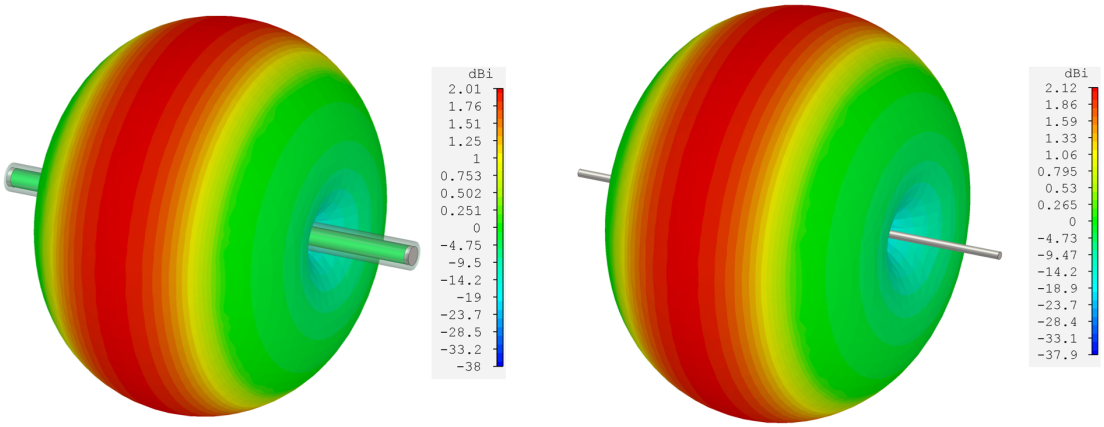

Figure 4.33: Directivity of the plasma and pec dipole in logarithmic scale at the resonant frequency of 1.17 GHz.

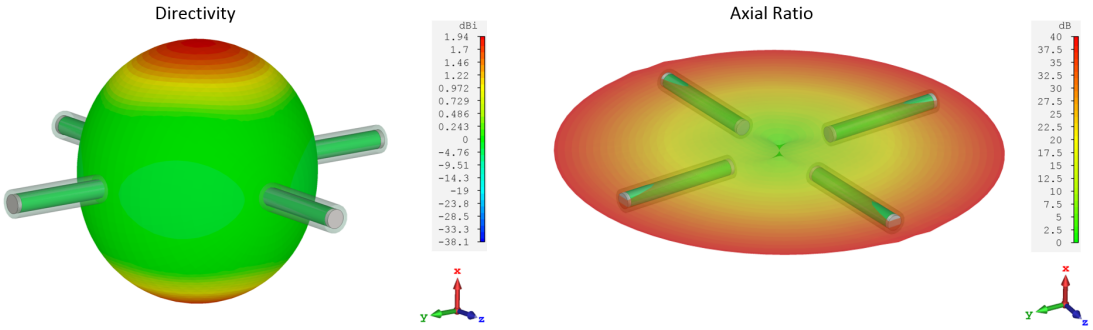

Figure 4.34: Directivity (on the left) and axial ratio (on the right) of the plasma crossed dipole (logarithmic scale) when the two dipoles are fed by 90° out-of-phase currents.

collision frequency are the same. The impedance is equal to the one of the single plasma dipole and therefore the resonance frequency is again 1.17 GHz.

The two dipoles are fed by currents that are 90° out-of-phase and the resulting three dimensional farfield and axial ratio plots are reported in Figure 4.34. It can be seen how the radiation pattern of the crossed plasma dipole is the same as the one of its metallic counterpart; moreover from the axial ratio plot it is clear that CP is achieved.

The gap between the two halves of each dipole was then changed to different values, namely 10, 15, 20 and 25 mm: the resonance frequency shifts up as the gap reduces, while the real part of the input impedance at the resonance frequency for each gap value does not change significantly as it is shown in Figures 4.35, 4.36. Figure 4.37 reports the magnitude of the reflection coefficient: as it is expected the lowest peak shifts up as the gap reduces.

4.5.4 Effect of the Plasma Parameters on the Antenna Parameters

As a final step, the analysis of the behavior of the antenna parameters (input impedance, reflection coefficient, axial ratio and farfield) with respect to the plasma parameters (plasma frequency and collision frequency) is presented.

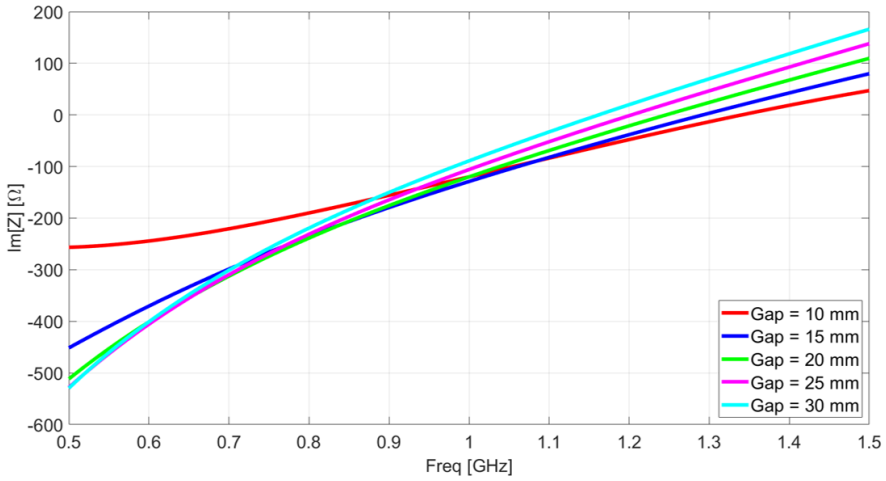

Figure 4.35: Imaginary part of the input impedance of the active plasma dipole for different values of the gap between its two arms (see Figure 4.29 for the design).

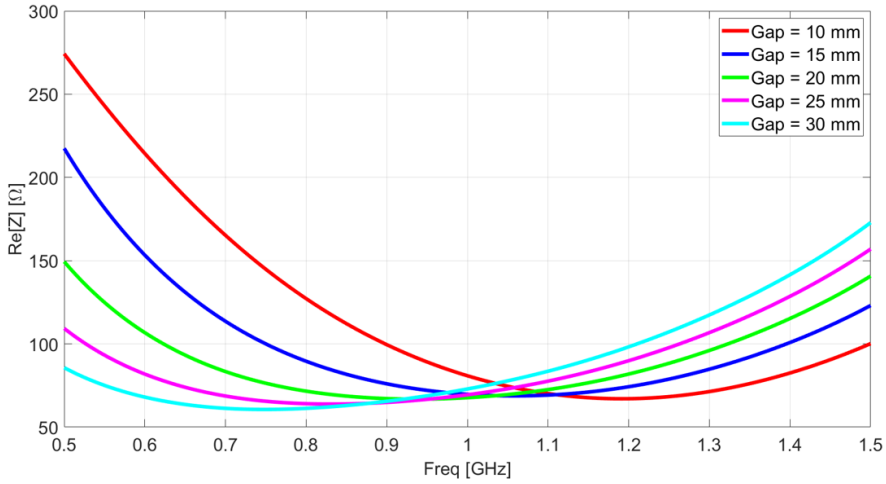

Figure 4.36: Real part of the input impedance of the active plasma dipole for different values of the gap between its two arms (see Figure 4.29 for the design).

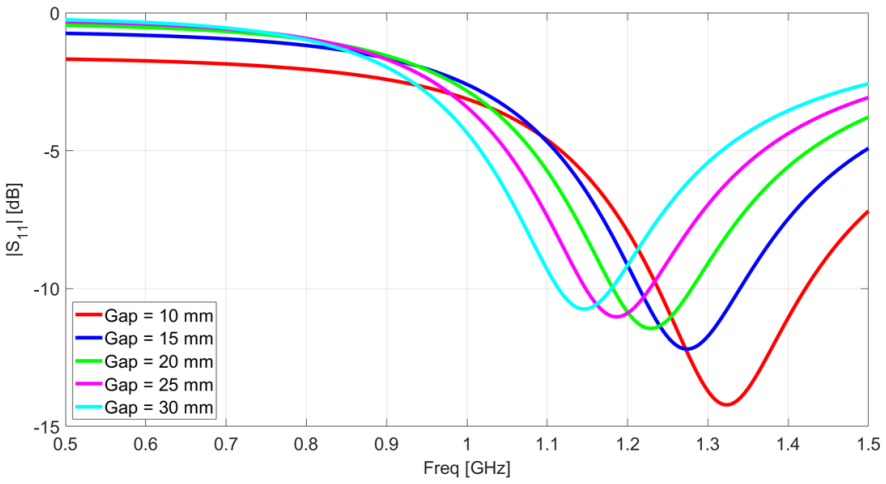

Figure 4.37: Reflection coefficient (magnitude) of the active plasma dipole for different values of the gap between its two arms (see Figure 4.29 for the design).

Figures 4.38, 4.39 depict the changes in the real and imaginary part of the input impedance when the collision frequency is set to 3.71 GHz (with a neutral gas pressure of approximately 1.5 mbar) and the plasma frequency varies from 100 GHz up to 170 GHz (with plasma density in the range $4 \times 10^{18}\ m^{-3} - 10^{19}\ m^{-3}$). It can be seen how, as the plasma frequency increases, both the resonance frequency and the input impedance at the resonance frequency increase.

Moreover, the frequency at which the magnitude of the reflection coefficient is minimum shifts up as the plasma frequency increases as it is depicted in Figure 4.40. As far as the axial ratio and the farfield are concerned instead, no significant change is detected when the plasma frequency is varied.

Two different values of collision frequency have been analyzed, namely 3.70 and 3.73 GHz, while keeping the plasma frequency fixed to 170 GHz. No significant change in the resonance frequency and input impedance has been detected: the resonance frequency is 1.17 GHz in both cases while the input impedance is 92.87Ω and 92.66Ω when the collision frequency is 3.70 and 3.73 GHz respectively.

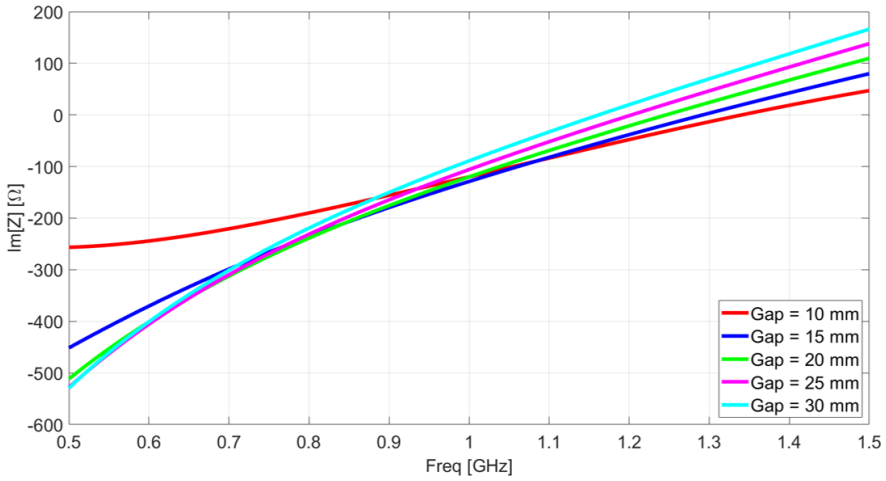

Figure 4.38: Imaginary part of the input impedance of the active plasma dipole for different values of the plasma frequency ω_p.

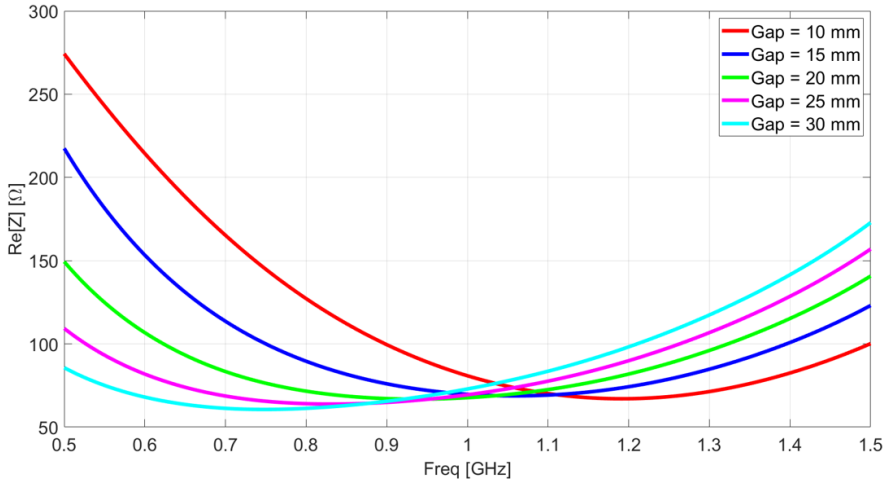

Figure 4.39: Real part of the input impedance of the active plasma dipole for different values of the plasma frequency ω_p.

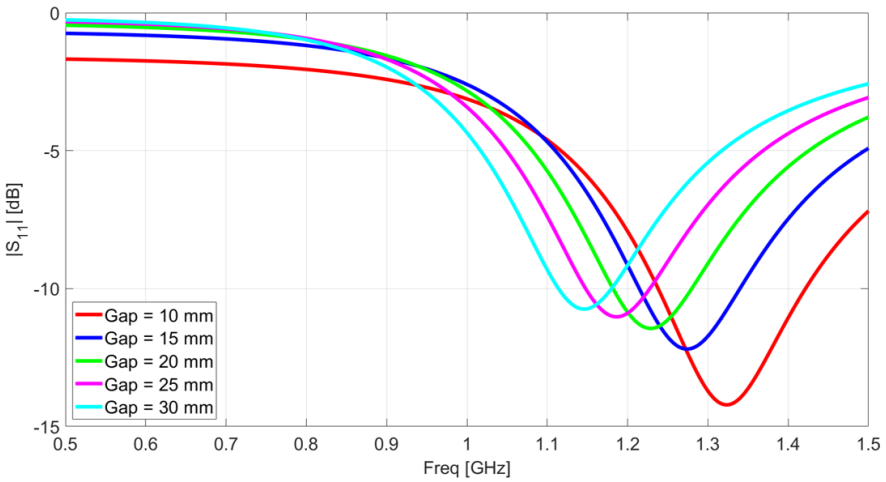

Figure 4.40: Reflection coefficient (magnitude) of the active plasma dipole for different values of the plasma frequency ω_p.

Chapter 5

Conclusions

This thesis reports the main results obtained in the three research topics that were the subject of my Ph.D.: self-adapting phased array antennas, microwave devices for skin cancer detection, and gaseous plasma antennas. For each of these three topics an original contribution was given.

As far as phased array antennas for changing surfaces are concerned, the projection method effectiveness and limitations when applied to complex changing arrays were investigated. Moreover a novel and simpler version of this method was provided and validated through simulations and measurements. To conclude, the projection method proves to be effective in retrieving the pattern of an array, but its performance are limited to the region around the main lobe of the array. Thus, this technique is a suitable solution for cheap and simple devices whose main requirement is to have an overall low cost.

Regarding skin cancer detection, a novel substrate integrated waveguide probe was presented: the probe overcomes the limitations of other probes that can be found in literature, providing a cheap easy-to-use and effective tool for early-stage skin cancer diagnosis. As a future step, the device should be tested on real skin tissues. Another interesting improvement to the work would be to fabricate a more realistic multi-layer skin phantom in which a very small tumor can be placed.

As far as gaseous plasma antennas are concerned, the designs of different active antennas were presented. These pave the way to novel antenna architecture that could be exploited for satellite communications. In the future we plan on fabricating and testing some of these antennas together with CISAS B. Colombo.

List of Publications

International Journals

1. G. Mansutti, F. Rigobello, S. M. Asif, M. S. Khan, A.-D. Capobianco, and A. Galtarossa, "Main lobe control of a beam tilting antenna array laid on a deformable surface", International Journal of Antennas and Propagation, 19 April 2018.

2. G. Mansutti, S. Khan, A. Capobianco, A. Iftikhar, and S. Asif, "Self-adapting conformal phased-array antennas for complex changing surfaces," Microwave and Optical Technology Letters, vol. 59, no. 2, pp. 393-399, Feb. 2017.

3. G. Mansutti, D. Melazzi, A. Capobianco, "A reconfigurable metal-plasma Yagi-Uda antenna for microwave applications," Advances in Science Technology and Engineering Systems Journal (ASTESJ), vol. 2, no. 3, pp. 441–448, 2017.

4. F. Rigobello, G. Mansutti, M. S. Khan, S. Asif, A.-D. Capobianco, and A. Galtarossa, "Robustness of the Projection Method for an Asymmetrically Deformed Planar Antenna Array", Microwave and Optical Technology Letters. [Accepted August 2018]

Conference Proceedings

1. G. Mansutti, A.-T. Mobashsher, A. M. Abbosh, "Millimeter-wave substrate integrated waveguide probe for near-field skin cancer detection," 3rd Australian Microwave Symposium (AMS), Brisbane, Australia, February 2018.

2. G. Mansutti, A.-T. Mobashsher, A. M. Abbosh, "Conformal array-based directional antenna system for biomedical applications," 3rd Australian Microwave Symposium (AMS), Brisbane, Australia, February 2018.

3. F. Rigobello, G. Mansutti, A.-D. Capobianco, and A. Galtarossa, "Phase Sensitivity of the Projection Method for a Beam Tilting Deformed Array," European Conference on Antennas and Propagation (EuCAP), London, 2018.

4. G. Mansutti, F. Rigobello, S. Khan, and A. Capobianco, "Pattern recovery of a beam-tilting phased array antenna on a doubly wedge-deformed surface," European Microwave Conference (EuMC), Nuremberg, Ger., 2017.

5. F. Rigobello, G. Mansutti, S. Khan, and A. Capobianco, "Pattern recovering of conformal antenna array for strongly deformed surfaces," European Conference on Antennas and Propagation (EuCAP), Paris, 2017.

6. G. Mansutti, D. Melazzi, A.-D. Capobianco, "Hybrid metal-plasma Yagi-Uda antenna for microwave applications," European Microwave Conference (EuMC), London, 2016.

Awards

IEEE Best student paper award for the work "Millimeter-wave substrate integrated waveguide probe for near-field skin cancer detection" by G. Mansutti, A.-T. Mobashsher, and A. M. Abbosh, presented at the 3rd Australian Microwave Symposium (AMS), Brisbane, Australia, February 2018.

Bibliography

[1] K. Chopra, D. Calva *et al.*, "A comprehensive examination of topographic thickness of skin in the human face," *Aesthetic Surgery Journal*, vol. 35, no. 8, pp. 1007–1013, 2015.

[2] F. Topfer and J. Oberhammer, "Millimeter-wave tissue diagnosis: The most promising fields for medical applications," *IEEE Microwave Magazine*, vol. 16, no. 4, pp. 97–113, 2015.

[3] Y. Lee and K. Hwang, "Skin thickness of Korean adults," *Surgical and Radiologic Anatomy*, vol. 24, no. 3-4, pp. 183–189, 2002.

[4] G. Mansutti, D. Melazzi, and A.-d. Capobianco, "A Reconfigurable Metal-Plasma Yagi-Yuda Antenna for Microwave Applications," *Advances in Science, Technology and Engineering Systems Journal*, vol. 2, no. 3, pp. 441–448, 2017. [Online]. Available: http://astesj.com/v02/i03/p57/

[5] G. Mansutti, D. Melazzi, and A. D. Capobianco, "Hybrid metal-plasma Yagi-Uda antenna for microwave applications," *European Microwave Week 2016: "Microwaves Everywhere", EuMW 2016 - Conference Proceedings; 46th European Microwave Conference, EuMC 2016*, pp. 727–730, 2016.

[6] Samsung, "Samsung 5G Vision," 2018. [Online]. Available: https://www.samsung.com/global/business/networks/insights/5g/

[7] Nokia, "Unleashing the Potential of 5G," 2018. [Online]. Available: https://networks.nokia.com/5g

[8] P. Salonen, Y. Rahmat-Samii *et al.*, "Dual-band wearable textile antenna," *IEEE Antennas and Propagation Society Symposium, 2004.*, vol. 1, pp. 463–466, 2004.

[9] M. Klemm and G. Troester, "Textile UWB Antennas for Wireless Body Area Networks," *IEEE Transactions on Antennas and Propagation*, vol. 54, no. 11, pp. 3192–3197, 2006.

[10] L. A. Yimdjo Poffelie, P. J. Soh *et al.*, "A High-Fidelity All-Textile UWB Antenna with Low Back Radiation for Off-Body WBAN Applications," *IEEE Transactions on Antennas and Propagation*, vol. 64, no. 2, pp. 757–760, 2016.

[11] H. Schippers, J. H. Van Tongeren *et al.*, "Vibrating antennas and compensation techniques Research in NATO/RTO/SET 087/RTG 50," *IEEE Aerospace Conference Proceedings*, 2007.

[12] H. Schippers, J. Verpoorte *et al.*, "Conformal phased array with beam forming for airborne satellite communication," *2008 International ITG Workshop on Smart Antennas, WSA 2008*, pp. 343–350, 2008.

[13] B. D. Braaten, S. Roy *et al.*, "A self-adapting flexible (SELFLEX) antenna array for changing conformal surface applications," *IEEE Transactions on Antennas and Propagation*, vol. 61, no. 2, pp. 655–665, 2013.

[14] M. S. Khan, B. Ijaz *et al.*, "Frequency reconfigurable self-adapting conformal array for changing surfaces," *IET Microwaves, Antennas & Propagation*, vol. 10, no. 8, pp. 897–901, 2016. [Online]. Available: http://digital-library.theiet.org/content/journals/10.1049/iet-map.2015.0622

[15] B. Ijaz, A. Sanyal *et al.*, "Gain limits of phase compensated conformal antenna arrays on non-conducting spherical surfaces using the projection method," *IEEE International Conference on Wireless for Space and Extreme Environments, WiSEE 2013 - Conference Proceedings*, pp. 1–6, 2013.

[16] S. Nariyal, I. Ullah *et al.*, "On the use of amplitude tapering for pattern correction of conformal (Curved) antennas," *IEEE International Conference on Wireless for Space and Extreme Environments, WiSEE 2013 - Conference Proceedings*, pp. 1–2, 2013.

[17] B. D. Braaten, S. Roy *et al.*, "Phase-compensated conformal antennas for changing spherical surfaces," *IEEE Transactions on Antennas and Propagation*, vol. 62, no. 4, pp. 1880–1887, 2014.

[18] B. D. Braaten, S. Roy *et al.*, "An Autonomous Self-Adapting Conformal Array for Cylindrical Surfaces with a Changing Radius," *2014 IEEE Antennas and Propagation Society International Symposium (APSURSI)*, vol. 2, no. 1, pp. 1784–1785, 2014.

[19] B. D. Braaten, I. Ullah *et al.*, "Scanning characteristics of a self-adapting phased-array antenna on a wedge-shaped conformal surface," *IEEE Antennas and Propagation Society, AP-S International Symposium (Digest)*, no. 2, pp. 1220–1221, 2013.

[20] I. Ullah and B. D. Braaten, "Nulls of a Conformal Beamforming Array on an Arbitrary Wedge-Shaped Surface," *IEEE Antennas and Propagation Society, AP-S International Symposium (Digest)*, no. 1, pp. 1790–1791, 2014.

[21] G. Mansutti, S. M. Khan *et al.*, "Self-adapting conformal phased array antennas for complex changing surfaces," *Microwave and Optical Technology Letters*, vol. 59, no. 2, pp. 393–399, 2017.

[22] R. L. Haupt, *Antenna Arrays: A Computational Approach*. John Wiley and Sons, Ltd., Hoboken, New Jersey, 2010.

[23] F. Rigobello, G. Mansutti *et al.*, "Pattern recovering of conformal antenna array for strongly deformed surfaces," in *2017 11th European Conference on Antennas and Propagation, EUCAP 2017*, 2017.

[24] C. A. Balanis, *Antenna Theory: Analysis and Design (3rd edition)*. Wiley, 2005.

[25] G. Mansutti, F. Rigobello *et al.*, "Main Lobe Control of a Beam Tilting Antenna Array Laid on a Deformable Surface," *International Journal of Antennas and Propagation (IJAP)*, vol. 2018, pp. 1–6, 2018.

[26] Australian Bureau of Statistics, "3303.0 - Causes of Death, Australia, 2016," 2017. [Online]. Available: http://www.abs.gov.au/ausstats/abs@.nsf/mf/3303.0

[27] American Cancer Society, "Cancer Facts and Figures 2018," 2018.

[28] M. P. Staples, M. Elwood *et al.*, "Non-melanoma skin cancer in Australia: the 2002 national survey and trends since 1985," *The Medical Journal of Australia (MJA)*, vol. 184, no. 1, pp. 6–10, 2006.

[29] R. S. Stern, "Prevalence of a history of skin cancer in 2007: Results of an incidence-based model," *Archives of Dermatology*, vol. 146, no. 3, pp. 279–282, 2010.

[30] AIRT Working Group, "Italian cancer figures—report 2006. Incidence, mortality and estimates," *Epidemiologia & Prevenzione*, vol. 30, no. 1, pp. 18–22, 2006.

[31] Australian Institute of Health and Welfare, "Cancer in Australia: an Overview 2014. Cancer series No 90. Cat. no. CAN 88." Tech. Rep., 2014.

[32] A. Breslow, "Thickness, cross-sectional areas and depth of invasion in the prognosis of cutaneous melanoma." *Annals of surgery*, vol. 172, no. 5, pp. 902–908, 1970.

[33] A. M. Noone, N. Howlader *et al.*, "SEER Cancer Statistics Review, 1975-2015," p. based on November 2017 SEER data submission, 2018. [Online]. Available: https://seer.cancer.gov/csr/1975{_}2015/

[34] A. C. Morton and R. M. Mackie, "Clinical accuracy of the diagnosis of cutaneous malignant melanoma," *British Journal of Dermatology*, vol. 138, no. 2, pp. 283–287, 1998. [Online]. Available: http://doi.wiley.com/10.1046/j.1365-2133.1998.02075.x

[35] V. Suntzeff and C. Carruthers, "The Water Content in the Epidermis of Mice Undergoing Carcinogenesis by Methylcholanthrene," *Cancer Research*, vol. 6, no. 10, pp. 574–577, 1946.

[36] C. M. Balch, J. E. Gershenwald *et al.*, "Final version of 2009 AJCC melanoma staging and classification," *Journal of Clinical Oncology*, vol. 27, no. 36, pp. 6199–6206, 2009.

[37] D. E. Elder, "Melanoma progression," *Pathology*, vol. 48, no. 2, pp. 147–154, 2016.

[38] E. L. Psaty and A. C. Halpern, "Current and emerging technologies in melanoma diagnosis: the state of the art," *Clinics in Dermatology*, vol. 27, no. 1, pp. 35–45, 2009. [Online]. Available: http://dx.doi.org/10.1016/j.clindermatol.2008.09.004

[39] D. Gutkowicz-Krusin, M. Elbaum *et al.*, "Precision of automatic measurements of pigmented skin lesion parameters with a MelaFindTMmultispectral digital dermoscope," *Melanoma Research*, vol. 10, no. 6, pp. 563–570, 2000.

[40] N. Qaddoumi, M. A. Khousa, and W. Saleh, "Near-field microwave imaging utilizing tapered rectangular waveguides," *Conference Record - IEEE Instrumentation and Measurement Technology Conference*, vol. 1, no. 5, pp. 174–177, 2004.

[41] D. Dancila, R. Augustine *et al.*, "Millimeter wave silicon micromachined waveguide probe as an aid for skin diagnosis - results of measurements on phantom material with varied water content," *Skin Research and Technology*, vol. 20, no. 1, pp. 116–123, 2014.

[42] D. Caratelli, A. Lay-Ekuakille, and P. Vergallo, "Non-invasive reflectometry-based detection of melanoma by piezoelectric micro-needle antenna sensors," *Progress In Electromagnetics Research*, vol. 137, no. January, pp. 687–702, 2013.

[43] F. Topfer, S. Dudorov, and J. Oberhammer, "Millimeter-wave near-field probe designed for high-resolution skin cancer diagnosis," *IEEE Transactions on Microwave Theory and Techniques*, vol. 63, no. 6, pp. 2050–2059, 2015.

[44] G. Salerni, C. Alonso, and R. Fernández-Bussy, "A series of small-diameter melanomas on the legs: dermoscopic clues for early recognition," *Dermatology Practical & Conceptual*, vol. 5, no. 4, pp. 31–36, 2015.

[45] F. Kazemi, F. Mohanna, and J. Ahmadi-shokouh, "Detection of biological abnormalities using a near-field microwave microscope," *International Journal of Microwave and Wireless Technology*, no. May, 2018.

[46] P. Oltulu, B. Ince *et al.*, "Measurement of epidermis, dermis, and total skin thicknesses from six different body regions with a new ethical histometric technique," *Turk Plastik, Rekonstruktif ve Estetik Cerrahi Dergisi*, vol. 26, no. 2, pp. 56–61, 2018.

[47] S. Gabriel, R. W. Lau, and C. Gabriel, "The dielectric properties of biological tissues: III. Parametric models for the dielectric spectrum of tissues," *Physics in medicine and biology*, vol. 2271, 1996.

[48] H. Hwang, J. Yim *et al.*, "110 GHz broadband measurement of permittivity on human epidermis using 1 mm coaxial probe," *IEEE MTT-S International Microwave Symposium Digest, 2003*, vol. 1, pp. 399–402, 2003. [Online]. Available: http://ieeexplore.ieee.org/document/1210961/

[49] N. Chahat, M. Zhadobov *et al.*, "Human skin permittivity models for millimetre-wave range," *Electronics Letters*, vol. 47, no. 7, p. 427, 2011.

[50] O. Gandhi and a. Riazi, "Absorption of Millimeter Waves by Human Beings and its Biological Implications," *IEEE Transactions on Microwave Theory and Techniques*, vol. 34, no. 2, pp. 228–235, 1986.

[51] R. Aminzadeh, M. Saviz, and A. A. Shishegar, "Dielectric properties estimation of normal and malignant skin tissues at millimeter-wave frequencies using effective medium theory," *22nd Iranian Conference on Electrical Engineering, ICEE 2014*, no. Icee, pp. 1657–1661, 2014.

[52] S. I. Alekseev and M. C. Ziskin, "Human skin permittivity determined by millimeter wave reflection measurements," *Bioelectromagnetics*, vol. 28, no. 5, pp. 331–339, 2007.

[53] P. Hasgall, F. Di Gennaro *et al.*, "IT'IS Database for thermal and electromagnetic parameters of biological tissues, Version 4.0," 2015. [Online]. Available: https://itis.swiss/virtual-population/tissue-properties/

[54] C. Gabriel, "Compilation of the Dielectric Properties of Body Tissues At Rf and Microwave Frequencies," Tech. Rep., 1996.

[55] G. Mansutti, A. T. Mobashsher, and A. M. Abbosh, "Millimeter-wave Substrate Integrated Waveguide Probe for Near-Field Skin Cancer Detection," in *2018 Australian Microwave Symposium*, no. February, 2018, pp. 1–7.

[56] G. G. Borg, J. H. Harris *et al.*, "Plasmas as antennas: Theory, experiment and applications," *Physics of Plasmas*, vol. 7, no. 5, pp. 2198–2202, 2000. [Online]. Available: http://aip.scitation.org/doi/10.1063/1.874041

[57] T. Anderson, *Plasma Antennas*. Artech House, 2011.

[58] A. I. Morozov, *Introduction to Plasma Dynamics*. CRC Press, 2012.

[59] J. P. Rayner, A. P. Whichello, and A. D. Cheetham, "Physical characteristics of plasma antennas," *IEEE Transactions on Plasma Science*, vol. 32, no. 1, pp. 269–281, 2004. [Online]. Available: http://ieeexplore.ieee.org/lpdocs/epic03/wrapper.htm?arnumber=1291644

[60] T. J. Dwyer, J. R. Greig *et al.*, "On the Feasibility of Using an Atmospheric Discharge Plasma as an RF Antenna," *IEEE Transactions on Antennas and Propagation*, vol. 32, no. 2, pp. 141–146, 1984.

[61] M. A. Lieberman and A. J. Lichtenberg, *Principles of Plasma Discharges and Materials Processing: Second Edition*, 2005.

[62] M. Moisan, A. Shivarova, and A. W. Trivelpiece, "Experimental Investigations of the Propagation of Surface Waves Along a Plasma Column," *Plasma Physics*, vol. 24, no. 11, pp. 1331–1400, 1982.

[63] T. Naito, S. Yamaura *et al.*, "Theoretical and experimental investigation of plasma antenna characteristics on the basis of gaseous collisionality and electron density," *Japanese Journal of Applied Physics*, vol. 54, no. 1, p. 016001, 2015.

[64] A. Locatelli, S. Boscolo *et al.*, "Nanoscale control of the radiation properties of coupled nanoantennas," *IEEE Photonics Technology Letters*, vol. 23, no. 20, pp. 1541–1543, 2011.

[65] L. Novotny, "Effective wavelength scaling for optical antennas," *Physical Review Letters*, vol. 98, no. 26, pp. 1–4, 2007.

[66] D. Melazzi, V. Lancellotti *et al.*, "Numerical Investigation Into the Performance of Reconfigurable Gaseous Plasma Antennas," in *The 8th European Conference on Antennas and Propagation (EuCAP 2014)*, 2014, pp. 2338–2342.

[67] O. Tudisco, A. Lucca Fabris *et al.*, "A microwave interferometer for small and tenuous plasma density measurements," *Review of Scientific Instruments*, vol. 84, no. 3, 2013.

[68] D. Melazzi, P. De Carlo *et al.*, "Numerical results on the performance of gaseous plasma antennas," *Proceedings of the 2015 International Conference on Electromagnetics in Advanced Applications, ICEAA 2015*, pp. 569–572, 2015.

[69] E. D. Kaplan and C. J. Hegarty, *Understanding GPS. Principles and applications*, second edi ed. Artech House, 2006. [Online]. Available: http://linkinghub.elsevier.com/retrieve/pii/S1364682697833378